Dynamics and Structure of Negative Ions

- Photoinduced double detachment on nano- and femtosecond time scales

INAUGURAL-DISSERTATION

ZUR ERLANGUNG DES DOKTORGRADES DER FAKULTÄT
FÜR MATHEMATIK UND PHYSIK

ALBERT-LUDWIGS-UNIVERSITÄT
FREIBURG IM BREISGAU, DEUTSCHLAND
&
GÖTEBORGS UNIVERSITET
GÖTEBORG, SVERIGE

VORGELEGT VON

HANNES HULTGREN

SEPTEMBER 24, 2012

UNIVERSITY OF
GOTHENBURG

Institute of Physics
Albert Ludwig's University
Freiburg 2012

Department of Physics
University of Gothenburg
Gothenburg 2012

Dekan: Prof. Dr. Kay Königsmann.
Leitern der Arbeit:
Dr. Igor. Yu. Kiyan,
Prof. Dr. Dag Hanstorp,
Prof. Dr. Hanspeter Helm.

Dynamics and Structure of Negative Ions
- Photoinduced double detachment on nano- and femtosecond time scales

Institute of Physics
Albert Ludwig's University
D-79104 Freiburg im Breisgau, Germany
Telephone +49(0)761 203 5723

Department of Physics
University of Gothenburg
SE-412 96 Gothenburg, Sweden
Telephone +46 (0)31 786 1000

Typeset in LaTeX
Figures created using MATLAB, Power Point, GIMP, FRED.

ABSTRACT

The goal of the presented work is to investigate double detachment of negative ions on nano- and femtosecond time scales. I have performed three types of experiments.

Femtosecond time resolved pump-probe experiments have been performed on electron dynamics in the valence shell of carbon, silicon and germanium atoms. The atom under investigation was prepared by strong field photodetachment of its parent negative ion in a linearly polarized femtosecond laser pulse. The detachment process coherently populates the fine structure levels of the atomic ground state giving rise to an electronic wave packet moving in the valence shell of the atom. The wave packet is probed by strong field ionization at a time delay controlled on a femtosecond time scale. The ionized electrons are detected in an electron imaging spectrometer. The energy and angular distribution of the ionized electrons provide information on the phase of the wave packet. The results reveal a periodic spatial rearrangement of the electron cloud in the atom. The experimental procedure and detection scheme developed provide the first direct visualization of an electronic wave packet moving in the ground state of an atom.

The process of rescattering in strong field detachment has also been investigated. The detached electron is accelerated in the laser field. When the E-field changes its direction the electron follows and may return and collide with the core. I have investigated the rescattering effect in negative fluorine ions and compared with previous results on bromine ions. Furthermore, strong field detachment experiments of F_2^- were conducted and the results from molecular fluorine ions are compared to results from atomic fluorine ions.

Photodetachment cross sections and doubly excited states in K^- and Cs^- have been investigated through double detachment. A resonant ionization scheme was used where the ion beam and laser beams were in a collinear configuration allowing for measurements of partial cross section channels individually with nearly 100% detection efficiency. A new threshold behavior has been found in photodetachment into atomic states having a large and negative polarizability. A new model was developed to explain the observed phenomena. Furthermore, two new resonances stemming from doubly excited states were found below the K(7 ^{2}P) channel opening in K^- and a set of new resonances was observed in Cs^- below the Cs(10 ^{2}P) channel.

Research publications

Part of the work presented in this thesis is based on the following research articles.

- *Electron Rescattering in Above-Threshold Photodetachment of Negative Ions*
  A. Gazibegović-Busuladžić, D. B. Milošević, W. Becker, B. Bergues, H. Hultgren, and I. Yu. Kiyan
  Physical Review Letters **104**, 103004 (2010).

- *Photodetachment dynamics of F_2^- in a strong laser field*
  H. Hultgren and I. Yu. Kiyan
  Physical Review A **84**, 015401 (2011).

- *Visualization of electronic motion in an atomic ground state*
  H. Hultgren, M. Eklund, D. Hanstorp and Igor Yu. Kiyan
  in preparation.

- *Visualization of electronic motion in the ground state of carbon and silicon atoms*
  H. Hultgren, M. Eklund, A. O. Lindahl, D. Hanstorp and Igor Yu. Kiyan
  in preparation.

- *Threshold Photodetachment in a Repulsive Potential*
  A. O. Lindahl, J. Rohlén, H. Hultgren, I. Yu. Kiyan, D. J. Pegg, C. W. Walter, and D. Hanstorp
  Physical Review Letters **108**, 033004 (2012).

- *Experimental studies of partial photodetachment cross sections in K^- below the K(7 ^2P) threshold*
  A. O. Lindahl, J. Rohlén, H. Hultgren, I. Yu. Kiyan, D. J. Pegg, C. W. Walter, and D. Hanstorp
  Physical Review A **85**, 033415 (2012).

- *Observation of overlapping resonances below the 10 $^2P_{1/2,3/2}$ states in photodetachment of Cs^-*

A. O. Lindahl, J. Rohlén, H. Hultgren, D. J. Pegg, C. W. Walter, and D. Hanstorp
in preparation.

TABLE OF CONTENTS

Preface

You are welcome to my thesis. Chapter 1 and 2 are an introduction to my field of physics, introducing the concepts and ideas needed to understand and appreciate the results of the research presented in this thesis. Chapter 3 treats, in detail, the experimental methods and equipment that I have used and developed during my PhD years. Some detours are done, dwelling on aspects that have been important for the outcome of the experiments. Chapter 4 to 10 provide the results of each project that I have participated in. These results are published or close to be submitted. Chapter 11 is a shorter discussion of the main scientific results that have been obtained. I have enjoyed immensely doing the research leading to this thesis. It has been hard work, surprises, mixed with dead ends and finally success. Nothing beats the feeling of suddenly understanding something that a minute ago was a black box full of: "I don't have a clue". Science is fun and shall always be approached with an open mind, ready to appreciate whatever you may learn.

The work culminating in this thesis has been conducted under an agreement on graduation by means of a joint supervision (cotutelle) between the University of Freiburg and University of Gothenburg. The major part of this work has been performed in the research group of Prof. Dr. Helm in Freiburg, where the projects have been led by Dr. Kiyan. I have also taken part in a research project in the group of Prof. Hanstorp in Gothenburg. My contribution to the projects that this thesis are based on are the following: For chapter 4, together with Dr. Kiyan I did the experiment on the fluorine ion, analyzed the data and took part in writing the manuscript. For chapter 5 I did all the measurements, analyzed the data and performed the simulations presented and compared with experimental results and wrote the manuscript together with Dr. Kiyan. The simulation routine was first constructed by previous PhD student Boris Bergues. The code was developed further by me. It was rewritten in c++, optimized and therefore the computation time needed was decreased by a factor of

10-15, depending on the experimental parameters used. Chapter 6 and 7 are the results of my main project. Together with principal investigator Dr. Kiyan, I developed the pump-probe setup having femtosecond time resolution. I performed simulations in physical optics software (FRED) to find the configuration yielding the highest laser peak intensity in the interaction region. The development of a diagnostic system to ensure a perfect overlap of the ion beam and laser beams were required. Furthermore, a new ion source were installed together with a custom built water cooled high voltage system. In addition I built a new type of cesium oven for the sputter source, allowing to insert new cesium without risk of oxidizing it. To perform the experiments presented in chapter 6 and 7 a new data acquisition and data treatment procedure were developed. I performed the simulations and compared with experimental results and I wrote the first versions of the manuscripts.

Chapter 8, 9 and 10 presents the results of the projects performed in the research group in Gothenburg. I joined the project in a stage when the main part of the system had been built by A. O. Lindahl and previous PhD students. I took part in constructing the optical setup and getting all the parts of the system running smoothly together. I did my night shifts during the data acquisition and I took part in the data analysis and in writing the manuscripts.

Hannes Hultgren
Gothenburg. September 24, 2012.

CHAPTER 1

Introduction

"Anyone who says that they can contemplate quantum mechanics without becoming dizzy has not understood the concept in the least."

—Niels Bohr

1.1 Quantum Mechanics, Atoms and Ions

Classical mechanics provides a deterministic view of the world. A particle can be well defined in its size and mass. The path and future positions can be calculated if its position and velocity at a given time is known. The precision of the measuring device is the sole limiting factor for the accuracy of our knowledge of a particle's state, and the world in general. This is not true in the world of Quantum Mechanics (QM). QM has a probabilistic nature where the state of a particle only can be predicted with a certain probability. The history of QM starts in the year 1900 when Planck introduced quantization of energy to derive the spectral distribution of a radiating black body [1]. In 1905 Einstein explained the photo-electric effect by describing light as quantized particles, now called photons [2]. Hence, light has a particle nature together with its well known wave behavior described by the Maxwell equations [3, 4]. De Broglie suggested in 1924 that the wave-particle duality applies not only to light but also to matter [5]. The de Broglie wavelength of a particle is given by $\lambda = \hbar/p$ where p is the momentum of the particle and $\hbar$ is Planck's constant divided by 2π. The wave nature of particles is normally only visible on a microscopic level. The phenomena has been observed in a number of experiments

such as electron [6–8] and neutron diffraction [9]. Schrödinger formalized the probabilistic view of quantum mechanics introducing the wave equation $i\hbar\frac{\partial}{\partial t}\Psi(\vec{r},t) = \hat{H}\Psi(\vec{r},t)$ to describe a quantum mechanical system evolving in time [10]. $\Psi(\vec{r},t)$ is the wave function of the system, describing the probability amplitude for the system as a function of position and time. $\hat{H}$ is the Hamilton operator representing the total energy of the system when operated on the wave function $\Psi(\vec{r},t)$. Schrödinger's formulation of quantum mechanics is telling us that the position and energy of a system is not arbitrarily well defined. The probability distribution is given by $\Psi\Psi^*$. The mathematical description of a particle moving in space is a wave packet. A wave packet can be described as a sum of complex-valued plane waves $e^{i(\mathbf{k}\cdot\mathbf{r}-\omega t)}$ having different waves vectors $\mathbf{k}$ and therefore different momenta. The waves interfere constructively in a limited region of space and destructively elsewhere. The wave packet has a distribution in position and momentum space therefore the particle's position and momentum is known only to a certain degree. The uncertainty was described by Heisenberg [11] in the uncertainty principle, $\Delta p \cdot \Delta x \geq \hbar$, where Δp is the uncertainty in momentum and Δx is the uncertainty in position. The uncertainty principle implies that some observables, e.g. momentum and position, cannot be measured arbitrarily accurately at the same time. Similarly, time and energy can not be exactly specified for a system. The uncertainty relation for energy and time reads $\Delta E \cdot \Delta t \geq h$, where ΔE is the uncertainty in energy and Δt is the uncertainty in time.

Matter consists of atoms and an atom is a nucleus, being positively charged, surrounded by an cloud of negatively charged electrons. The electron cloud of an atom is configured in discrete states, where the energy and angular momenta of the states are quantized. The atomic state is described by a wave function and the square of the wave function is referred to as an orbital. Orbitals specify the probability of finding an electron at a certain position in space, depending on its energy and angular momenta. For an atom in an eigenstate, the probability density distribution is constant over time. As an example, the ground state of the hydrogen atom has a static spherical probability distribution, where the electron's most probable radial distance from the nucleus is one Bohr radius (0.529 Å). In an ion the number of protons and electrons is not equal giving the atom an overall positive or negative charge.

An electron in an atom can absorb a photon and gain enough energy to break free from the binding potential created by the nucleus and

the other electrons. The unbound electron can have any given energy and is said to be in the continuum, in contrast to the case when it is bound inside the atom where only certain energies are allowed. The process of promoting a bound electron in to the continuum is referred to as photodetachment when the initial system is a negative ion, and ionization when the initial system is an atom or positive ion. In photodetachment the energy needed to remove one electron is denoted as the electron affinity (EA), while the energy needed to ionize an atom or positive ion is referred to as the ionization potential (IP). An atom can be in an excited state which means that the electrons are in a configuration where the total energy is larger than in the ground state. An excited state has a finite lifetime, and will always relax back into the ground state. The excess energy is released through different processes depending on the quantum system involved. In atoms the excess energy is released by emitting a photon of frequency ν. The photon energy, $E_{ph} = h\nu$, matches the energy difference between the two states in the atom, $h\nu = E_{excited} - E_{ground}$. The reverse of the photon relaxation process can also occur, i.e. photon absorption. If a photon's energy matches the energy difference between two states in an atom, it can be absorbed and promote the atom to an energetically higher state. By observing the frequency of emitted or absorbed photons from an element, knowledge on the structure of atoms can be extracted. This is the idea of all spectroscopy.

The field of spectroscopy was opened in 1814 when Fraunhofer invented the spectroscope. Fraunhofer investigated the light spectrum emitted from the sun and he found several dark lines in the spectrum. The dark lines were later explained by Bunsen and Kirchhoff as being absorption lines corresponding to the energy levels of the elements in the sun's atmosphere. In their research Bunsen and Kirchhoff burned elements in a hot gas flame and observed the emitted light spectrum. They realized that atoms in the flame were continuously being excited by the heat and subsequently relaxed by emitting a photon. The energy levels in an atom are unique for each element. Hence, the emitted photons forms a specific spectrum, a fingerprint allowing an identification of an element in a sample. Bunsen performed a systematic study of the observed spectral lines and discovered two new elements, cesium and rubidium. Both the process of absorbing and emitting photons are used in spectroscopy to map out the structure of atoms, ions and molecules. The invention of the LASER in 1960 [12, 13] and especially tunable lasers in 1966 [14, 15], where the wavelength can be altered over a wide range, has had a huge impact on the field of spec-

troscopy. The subsequent invention of mode locked lasers has provided extremely short laser pulses. The idea of mode locking was proposed already in 1964 [16] and realized in 1972 [17]. Since then pulse lengths of femtosecond [18, 19] and attosecond [20, 21] lengths have been achieved. The results presented in this thesis would have been inaccessible without the development of tunable and pulsed lasers.

My work has focused on the photodetachment process of negative ions and the ionization process of atoms with the use of intense laser light. I have performed mainly two types of experiments. At Göteborg University Negative Ion Laser LAboratory (GUNILLA) a laser pulses of a few nanoseconds duration were used. The relatively long pulse duration enables a very precise frequency of the laser light. This is in accordance with Fourier transform [22], where a broad spectrum in the time domain gives a narrow spectrum in the frequency domain. The well defined energy of the photons (0.2cm^{-1}) allowed us to map out the structure of negative ions and atoms with high accuracy. In the laser lab at Albert Ludwig's University in Freiburg, on the other hand, a femtosecond laser were used to measure ultra fast dynamics in the outer electron shell of atoms. The short pulse duration also gives rise to a very high flux of photons, generating new previously unobserved phenomena in the interaction between light and matter. The two laser systems complemented each other in an excellent way. High precision structural measurements were done at GUNILLA while electron dynamics in the time domain were studied with ultra high temporal resolution at the laser lab at Albert Ludwig's University.

CHAPTER 2

Theory

"Theory helps us bear our ignorance of facts."

– George Santayana

2.1 Negative ions and photodetachment

The electrons in an atom are bound by the Coulomb potential, stemming from the attraction between the positively charged nucleus and the negatively charged electron. The potential decreases with distance as $1/r$ at large distances. In negative ions the outermost electron experiences an attractive force from the nucleus and a repulsive force from the other electrons. In order to explain the existence of negative ions electron correlation has to be considered. The independent-particle model, where each particle is considered to move in the mean field of the other particles of the system, functions well for atoms. If the model is applied to a negative ion the net attractive force is not sufficiently strong to form a stable ion. However, if one considers correlated motion of the electrons the electron cloud and nucleus can be slightly deformed, generating a dipole. In a dipole one side is slightly positively charged while the other is slightly negatively charged. The dipole gives rise to a binding potential that decreases as $1/r^4$. The full potential seen at large distances by the outermost electron in a negative ion, including the effective centrifugal potential is given by Eq. 2.1. Atomic units ($m = \hbar = 1$) are used.

$$U(r) = \frac{\ell(\ell+1)}{2r^2} - \frac{\alpha}{2r^4}, \tag{2.1}$$

where ℓ is the angular momentum of the electron and α is the static dipole polarizability of the atom. An atom can be excited, through collision with other particles or by absorbing a photon. When excited, one electron in the atom is promoted to a state energetically closer to the continuum. Due to the $1/r$ dependency of the Coulomb potential, an infinite number of exited states are incorporated in an atom. In negative ions, however, where the potential decays as $1/r^4$, usually only a single excited state is present below the lowest continuum threshold.

At GUNILLA in Gothenburg investigations have been performed on the shape of the photodetachment threshold in negative ions when the photon energy is just sufficient to detach the electron. The kinetic energy of the detached electron is, hence, small and therefore the electron spends an extended amount of time in the vicinity of the parent core and electron-electron interactions become important. Wigner showed in 1948 [23] that the cross section close to the threshold, i.e. the probability, for photodetachment is given by

$$\sigma_{pd} \propto E_e^{\ell+1/2} = (\hbar\omega - E_{th})^{\ell+1/2}, \tag{2.2}$$

where E_e and ℓ are the energy and angular momentum of the detached electron, respectively. $\hbar\omega$ is the supplied photon energy and E_{th} is the threshold energy for the detachment process to occur. In figure 2.1 the general behavior of the cross section over a large energy range is depicted. At E_{th} the supplied energy is sufficient to detach the electron but the available phase space is small and therefore the probability is low. As the energy is increased, the phase space gets larger and the cross section increases. At high photon energies the quickly oscillating wave function of the emitted electron diminishes the overlap between the initial and final states and hence the cross section decreases.

The first photodetachment experiments were performed in 1953 by Fite and Branscomb [24]. Two years later the cross section for photodetachment of H^- and D^- [25] as well as O^- [26] were measured. The electron affinities for many of the elements in the periodic table were studied and determined by Hotop and Lineberger between 1970 and 1975 [27–31,129], the latest review was published in 1999 [140]. In most atomic states the centrifugal part of the potential in Eq. 2.1 is dominating, giving rise to the threshold behavior described by Wigner. However, if the polarizability of the atom is large the shape of the threshold can no longer be described by the Wigner law.

An excited atom can bind an extra electron and form a negative ion where two electrons are in an excited state. In these ions, two elec-

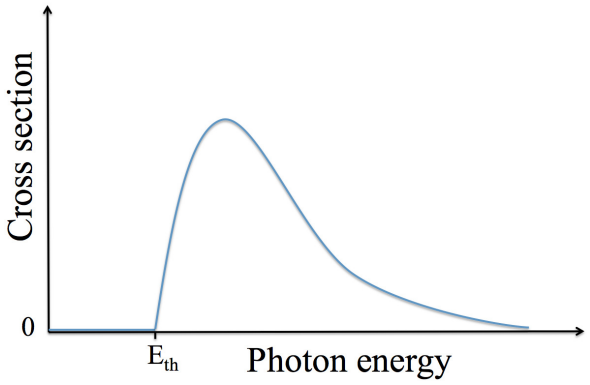

Figure 2.1: *Sketch showing the general behavior of the cross section for photodetachment over a wide energy range.*

trons are in an excited state comparably far from the parent core and therefore electron-electron correlations become pronounced. The doubly excited states lie in the continuum, above the single detachment limit (Fig: 2.2). Since the states are in the continuum they autodetach. On a picosecond time scale they decay in to one free electron and a neutral atom. The doubly excited states affect the probability for photodetachment and are refereed to as resonances in the cross section spectrum. If the doubly excited state is located energetically below the parent state in the atom, it is called a Feshbach resonance while if the doubly excited state is located above the parent state it is a shape resonance. A shape resonance decaying into its parent state increases the photodetachment cross section since the probability of absorbing a photon is enhanced if an energetically suitable state is available. The simplest negative ion H^- has previously been investigated both theoretically and experimentally [32,145,147,148]. In H^- the doubly excited states are highly excited, out of reach for conventional laser systems. Therefore quasi two-electron systems have attracted a lot of attention [149–152]. In negative ions formed by the alkali metals the doubly excited states lie in the UV wavelength region and can thus be reached by tabletop laser systems.

The process where a negative ion is promoted to a doubly excited state followed by autodetachment is depicted by the solid vertical arrow followed by the dashed-dotted diagonal arrows in Fig. 2.2. However, if one is observing the decay in to an atomic state below the parent state there are two competing processes leading to the same final state. The resonant excitation followed by autodetachment described above and the direct detachment where one electron absorbs the photon energy and is detached directly. These two paths give rise to quantum inter-

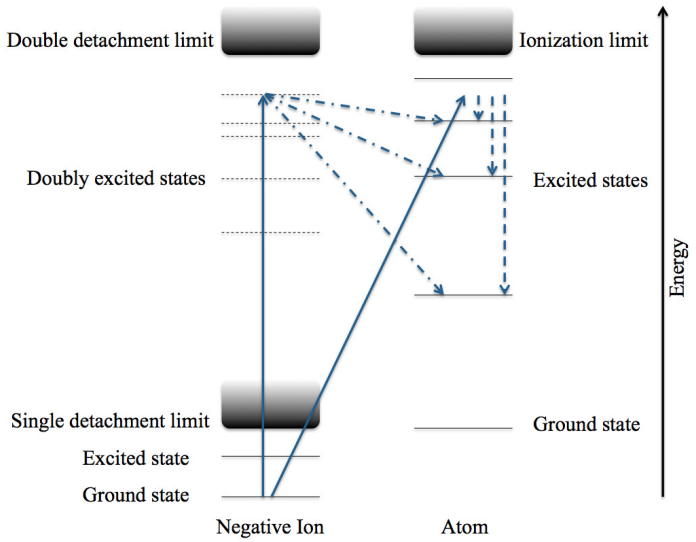

Figure 2.2: *Schematic view of the energy levels in a negative ion and an atom. Vertical solid arrow represents a double excitation. Diagonal dashed-dotted lines represents autodetachment, where one electron is ionized and the other falls in to the ground state or an excited state in atom. Diagonal solid line and vertical dashed lines represent the direct photodetachment process.*

ference, modulating the cross section spectra. A review on resonances in photodetachment cross sections is available in [33]. Doubly excited states can also be investigated by electron scattering on neutral atoms. An incoming electron can be captured forming a doubly excited state and subsequently emitted, giving rise to resonances in the observed cross section spectrum [34]. Electron beams have also been used to study collisional detachment of negative ions [35, 36]. An electron can attach to a molecule and form a stable negative molecular ion. Molecular ions is a vast field of research. In experiments on molecular ions, resonances has been observed stemming from excited doubly negatively charged states [37, 38]. No doubly negatively charged atomic ions have been observed. Molecular negative ions have been observed in interstellar clouds [39] and have since then attracted a wide interest [40–43].

Experiments investigating the cross sections, doubly excited states and threshold behaviors of K^- and Cs^- are described in Chapter 8, 9 and 10.

2.2 Strong field effects

The idea of a multiphoton transitions in an atom was first considered theoretically by Goeppert-Mayer in 1931 [44]. The cross section for such a process is very small and no light source, intense enough, was available at the time. Twenty years later the invention of intense radio frequency emitters allowed observations of multiphoton transitions between Zeeman sub levels in atoms [45–47] and molecules [48]. The invention of the laser has had a revolutionary impact on the posibilities to conduct multiphoton experiments. The first two photon excitations by a laser field were done on CaF_2 molecule in 1961 [49], followed by the first two photon excitation of an atom [50]. Two photon detachment of a negative ion were done by Hall et al. in 1965 [51] and multiphoton ionization was observed in 1965 by Voronov et al. [52] and in 1968 by Agosini et al. [53]. The first strong field experiments were performed by Agostini et al. in 1979 [54]. In strong field ionization the electron can absorb a substantially larger number of photons than needed to be promoted to the continuum. This process is referred to as Above Threshold Ionization (ATI) [54–56]. This is not to be confused with multiphoton ionization, where the electron only absorbs the number of photons needed to break free from the atomic potential. In the strong field experiment by Agostini et al. the kinetic energy distribution of electrons ionized from Xenon in the focus of an intense laser beam was measured. The energy spectrum revealed peaks in the electron energy distribution separated by the photon energy. These peaks are refereed to as ATI peaks. The corresponding phenomena in negative ions is called excess photon detachment and was first observed in [57–59]. Experiments where the laser intensities exceed 10^{12} W/cm^2 are commonly regarded as strong field experiments. Strong field detachment and ionization occur in two ways depending on the strength of the applied laser field relative to the atomic electric field experienced by the electron. In the multi photon regime, the external laser field is weak compared to the atomic field an can be treated as a perturbation. However, the flux of photons is sufficiently large for the electron to absorb more energy than needed to reach the continuum as shown in Fig. 2.3a. On the other hand, in the tunneling regime, the external laser field is comparable to the atomic electric field and the atomic potential is deformed, allowing the electron to tunnel out in to the continuum (Fig. 2.3b). An experiment is conducted in one of the regimes or in between the two, where the processes are competing.

The process of strong field detachment was described theoretically by

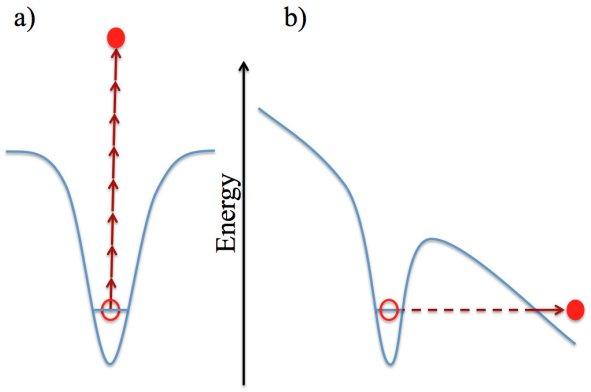

Figure 2.3: *Strong field photodetachment in the multi photon regime (left) and tunneling regime (right).*

Keldysh [65], who introduced the Strong Field Approximation (SFA). In SFA the interaction between the detached electron and the residual core is neglected. The final state is a detached electron quivering in the external laser field. The state is described by a Volkov wave function, [66]. The SFA has been further developed by Faisal and Reiss [67, 68] and is therefore referred to as Keldysh-Faisal-Reiss (KFR) theory. The SFA makes the expression for the detachment rate analytical and hence comparably straight forward to simulate. The Keldysh parameter is a quantitative comparison of the internal atomic field and the external laser field. The parameter is given by

$$\gamma = \sqrt{\frac{IP}{2U_p}}, \tag{2.3}$$

where IP is the ionization potential in electron volts, eV. UP is the ponderomotive energy, that is the cycle averaged quiver energy of an electron in an alternating electric field. The ponderomotive energy is given by

$$U_p = \frac{e^2 I}{2c\epsilon_0 m\omega^2}, \tag{2.4}$$

where e is the electron charge, I is the laser intensity, c is the speed of light, ϵ_0 is the permittivity of vacuum, m is the electron mass and ω is angular frequency of the laser light. $\gamma > 1$ represent the multi-photon regime while if $\gamma < 1$ represents the tunneling regime. In the strong field experiments presented in this thesis γ is in the range 0.1 to 0.5. The electric field amplitude in the laser field is maximum twice per optical cycle, hence electrons will be emitted with equal probability at two separate instances in time, see Fig. 2.4. The wave nature of

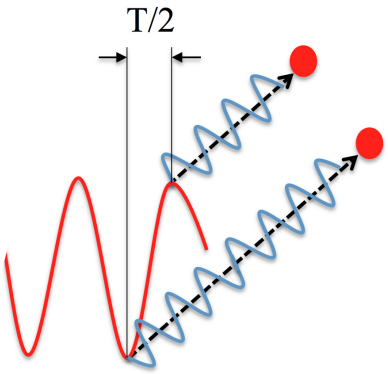

Figure 2.4: *The electric field amplitude is maximal at two instances in time, separated by T/2, giving rise to quantum interference between emitted electrons.*

electrons give rise to quantum interference in the far field when the electrons are detected [69, 70, 91]. This quantum interference was observed in strong field experiments on H^- [75], F^- [64] and Br^- in [71].

When an electron is detached from its parent core it is accelerated in the external laser field. When the E-field changes its direction the electron follows and may return and collide with the core. If the electron recombines with core the excess energy, gained in the electric field, is released as a high energy photon, in the process referred to as High Harmonic Generation (HHG) [60–63]. HHG is used to produce ultra short pulses in the x-ray regime. A short, high intensity, pulse is focused in to a gas cell containing a noble gas. The noble gas is strong field ionized and a small fraction of the electrons recombine with their parent core to produce a short coherent x-ray pulse. Recent development of HHG indicates that it could replace synchrotrons for photon energies up to 1 keV.

When simulating quantum mechanical systems solving the Schrödinger equation quickly becomes impossible with increasing number of particles. In simulations of strong field detachment an additional approximation is required together with the SFA mentioned earlier. In the Single Active Electron (SAE) approximation the multi electron ion is described by a single electron bound by an effective potential from the core. The ground state of the electron, with no laser field present, is given by $|\Phi_0\rangle$. The Schrödinger equation allows to determine the wavefunction $|\Psi(t)\rangle$, describing the time evolution of the system. Atomic units (e = m = $\hbar$ = 1) are used throughout.

$$i\hbar\frac{\partial}{\partial t}|\Psi(t)\rangle = H(t)|\Psi(t)\rangle, \tag{2.5}$$

with the initial condition $|\Psi(t_0)\rangle = |\Phi_0\rangle$. The Hamiltonian, $H(t)$, is

$$H(t) = -\nabla/2 + V(\mathbf{r}) + \mathbf{r}\cdot\mathbf{E}(t), \tag{2.6}$$

where the kinetic energy of the electron is $\nabla/2$, the potential energy in the short range potential is described by $V(\mathbf{r})$ and $\mathbf{r}\cdot\mathbf{E}(t)$ represents the electron's interaction with the laser field $\mathbf{E}(t)$. The probability amplitude of detaching an electron with drift momentum $\mathbf{p}$ is given by the transition matrix element

$$M_{\mathbf{p}i} = -\mathrm{i}\lim_{\mathrm{t}\to\infty}\int_{-\infty}^{\mathrm{t}} \mathrm{dt}'\langle\psi_{\mathbf{p}}(\mathrm{t})|\mathrm{U}(\mathrm{t},\mathrm{t}')\mathbf{r}\cdot\mathbf{E}(\mathrm{t}')|\psi_{\mathrm{i}}(\mathrm{t}')\rangle, \tag{2.7}$$

where $|\psi_i(t')\rangle$ and $|\psi_{\mathbf{p}}(t)\rangle$ describe initial state and the final state having drift momentum $\mathbf{p}$, respectively. $U(t',t)$ is the time evolution operator of the Hamiltonian, $H(t)$. $U(t',t)$ maps the ground state of the electron on to some state in the system at a later time t, $|\psi_i(t)\rangle = U(t,t_0)|\Phi_0\rangle$. The time evolution operator $U(t',t)$ satisfies the Dyson equation

$$U(t,t') = U_L(t,t') - \mathrm{i}\int_{\mathrm{t}'}^{\mathrm{t}} \mathrm{dt}''\mathrm{U_L}(\mathrm{t},\mathrm{t}'')\mathrm{V}(\mathbf{r})\mathrm{U}(\mathrm{t}'',\mathrm{t}') \tag{2.8}$$

where U_L is the time evolution of the Hamiltonian, $H_L(t) = -\nabla/2 + \mathbf{r}\cdot\mathbf{E}(t)$, describing a free electron in the laser field excluding the interaction with the potential. The electron's initial state $|\psi_i(t)\rangle$ is represented by

$$\psi_{lm}(\mathbf{r}) = (A/r)\exp(-\kappa r)Y_{lm}(\hat{\mathbf{r}}), \tag{2.9}$$

where A is a normalization constant, κ is given by the binding energy, E_a, as $\kappa = \sqrt{2E_a}$. ℓ and m are the angular momentum quantum numbers of the initial state. We make two approximations to equation 2.7. U is replaced by U_L and the final state $\langle\psi_{\mathbf{p}}(t)|$, being a free electron is represented by a plane wave. The state $\langle\psi_{\mathbf{p}}(t)|U_L(t,t')$ then becomes the Volkov state, $\langle\psi^{(L)}_{\mathbf{p}}(t')|$, representing a free electron in a laser field. Equation 2.7 is then rewritten as

$$\begin{aligned} M^{SFA}_{\mathbf{p}i} &= -\mathrm{i}\int_{-\infty}^{\infty}\mathrm{dt}\langle\psi^{(\mathrm{L})}_{\mathbf{p}}(\mathrm{t})|\mathbf{r}\cdot\mathbf{E}(\mathrm{t})|\psi_{\mathrm{i}}(\mathrm{t})\rangle \\ -\int_{-\infty}^{\infty}dt\int_{t}^{\infty}dt'\langle\psi^{(L)}_{\mathbf{p}}(t')|V(\mathbf{r})U_L(t',t)\mathbf{r}\cdot\mathbf{E}(t)|\psi_i(t)\rangle, \end{aligned} \tag{2.10}$$

The first term on the right hand side represent the probability amplitude of direct detachment of electrons, which is the standard SFA. However, also the second term on the right hand side may be included

in simulations. This term represents electrons that travel back with the oscillating electric field in the laser light and rescatter off the parent core. The core potential $V(\mathbf{r})$ on the right hand side is specific for each negative ion and is modeled by the double Yukawa potential [73]

$$V(\mathbf{r}) = -\frac{Z}{H}\frac{e^{-r/D}}{r}(1 + (H-1)e^{-Hr/D}), \tag{2.11}$$

where $H = DZ^{0.4}$, Z is the atomic number and D is a numerical parameter. The full expression for the differential detachment rate, summing over all possible n-photon processes, is then given by

$$d\omega = 2\pi \sum_{n \geq n_0} |M_{\mathbf{p}i}|^2 \delta(\frac{p^2}{2} + U_p + E_0 - n\omega)\frac{d^3p}{(2\pi)^3}, \tag{2.12}$$

where $M_{\mathbf{p}i}$ is the n-photon transition amplitude given by Eq. 2.10, with or without taking the second rescattering term into account. n_0 is the minimum number of photons needed to overcome the detachment threshold. The δ-function accounts for the conservation of energy and p is the electrons momentum in the continuum, U_p is the ponderomotive energy given by Eq. 2.4 and ω is the frequency of the laser field. In simulations the spatiotemporal intensity distribution of the laser focus has to be taken into account, as well as the depletion of negative ions.

CHAPTER 3

Methods of laser-ion experiments

"An experiment is a question which science poses to Nature, and a measurement is the recording of Nature's answer"

– Max Planck

In this chapter I describe and discuss the two complimentary experimental setups at Albert Ludwig's University and at University of Gothenburg. Negative ions are fragile systems and they would not survive if they were accelerated to a beam in atmospheric pressure. Therefore all our experiments are performed in ultra high vacuum. The pressure in the interaction region is on the order of 10^{-9} - 10^{-10} torr. The low pressure minimizes the background from electrons detached by collisions with residual gas in the interaction region. The negative ions are created in a commercially available sputter source [78], which is also in vacuum. Electrostatic deflection plates and lenses are used to steer and shape the ion beam. Due to impurities of the sample and residual materials in the vacuum system an ion source produces a range of elements at the same time. Therefore a mass selector is needed. At Albert Ludwig's University a Wien filter is used whereas GUNILLA is equipped with a sector magnet. Both systems have a 90° bend before the ions enter the interaction region to remove any neutrals present in the ion beam. The laser beams enter the interaction region through a window in the chamber. At Albert Ludwig's University photodetached electrons produced in the interaction region are detected. Time delay between the pump and the probe pulse is on a femtosecond time scale. At GUNILLA residual positive ions are detected using a position sensitive detector. The time delay between the pump and the probe pulse is on a nanosecond time scale. The two setups and detector systems are described in detail in section 3.1 and 3.2. Time resolved experiments investigating the dynamics of atoms and negative ions were

conducted in the laser lab at Albert Ludwig's University while studies of the structure and electron-electron correlations in negative ions and atoms were performed at (GUNILLA) in Gothenburg.

3.1 Femtosecond spectroscopy

The ion source and vacuum system used at Albert Ludwig's University was built by R. Reichle [77] and I. Yu. Kiyan. The system is depicted in Fig: 3.1. Negative ions are created in the sputter source [78], accelerated to 4,5 keV and mass selected in a Wien filter. In a Wien filter the ions travel through a magnetic field and an electric field, aligned perpendicular to each other. Mass selection is achieved by balancing the electric and magnetic forces for a certain mass, thus guiding only a specific ion through the filter. After mass selection the beam is bent by 90° in a quadrupole deflector to remove any neutral atoms or molecules present in the beam [76]. The ion beam is focused by an electrostatic lens in to the interaction region where it is intersected with the two laser beams. A typical ion current of 200 nA and beam waist of less than 1 mm is obtained in the interaction region.

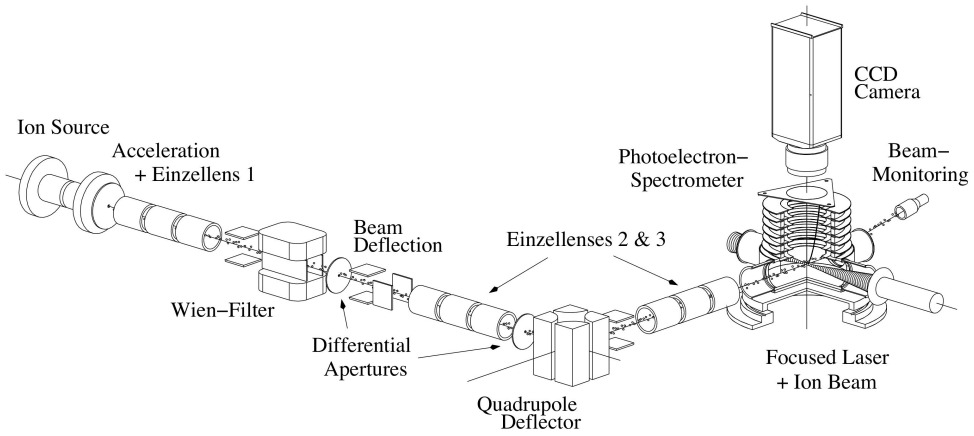

Figure 3.1: *Schematic view of the experimental setup at Albert Ludwig's University in Freiburg. A sputter ion source produces negative ions that are mass selected in a Wien filter. Ion optics guide and focus the ions in to the interaction region where the ion beam is intersected with two femto-second laser beams. Photoionized electrons are detected by an angular resolved electron imaging spectrometer (EIS) [75, 76]. Picture by R. Reichle [77].*

The interaction region is inside an Electron Imaging Spectrometer (EIS) [75, 76], shown in Fig. 3.2, operated in the velocity mapping regime

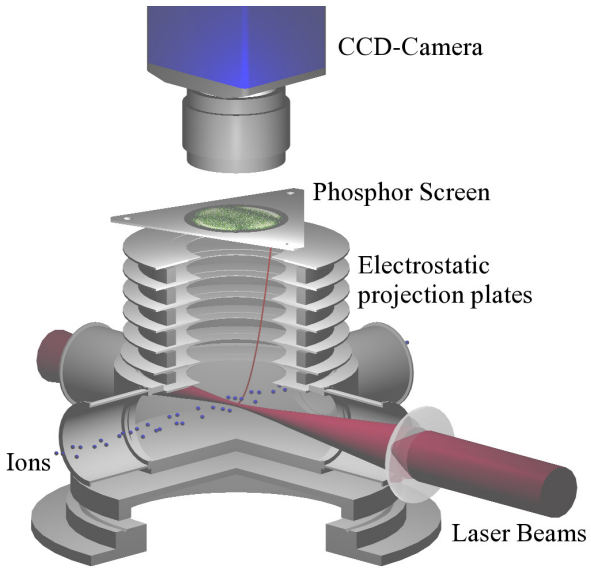

Figure 3.2: *Photoionized electrons are detected by our angular resolved electron imaging spectrometer (EIS) [75,76]. Picture by R. Reichle [77].*

[79]. The EIS consists of a set of electrodes projecting electrons emitted in the entire solid angle on to a stack of multichannel plates (MCPs). When an electron hits the MCP stack it creates an avalanche of electrons. A phosphor screen behind the MCPs gives of a light flash for each electron avalanche. The flash of light is detected by a CCD-camera. Velocity mapping means that electrons having the same momentum $\mathbf{p}$ are projected on to the same point on the detector, regardless of where in the focal volume they were ejected. This is achieved by a nonuniform projection field, as shown in Fig. 3.3.

A detached electron the interaction region with a certain momentum. Electrons of fixed energies expand as concentric spheres while being projected on to the detector. For a specific momentum p_n the radius of the expanding sphere is given by $r = p_n t/m_e$, where t is the expansion time and m_e is the electron mass. The density of electrons on the surface of the expanding sphere is given by the photodetachment probability, which can be highly dependent on the angle, θ, relative to the laser polarization. In experiments where linearly polarized light is used, the projected image has a cylindrical symmetry around the direction of the laser polarization. Two types of distortions arise during the projection of the expanding spheres [77,81]. In Fig. 3.4a a perfect parallel projection is depicted. However, since the projection time Δt is larger than zero, the back of the sphere will continue to expand dur-

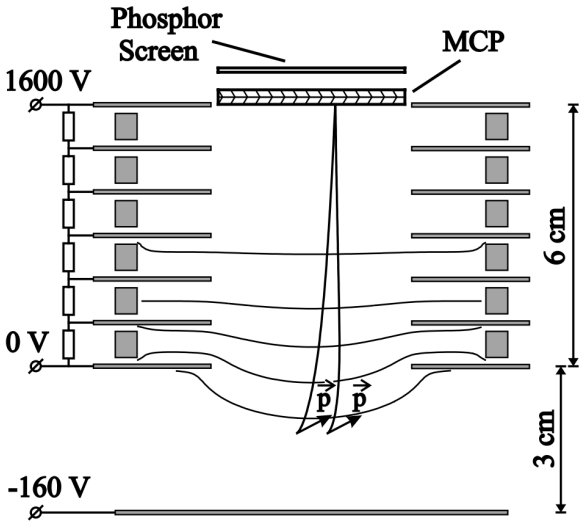

Figure 3.3: *Design of the EIS [75,77]. A nonuniform electric field projects electrons having the same momentum vector,* $\mathbf{p}$*, on to a single spot on the detector, regardless of the electron's exact origin. Representative equipotential curves as well as two electron trajectories shown in the figure. Picture by R. Reichle [77].*

ing Δt while the front is already mapped on to the detector, see Fig. 3.4b.

The projection time Δt is given by $\Delta t = 2v_0T/v$, where T is the time of flight from the interaction region to the detector for an electron emitted with zero momentum. $v_0 = p_n/m_e$ is the initial velocity of an electron with momentum p_n. If the projection time, Δt, is small compared to the time of flight, T, of the center of the sphere, the distortion is small. The distortion is larger for high energy electrons, where v_0 is large. The distortion can be related to the energy gained from the laser field, E_{p_n}, compared to the energy gained from the projection field $E_{projection}$. $\Delta t/T = 2/\sqrt{\rho}$, where $\rho = E_{p_n}/E_{projection}$. In Fig. 3.4b the distortion due to the expansion is depicted for three different projection parameter ρ. The ion beam has velocity of the order cm per microsecond, in the same direction as the laser polarization (Fig. 3.4a). This gives rise to another distortion as the sphere is translated while being projected. In Fig. 3.4c the translational distortion is depicted for projection parameters of ρ =1, ρ =10 and ρ =1000. A hard projection is desired to minimize distortion. However, a hard projection decreases the energy resolution. The sphere has less time to expand during the projection time and that the distance from the center to the point of impact on the detector becomes smaller. By increasing the flight distance to the detector the image is enlarged, and the energy resolution enhanced.

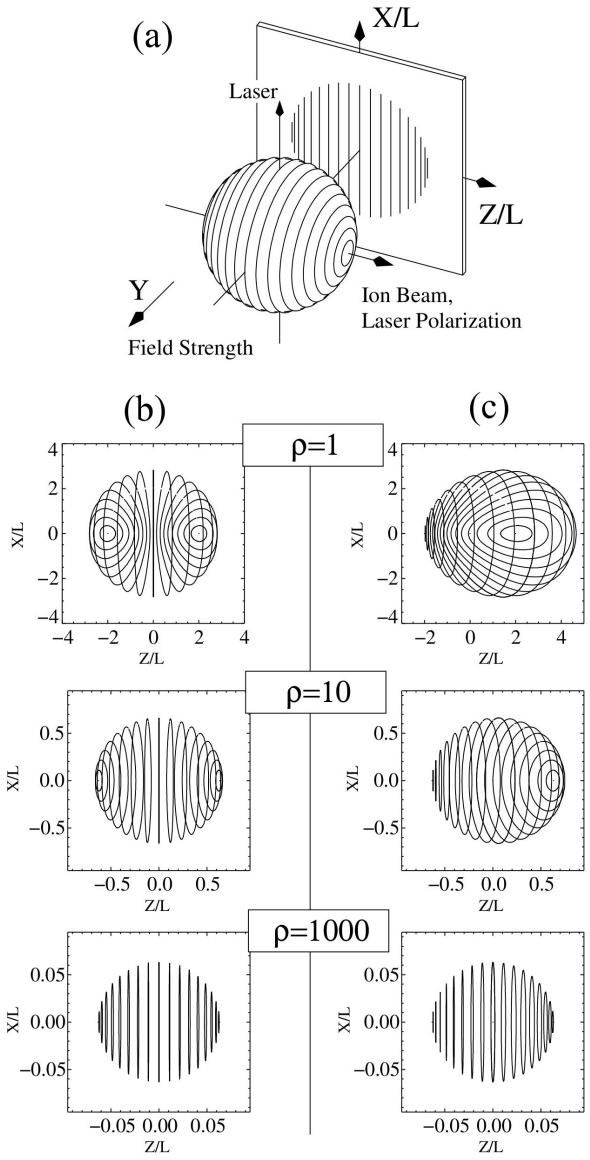

Figure 3.4: *(a)Ideal imaging, where the expanding sphere is mapped perfectly on to the detector. (b) Distortion due to expansion of the sphere during the projection time. (c) Distortion due to the translational motion from the velocity of the ion beam. In the experiments a projection parameter of approximately 1000 is achieved for our most energetic electrons. For less energetic electrons the parameter is larger. Picture by R. Reichle [77].*

More details on the EIS, and on image distortion and treatment can be found in [75,76].

The image recorded is a three dimensional distribution projected on to a two dimensional detector. Therefore some information lost. It is, however, possible to recreate the three dimensional distribution through a back projection. This is referred to as Abel inversion and is possible only if there is a symmetry present in the 3D angular distribution. In our experiments the angular distribution of photoelectrons is symmetric around the laser polarization direction, providing us with a well defined cylindrical symmetry. An Abel inversion routine known as "onion-peeling" [81] is used. We have applied the inversion on the data presented in chapter 4 and 5, where two dimensional cuts through the three dimensional distributions of photoelectrons are presented.

The laser system consists of a Ti:sapphire laser generating 100 fs long pulses of 800 nm at 1 kHz repetition rate. A traveling-wave optical parametric amplifier of superfluorescence (TOPAS) is pumped by the Ti: sapphire laser. TOPAS is tunable in the wavelength range 250 nm-2500 nm. The output of TOPAS is linearly polarized and consists of two colors, called *Signal* and *Idler*. The energy/wavelength of the incoming pump beam photons is split into two photons according to

$$\frac{1}{\lambda_{pump}} = \frac{1}{\lambda_{Signal}} + \frac{1}{\lambda_{Idler}} \tag{3.1}$$

When focusing the laser beam the peak intensity is on the order of $10^{13}-10^{14}$ W/cm^2. Figure 3.5 shows the beam paths of *Idler* and *Signal*. After TOPAS the two beams are separated using a beam splitter where *Signal* is transmitted while *Idler* is reflected on the surface as shown in Fig: 3.5. *Idler* passes through a telescope (b) where the divergence of the beam can be changed. The path length of the *Idler* beam can be altered by moving two mirrors placed on a motorized micrometer translation stage (c). With these mirrors the time delay between the two pulses is controlled on a femto second time scale. The polarization axis of both laser beams is controlled by means of two $\lambda/2$-plates (d). The two laser beams are merged again in a combiner (e), where *Signal* is reflected on the surface while *Idler* is transmitted. A negative lens (f) expands the laser beams before they are focused (g) in to the vacuum chamber to achieve a focus as small as possible. The problem of achieving a small laser focus is discussed in more detail later. The two laser beams are intersected with the ion beam inside an EIS where

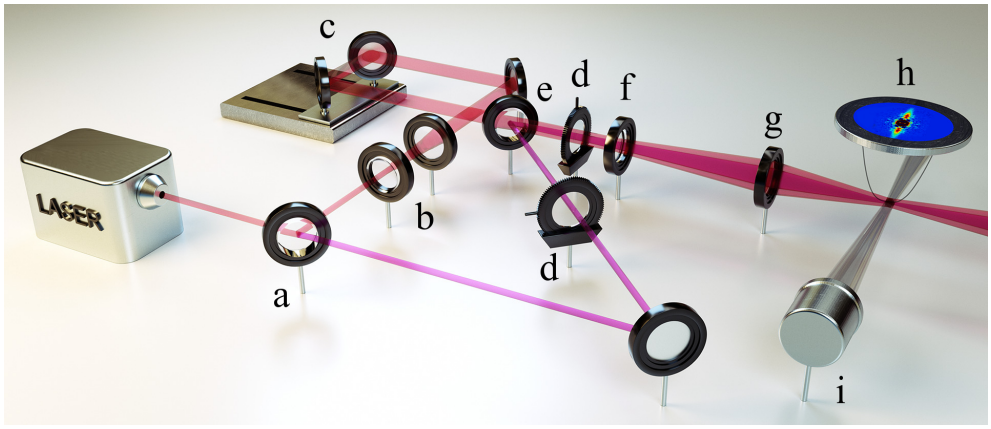

Figure 3.5: *Schematic view of the experimental setup. The probe and pump pulses are split in a dichroic mirror (a), and the pump beam divergence is controlled by a telescope (b). The time delay between pump and probe is controlled by a motorized micrometer translation stage (c). The polarizations of both beams can be rotated individually with two $\lambda/2$-plates, (d). The two laser beams are merged in a dichroic mirror (e). Both beams are expanded, (f), before focused into the interaction region with a 150mm focal length lens, (g), and intersected with the ion beam. Detached electrons are projected onto the position sensitive detector inside the EIS, (h). The ion current is measured using a Faraday-cup (i). Picture by Arvid Forsberg [87].*

the photodetached electrons are projected onto the position sensitive detector (h). The ion current is measured using a Faraday cup (i).

The optical setup was simulated using physical optics software [80] in order to optimize the peak intensity in the focus. In strong field experiments a short pulse length and a small focus size are desired in order to expose the species to an electric field as strong as possible. A simulation of the laser focus intensity is shown in Fig. 3.6. The Z-axis is the propagation axis of the light. There are a number of issues to be considered when a small laser focus is required. Chromatic aberrations in the focusing lens causes shorter wavelengths to diffract more and are thus focused earlier along the optical axis than longer wavelengths that are diffracted less. Chromatic aberration can be reduced using achromatic lenses. Such a lens is constructed by merging two lenses of different material and focal length. The difference in refractive index and focal lengths are matched to compensate for chromatic aberrations for a chosen pair of wavelengths. Spherical aberrations occur for rays passing through the lens close to its rim. The spherical shape of a lens surface causes these rays to diffract more, i.e. focus earlier, than rays passing through the center of the lens. Spherical aberration can be minimized by using aspheric lenses. Besides the two above mention

issues there is a fundamental physical limit of the spatial resolution of an optical system, refereed to as the diffraction limit. Light traveling through a slit or an aperture represented by the lens edge is diffracted. The diffraction gives rise to an interference pattern. In the case of a circular aperture light is focused to an airy disks pattern. The airy disk consists of concentric rings of light, stemming from constructive interference, around a central spot of light. The radial distance, d from the center of the spot to the first intensity minimum is a measure of the resolution of the optical system and is given by [82] as

$$d = 1.22\frac{\lambda f}{D}, \tag{3.2}$$

where λ is the wavelength, f is the focal length of the lens and D is the aperture or beam size. In the current setup the shortest focal length that can be used is defined by the distance from the window of the vacuum chamber to the interaction region in the center of the EIS. The wavelength λ is chosen depending on the electron affinity of the negative ion under investigation. The sole parameter to be adjusted to minimize the foci is the diameter, D, of the laser beam. As mentioned earlier, the laser beams are expanded by a negative lens before being focused into the interaction region.

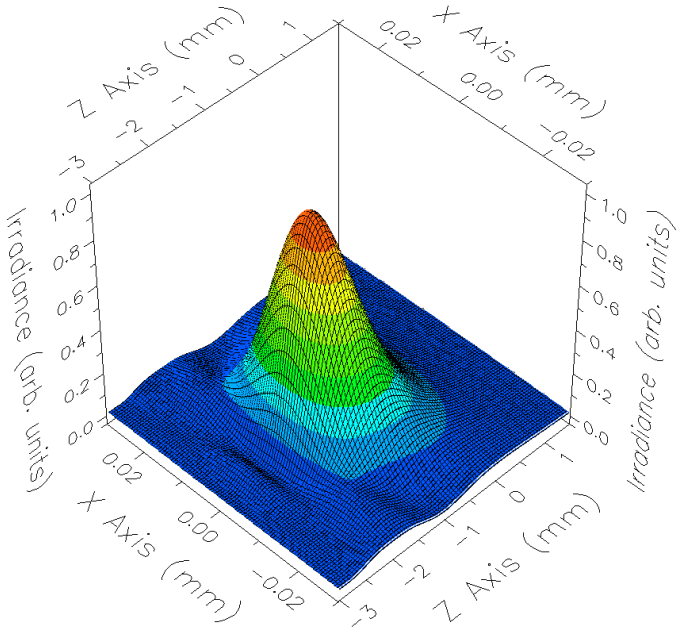

Figure 3.6: *Simulation of the laser focus intensity using physical optics software [80]. The Z-axis is the propagation axis of the laser pulse.*

A close up of the interaction region is shown in Fig: 3.7. The *Idler* beam is used as a pump and the *Signal* beam as a probe. The pump

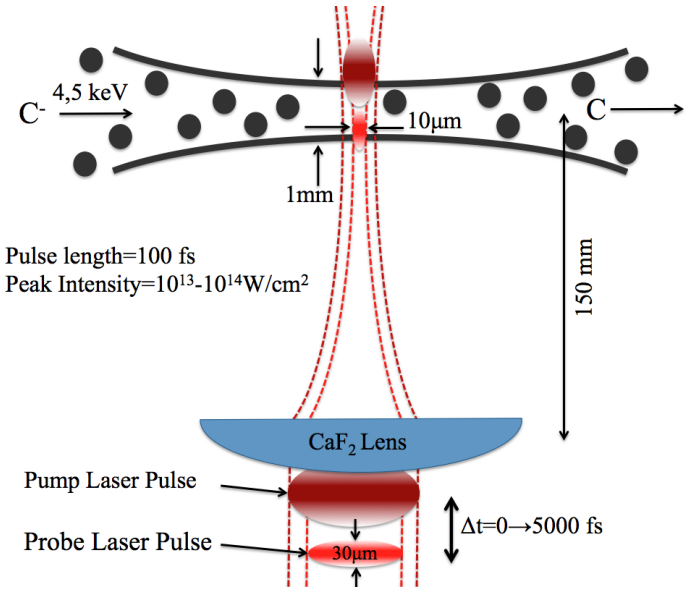

Figure 3.7: *Schematic view of the interaction region. The pump and the probe pulses are overlapped and focused into the ion beam by a 15cm focal length CaF_2 lens.*

pulse is spatially larger than the probe pulse. See Fig: 3.7. The beam waist of the ion beam is typically less than 1 mm. The Full Width at Half Maximum (FWHM) of the pump pulse focus is 26 μm while the FWHM of the probe pulse focus is 17μm. The probe pulse focus is kept small to ensure that only ions that have been exposed to the pump pulse are probed. Extensive work has been put in to developing a method to overlap the two laser beam foci with the ion beam focus. The pump pulse focus has to be placed in the center of the focused ion beam where the density of ions is maximal. Subsequently the probe pulse should be focused in to the center of the pump focus. A razor blade is scanned across the laser beams individually while recording the intensity of the laser light that passes by. The intensity drops as the blade is slowly scanned across the focus. An error function is fitted to the curve providing us with the size of the focus at the position of the razor blade. The razor blade is then scanned across the beam a several positions along the optical axis, thus giving us the position and size of the focus as well as the Rayleigh length. As mentioned before the pump pulse and probe pulse have different focal lengths due to chromatic aberrations of the lens. The telescope in the pump beam path is used to compensate by changing the divergence of the pump beam to overlap the two laser beams along the optical axis.

The construction of a new diagnostic setup was essential to monitor the overlap of laser foci. A wedge was placed after the focusing lens to

split of a fraction of the laser light and steer it on to a off-axis parabolic gold mirror with a focal length of 2.5cm. The light is reflected by the mirror into a CCD camera. The laser focus is imaged by placing the focal point of the gold mirror at the laser focus. Two of the mirrors in the pump beam path are controlled by piezo-electric motors. Using these two mirrors the pump beam with the probe beam is overlapped by means of visual inspection via the CCD camera. Optimization of the overlap between the laser focus and the ion beam focused is carried out by monitoring the signal from the detached electrons in the EIS.

3.2 Structure studies of negative ions

GUNILLA is also equipped with a sputter ion source. After acceleration the ion beam is mass selected in a sector magnet (Fig: 3.8). The sector magnet is bending the beam 90°. The magnetic field is tuned to only guide a specific mass through the magnet. When studying molecular ions a mass resolution of $m/\Delta m = 800$ is achieved and for monoatomic ions $m/\Delta m = 500$ [138]. The beam is bent 90°, to remove neutrals created through collisions with the background gas, before entering the interaction chamber. The ion beam and laser beams travel together through a 60 cm long interaction chamber in a collinear setup. Two laser systems, configured in a resonant ionization scheme, is used to investigate the cross section and threshold behavior in photodetachment of K^- and Cs^-.

A doubly excited state is created in the negative ion by absorption of a single UV-photon. The UV photons are generated in an OPO pumped by a Nd:Yag laser at a repetition rate of 10 Hz and a pulse energy of 0.7 mJ. The OPO is tunable in the range 220 nm to 1800 nm. The excited ion is then given time to decay. In the decay process all energetically available states in the atom can be populated, see Fig. 3.9. To probe the cross section for decay in to a specific state in the atom an IR laser is used to excite that state in the atom to a high Rydberg state. The IR laser consists of a 10 Hz Nd:Yag pumped OPO tunable in the range 1350 nm to 5000 nm with a pulse energy of 0.2 mJ. The high Rydberg state is subsequently ionized, in the field ionizer, forming a positive ion, see Fig. 3.10. The positive ion is deflected on to the position sensitive detector, see Fig 3.11.

Doubly excited states in negative ions are mapped out by scanning the wavelength of the UV laser over an extended energy range. The IR

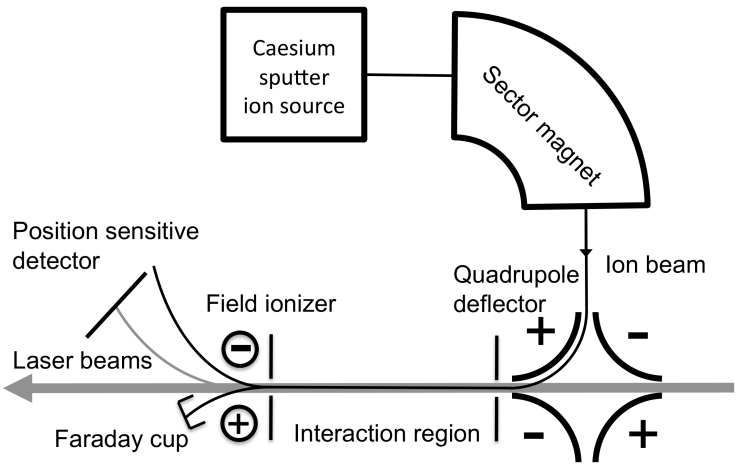

Figure 3.8: *Schematic view of the GUNILLA setup in Gothenburg [86]. Negative ions are created and accelerated in a cesium sputter ion source, mass selected in a sector magnet, deflected in to the interaction region where they travel in collinear geometry with the two laser beams. The excited Rydberg atoms are field ionized and detected on our position sensitive detector. The ion current is monitored by a faraday cup.*

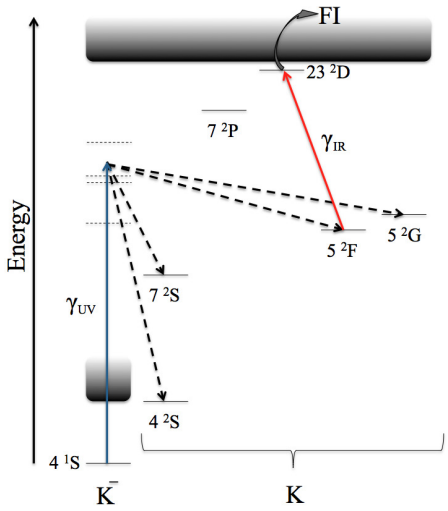

Figure 3.9: *Resonant ionization scheme used when investigating K^-. The γ_{UV} photon performs a double excitation of the negative ion which subsequently decays and populates all energetically available states in the neutral atom. The γ_{IR} photon is tuned to probe a specific state in the neutral atom. γ_{IR} photon promotes the atom in to a Rydberg state that is subsequently field ionized and the residual positive ion is detected [86].*

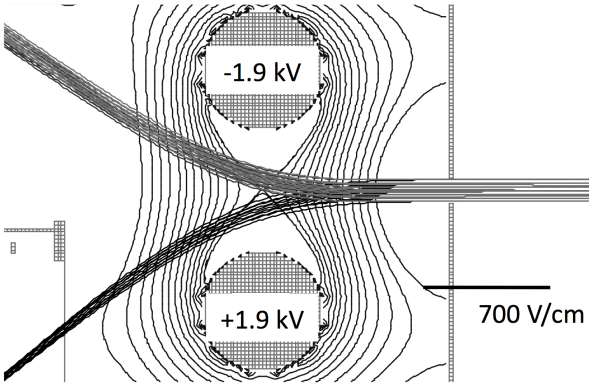

Figure 3.10: *A close up of the field ionizer. The contours represent lines of equal field strength. Different Rydbergs states have distinct ionization energies and are therefor field ionized at separate positions in the field and thus deflected onto spatially separated positions on the detector. Negative ions are deflected downwards in the picture, into a Faraday cup. Picture by A. O. Lindahl.*

laser is kept at a fixed wavelength, matching the energy needed to excite the atomic state of interest up to a Rydberg state. In Fig: 3.9 the resonance ionization scheme used in chapter 8 and 9 is presented. The figure depicts the case where doubly excited states in K^- are investigated. The same method is applicable to Cs^-, which is done in chapter 10. When the γ_{UV} wavelength is scanned over the threshold for reaching a specific state in the neutral atom that state gets populated and an increase in signal of positive ions is observed. The shape of this threshold tells us about the electron-electron correlations and the polarizability of the state of interest in the atom. The doubly excited states in the negative ion shows up as resonances in the measured cross section. During the scan over an doubly excited state the probability of detachment is modulated and the rate of negative ions decaying in to a neutral atom is increased. Rydberg states of different energy are field ionized a different field strengths, i.e. at different positions in the field ionizer. When the positive ion is deflected on to the detector, its path is dependent on where it was field ionized. Hence, different Rydberg states are separated spatially on the detector. One such path is depicted as path b in Fig. 3.11. Positive ions created already in the interaction region, through absorption of two UV-photons are deflected already from the start of their path through the field ionizer, see path a in Fig: 3.11. Negative ions follow path c in Fig: 3.11 and are measured in the Faraday cup.

The position sensitive delay line detector [88, 89] consists of two long copper wires winded around a frame forming a grid. A multi channel

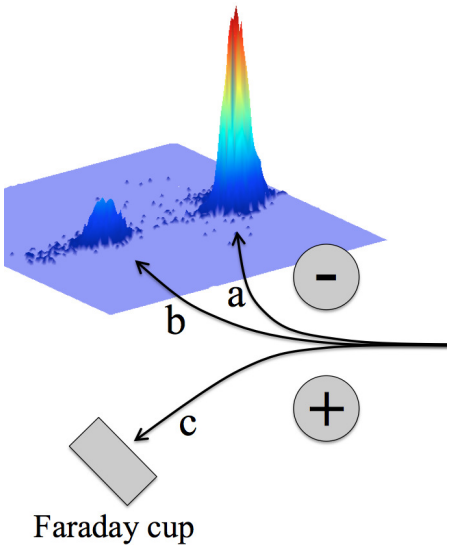

Figure 3.11: *Positive ions, created in the interaction region through absorption of two UV-photons, follow path a. Rydberg atoms ionized in the field ionizer will follow path b. The exact impact position on the detector is dependent on the Rydberg state being measured. Rydberg states have different energies and will be ionized at slightly different positions and thus deflected on to distinguishable areas on the detector. The ion current is measured by deflecting the negative ions into a Faraday cup.*

plate (MCP) stack is placed in front of the grid. The delay lines pick up the electron avalanche from the MCP and an electric pulse is formed traveling towards the two ends of each copper wire. By measuring the difference in arrival time of the electrical pulse at the two ends of the wire the position of impact on that wire is determined. Two wires are enough to unambiguously specify the point of impact on the detector surface. The timing is measured by a Time To Digital Converter (TDC) with an accuracy of 25 ps. The diameter of the active are of the detector is 40 mm, and a spatial resolution better than 0.1 mm is achieved. The detector system has a dead time of 10-20 ns.

The energy supplied by each γ_{UV} photon is large enough to start an avalanche of electrons in the MCP stack. In each laser pulse scattered γ_{UV} photons in the chamber saturate the detector for microseconds, making it impossible to detect positive ions. This problem is circumvented by switching on the voltage over the MCP only after the laser pulse has traveled through the chamber. The switching takes a mere 0.5 μs while the flight time for the positive ions from the interaction region to the detector is 2-6 μs. The direct peak of negative ions originating from sequential double detachment by the γ_{UV} pulse is two orders of magnitude larger than the observed Rydberg peaks. Satura-

tion of the detector by the direct peak is avoided by tuning the field ionizer to steer the direct peak outside of the active area of the detector (Fig. 3.11). The number of positive ions is recorded as a function of the γ_{UV} wavelength. The yield of positive ions is normalized for varying experimental parameters therefore the ion current, UV wavelength and the UV pulse energy for each laser pulse are recorded. The γ_{IR} induced transition from the monitored state in the atom to the Rydberg state is resonant and therefor saturated in our case, no normalization for varying γ_{IR} pulse energy is done.

CHAPTER 4

Electron Rescattering in Above-Threshold Photodetachment of Negative Ions

A. Gazibegović-Busuladžić [1], D. B. Milošević [1,2], W. Becker [2]
[1]*Faculty of Science, University of Sarajevo, Zmaja od Bosne 35, 71000 Sarajevo, Bosnia and Herzegovina*
[2]*Max-Born-Institut, Max-Born-Str. 2a, D-12489 Berlin, Germany.*

B. Bergues, H. Hultgren & I Yu. Kiyan
Physikalisches Institut, Albert-Ludwigs-Universität, D-79104 Freiburg, Germany

published in Physical Review Letters **104**, 103004 (2010).

We present experimental and theoretical results on photodetachment of Br^- and F^- in a strong infrared laser field. The observed photoelectron spectra of Br^- exhibit a high-energy plateau along the laser polarization direction, which is identified as being due to the rescattering effect. The shape and the extension of the plateau is found to be influenced by the depletion of negative ions during the interaction with the laser pulse. Our findings represent the first observation of electron rescattering in above-threshold photodetachment of an atomic system with a short-range potential.

The rescattering of a photoelectron on its parent core represents a fundamental effect that lies in the focus of recent investigations in the field of the nonlinear interaction of atoms and molecules with strong laser radiation. An electron liberated by photoionization moves in the presence of the laser field. Driven by a field of linear polarization, it may revisit the parent core. Its recollision with the core gives rise to processes such as high-order above-threshold ionization (HATI), high-order harmonic generation, and nonsequential multiple ionization (see the review articles [92, 93] and references therein).

The HATI process, which represents the subject of the present work, manifests itself in photoelectron spectra as a high-energy plateau stretching along the laser polarization axis. On the energy scale this plateau extends up to (and has a cutoff at) approximately $10U_{\mathrm{p}}$, where U_{p} is the electron ponderomotive energy in the laser field. The HATI process was found to be initiated by elastic rescattering of the photoelectron on its parent core, where the highest kinetic energy is reached via backscattering [94]. More recently, the HATI process has received much attention in the context of attophysics [95], as a means to measure the carrier-envelope phase of a few-cycle laser pulse in a single shot [96], and also since it allows one to extract the differential cross sections for elastic electron scattering off positive ions from the experimental angle-resolved photoelectron spectra [97].

While the rescattering effect has been widely studied in atoms and molecules, its role in negatively charged ions remains essentially unexplored [98]. One might expect the manifestation of rescattering in above-threshold photodetachment of negative ions to be different. The short-range character of binding forces in negative ions precludes the Coulomb focusing of the electron wave packet created in the continuum. Coulomb focusing was shown to enhance the rescattering probability [99]. On the other hand, the lower binding energy of negative ions implies a larger initial size of the electron wave packet and, consequently, its slower spreading between the instants of ionization and rescattering. Whether or not these features result in a significant modification of the HATI process represents a fundamental question. In the present work we report on the first observation of the rescattering plateau in above-threshold photodetachment of negative ions.

4.1 Methods

Early experiments on strong-field photodetachment were hampered by depletion of the negative-ion sample at the leading edge of the laser pulse. This problem was overcome by using a short laser pulse of infrared wavelength and, thus, by reaching the saturation condition of photodetachment at a significantly higher intensity. First experiments with infrared pulses of 100 fs duration were performed by our group on H^- [75,76] and F^- [64,71]. The peak intensity was of the order of 10^{13} W/cm^2. Though electrons of rather high kinetic energies were detected in [64,71], the dynamic range of the signal, limited to 2.5 orders

of magnitude, did not allow us to distinguish a rescattering contribution from the experimental background. The results were described well by using a Keldysh-like theory [69] that considers the direct detachment only.

In the present work we investigate photodetachment of Br^-. Our study is motivated by the recent prediction that the ratio of the rescattering signal to the signal of direct electrons is higher for the heavier halogen negative ions, Br^- and I^- [90, 91]. Intuitively, heavier elements have a larger core, which gives rise to a larger elastic scattering cross section. Recently we reported on photodetachment of Br^- in a laser field of 800 nm wavelength and 6×10^{14} W/cm^2 peak intensity [72]. A jet of energetic electrons along the laser polarization axis, resembling a rescattering plateau, was observed in the measured spectra. This jet, however, was found to be due to sequential double detachment. If there was any yield from the rescattering process, it was masked by the dominant double-detachment signal. In the present work the contribution of sequential double detachment is suppressed by exposing Br^- to radiation of a longer wavelength of 1300 nm. At this wavelength the nonlinearity of the double detachment process is much higher and the signal arising from sequential double detachment lies far below the noise level of the measured spectra.

Our experimental setup is described elsewhere [64,72,75,76]. Briefly, a mass-selected beam of negative ions is intersected with the laser beam inside an electron imaging spectrometer (EIS) operated in the velocity mapping regime. Linearly polarized infrared laser pulses of 1300 nm wavelength are generated in an optical parametric amplifier (OPA) pumped with a mode-locked Ti:sapphire laser system at a repetition rate of 1 kHz. The output of the OPA is focused with a 15 cm focal length lens into the interaction region. A focus size of 40 μm (FWHM) and a pulse duration of 100 fs (FWHM) are measured with the use of our beam diagnostic tools. Assuming a Gaussian shape of the spatio-temporal intensity distribution, the peak intensity in the focus is determined to be 6.5×10^{13} W/cm^2. The image processing involves a conventional Abel inversion routine to reconstruct the angle-resolved momentum distribution of the photoelectrons emitted from the laser focus. The momentum/energy resolution of the EIS is determined by measuring the detector response function to a single electron event. The energy resolution is 0.23 eV at the energy of 1 eV, and it varies proportionally to the square root of the kinetic energy.

4.2 Theory

We analyze the measured spectra in terms of the rescattering theory developed in Ref. [90, 91]. This rescattering theory is an extension of the Keldysh-Faisal-Reiss theory [65, 68] and yields a first-order correction to the strong-field approximation (SFA). In the standard SFA, the interaction of the photoelectron with the residual core is neglected. This approximation is particularly suitable for the description of photodetachment of negative ions due to the absence of the long-range Coulomb potential, which is experienced by the outer electron in atoms. However, even for negative ions a photoelectron, driven back into the inner region of the binding potential, may interact with the atomic core. The rescattering theory of Ref. [90, 91] allows for such an interaction. A closely related approach was formulated in Ref. [100] and successfully applied to photodetachment of F^- [101].

Let us stress the main aspects of this rescattering theory. The probability amplitude to detach an electron with a drift momentum $\mathbf{p}$ is defined by the matrix element [93]

$$M_{\mathbf{p}i} = -i \lim_{t\to\infty} \int_{-\infty}^{t} dt' \langle \psi_{\mathbf{p}}(t)|U(t,t')\mathbf{r}\cdot\mathbf{E}(t')|\psi_i(t')\rangle, \tag{4.1}$$

where $U(t,t')$ is the time-evolution operator of the Hamiltonian $H(t) = -\boldsymbol{\nabla}^2/2 + \mathbf{r}\cdot\mathbf{E}(t) + V(\mathbf{r})$, $\mathbf{r}\cdot\mathbf{E}(t)$ is the laser-field–electron interaction given in the length gauge and dipole approximation, and $V(\mathbf{r})$ is the electron–atom interaction in the absence of the laser field. The wave functions $\psi_{\mathbf{p}}$ and ψ_i describe the final state with the drift momentum $\mathbf{p}$ and the initial state, respectively. As discussed in detail in Ref. [69], ψ_i can be represented in the asymptotic form $\psi_{\ell m}(\mathbf{r}) = (A/r)\exp(-\kappa r)Y_{\ell m}(\hat{\mathbf{r}})$, where A is a normalization constant, $E_{\rm a} = \kappa^2/2$ is the binding energy, and ℓ, m are the angular-momentum quantum numbers of the initial state. The time-evolution operator $U(t,t')$ satisfies the Dyson equation

$$U(t,t') = U_{\rm L}(t,t') - i\int_{t'}^{t} dt'' U_{\rm L}(t,t'')V(\mathbf{r})U(t'',t'), \tag{4.2}$$

where $U_{\rm L}(t,t')$ is the time-evolution operator of the Hamiltonian $H_{\rm L}(t) = -\boldsymbol{\nabla}^2/2 + \mathbf{r}\cdot\mathbf{E}(t)$ of a free electron in the laser field. We now make two approximations: on the right-hand side of Eq. (4.2) we replace U with $U_{\rm L}$, and in Eq. (4.1) we replace the final state $\langle\psi_{\mathbf{p}}(t)|$ by a plane wave.

The state $\langle\psi_{\mathbf{p}}(t)|U_{\mathrm{L}}(t,t')$ then becomes the Volkov state $\langle\psi_{\mathbf{p}}^{(L)}(t')|$ (eigen state of a free electron in the external laser field), and we obtain

$$M_{\mathbf{p}i}^{\mathrm{SFA}} = -i\int_{-\infty}^{\infty} dt\langle\psi_{\mathbf{p}}^{(\mathrm{L})}(t)|\mathbf{r}\cdot\mathbf{E}(t)|\psi_i(t)\rangle$$
$$-\int_{-\infty}^{\infty} dt\int_{t}^{\infty} dt'\langle\psi_{\mathbf{p}}^{(\mathrm{L})}(t')|VU_{\mathrm{L}}(t',t)\mathbf{r}\cdot\mathbf{E}(t)|\psi_i(t)\rangle. \tag{4.3}$$

The first term on the right-hand side of Eq. (4.3) represents the probability amplitude of direct detachment (the standard SFA), while the second term describes the (first-order Born approximation) rescattering amplitude. It is the second term that gives rise to the high-energy plateau in the electron energy spectrum [90, 91]. For above-threshold detachment off a negative ion – in contrast to above-threshold ionization of an atom – we expect Eq. (4.3) to yield a quantitatively reliable description.

The rescattering amplitude is dependent on $V(\mathbf{r})$, which is specific for a given negative ion. The potential $V(\mathbf{r})$ can be modeled by the double Yukawa potential [73]

$$V(r) = -\frac{Z}{H}\frac{e^{-r/D}}{r}\left[1+(H-1)e^{-Hr/D}\right]. \tag{4.4}$$

Here $H = DZ^{0.4}$, Z is the atomic number and D is a numerical parameter. For bromine $Z = 35$, $D = 0.684$ and, for comparison, for fluorine $Z = 9$, $D = 0.575$ [102]. The potential (4.4) has a static character and does not include polarization effects. It was shown in [90,91] that these effects are not significant for electron rescattering at high kinetic energies. Therefore, for the sake of simplicity we use the static potential and demonstrate below to which extent the difference in the parameters Z and D for Br^- and F^- affects the rescattering signal from these negative ions.

For a fixed laser intensity I and frequency ω, the energy spectrum of photoelectrons consists of a series of discrete peaks at energies $E_{\mathbf{p}} \equiv \mathbf{p}^2/2 = n\omega - E_{\mathrm{a}} - U_{\mathrm{p}}$ with $n \geq n_{\mathrm{min}}$, where $U_{\mathrm{p}} = I/(4\omega^2)$ and n_{min} denotes the minimum number of photons needed to overcome the ponderomotively shifted detachment threshold. For a detailed comparison with the experimental results, the electron spectrum has to be averaged over the spatio-temporal intensity distribution in the laser focus. Since the intensity in our experiment is far above the saturation value, the depletion of the negative ions during the interaction with the laser pulse also needs to be taken into account [64, 71, 76]. Details

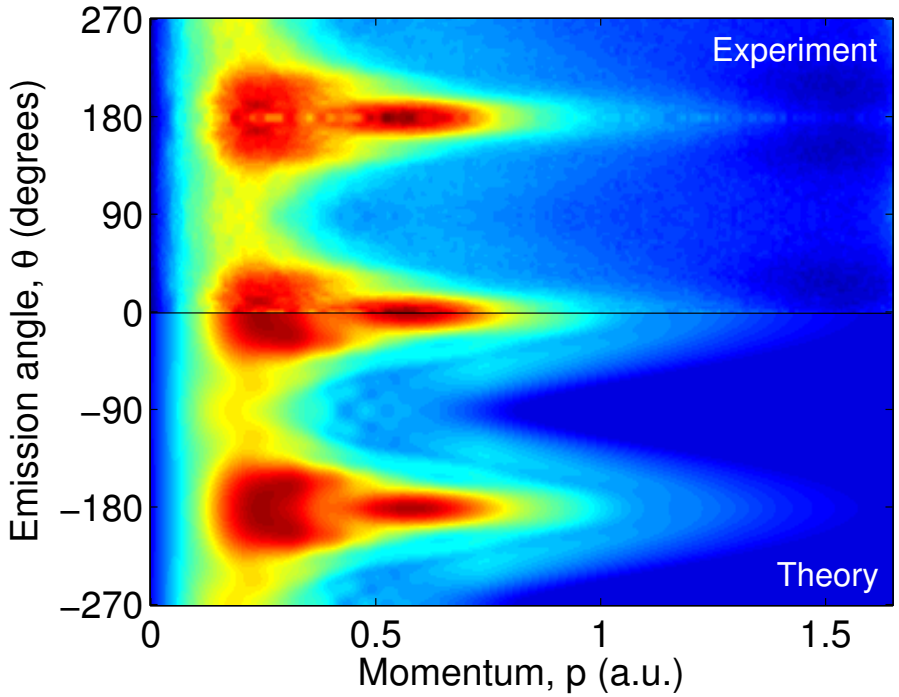

Figure 4.1: (color online) Angle-resolved momentum distribution of photoelectrons detached from Br^- in a laser field of 1300 nm wavelength and 6.5×10^{13} W/cm^2 peak intensity. Upper part ($0° \leq \theta \leq 270°$): experimental results; lower part ($-270° \leq \theta \leq 0°$): predictions by the rescattering theory.

on the simulation routine will be presented elsewhere. The experimental energy resolution is taken into account by convolution of the simulated spectra with the measured response function of the detector to a single electron event.

4.3 Results

Our experimental results and the predictions by the rescattering theory are presented in the upper and lower part of Fig. 4.1, respectively. The figure shows the measured and calculated photoelectron distributions in the (p, θ) coordinates, where p is the electron momentum and θ is the emission angle with respect to the laser polarization axis. Despite the limited signal-to-noise ratio at low signal and the presence of background in the experimental spectrum, Fig. 4.1 demonstrates good agreement between experiment and theory.

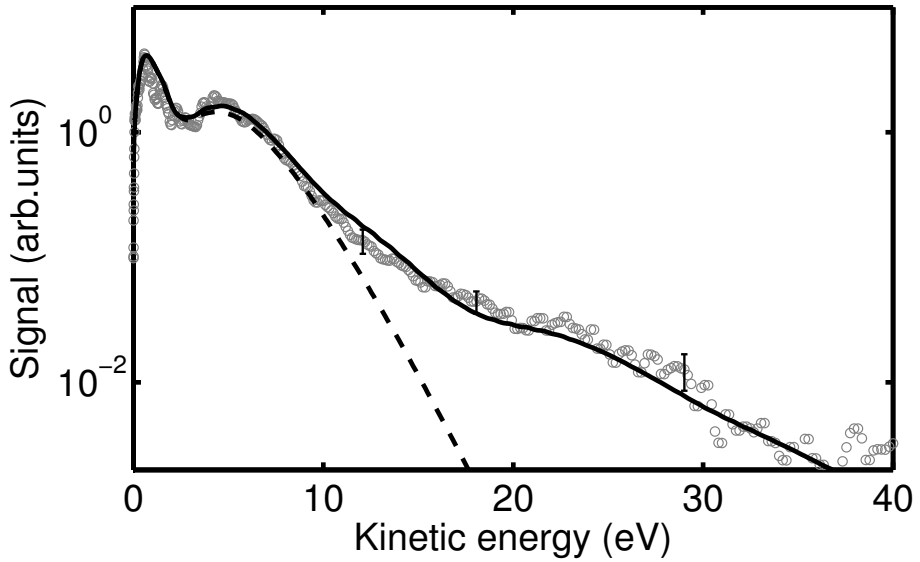

Figure 4.2: Electron energy distributions along the laser polarization axis obtained from the spectra shown in Fig. 4.1. Circles: experiment; solid line: predictions with rescattering taken into account. The dashed line shows the predictions for the direct electrons only. The theoretical distributions are normalized to the experimental data at the maximum of the signal. Error bars of a few experimental data points are shown.

In the following discussion we focus on electron detachment along the laser polarization axis, where the rescattering contribution is most pronounced. The measured and simulated kinetic-energy spectra of electrons emitted at $\theta = 0^\circ$ are presented in Fig. 4.2. Here we also show results of simulations where rescattering is not taken into account. These are obtained by disregarding the second term in Eq. (4.3) that describes the rescattering amplitude. Comparison of the results in Fig. 4.2 clearly demonstrates that rescattering contributes to the yield of electrons with kinetic energies higher than 10 eV. At this energy the experimental curve changes its slope and starts deviating considerably from the predictions for the direct electrons, while it is well reproduced by the predictions with rescattering taken into account. The rescattering signal dominates in the spectrum at energies higher than 15 eV and appears well pronounced in the range up to approximately 35 eV. Beyond this value it becomes indistinguishable from the experimental background. In the intermediate range between 10 and 15 eV both the direct-detachment and the rescattering amplitudes in Eq. (4.3) are significant and interfere. In this region the slope changes gradually to a smaller value, which characterizes the "plateau".

The upper energy limit of the observed spectrum, however, is much lower than the cutoff energy of $10U_{\mathrm{p}}$, which has a value of 103 eV for the measured peak intensity. The signal of rescattered electrons continuously decreases with increasing energy, forming an inclined plane rather than a plateau. Such an unusual manifestation of the rescattering plateau is found to be due to strong saturation of the photodetachment process. Indeed, by tracing in our simulations the population density of negative ions during the interaction with the laser pulse, we obtain that only 1% of the ions in the laser focus survive until the intensity reaches the value of 3×10^{13} W/cm^2, which is still a factor of 2 lower than the measured peak intensity. In other words, only a very small number of negative ions are practically exposed to the peak intensity. Integration of the product of the population density and the photodetachment rate over the focal region results in the inclined-plane shape of the rescattering signal without a pronounced cutoff energy. It follows from this discussion that the condition of strong saturation makes the peak intensity less crucial. This has also been verified by performing simulations for different peak intensities that differ from the measured value by up to 30%, which is our estimate for the intensity error bar. The variation of the peak intensity does not cause significant changes in the predicted spectra.

Let us consider, for comparison, photodetachment of F^- whose rescattering potential (Eq. 4.4) is described by different parameters Z and D. The smaller values of the parameters Z (smaller potential depth) and D (steeper decrease of the potential with the increase of r) reflect the smaller size of the fluorine atom as compared to the bromine atom. Results on photodetachment of F^- in a strong infrared laser field have been presented before [64, 71]. Here we present new data obtained for F^- at the wavelength of 1300 nm, as used in the experiment on Br^-. Because of a different optics alignment (focus size of 45 μm, pulse duration of 133 fs), the value of the peak intensity in this measurement was 3.4×10^{13} W/cm^2. Fig. 4.3 shows measured and calculated energy distributions of electrons emitted along the laser polarization axis. The two predicted distributions are obtained with and without taking rescattering into account. Only the onset of the rescattering signal in the energy range between approximately 15 and 22 eV can be distinguished from the noise in the measured spectrum. Except for this range, the predicted rescattering plateau, which again looks more like an inclined plane, lies below the experimental background. One should note that the dynamic range of the signal is the same in both F^- and Br^- data and is restricted to approximately three orders of magnitude. This prevents us from studying the rescattering effect in F^-.

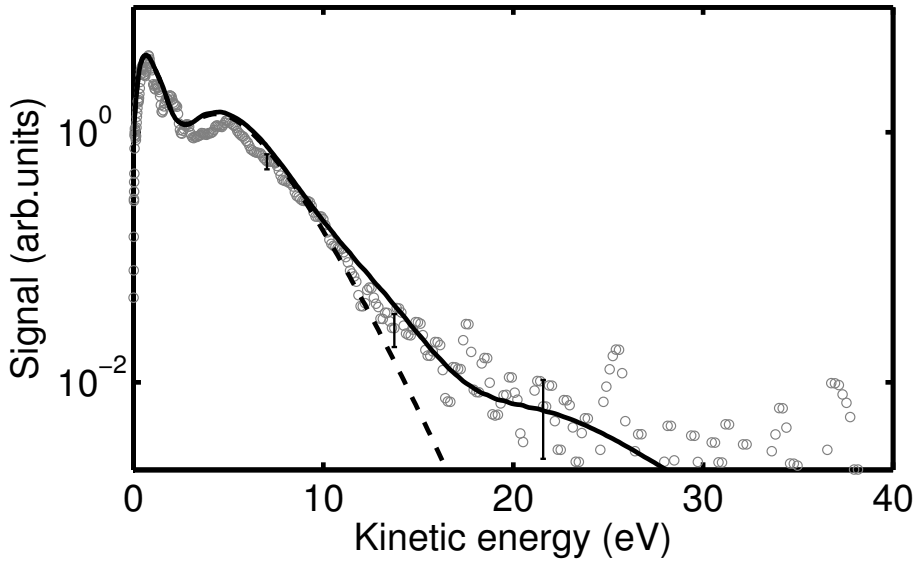

Figure 4.3: Same as Fig. 4.2 but for F^-. The laser wavelength is 1300 nm and the peak intensity is 3.4×10^{13} W/cm^2.

The smaller contribution of the rescattering effect in F^- as compared to Br^- is a consequence of the smaller size of the fluorine core. This is in accord with the predictions of Ref. [90,91].

In conclusion, we reported on the first observation of the HATI process in negative ions. The shape of the rescattering signal is found to be strongly affected by saturation of the photodetachment process. Because of saturation, the rescattering plateau assumes the form of an inclined plane. This fact reflects the fragility of negative ions compared to atoms and positive ions. Because of a larger core, the rescattering contribution to the spectrum is larger for heavier elements. This makes observation of rescattering effects easier in Br^- than in F^-.

The authors greatly appreciate fruitful discussions with Professor Hanspeter Helm. This work is supported in part by the Federal Ministry of Education and Science, Bosnia and Herzegovina and by the Deutsche Forschungsgemeinschaft, Grant No. KI 865/1-3.

CHAPTER 5

Photodetachment dynamics of F_2^- in a strong laser field

Hannes Hultgren & Igor Yu. Kiyan

Physikalisches Institut, Albert-Ludwigs-Universität, D-79104 Freiburg, Germany

published in Physical Review A **84**, 015401 (2011)

The angle-resolved photoelectron spectrum of F_2^-, exposed to a strong infrared laser pulse, is significantly different from the spectrum of F^- obtained at the same experimental conditions. The experimental results are used to test the theory based on the molecular strong-field approximation. Both the dressed and undressed versions of this theory fail to reproduce the F_2^- spectrum. One origin for this discrepancy is that photodetachment of F^- produced by strong-field dissociation of F_2^- needs to be considered.

Ionization of atoms and molecules in a strong laser field represents a hot topic of recent studies on nonlinear interaction of matter with laser radiation. At high laser intensities, the photoelectron can gain substantially more energy from the field than necessary to overcome the ionization threshold. This gives rise to an above-threshold ionization (ATI) structure in electron emission spectra [92, 93]. The energy spectrum is characterized by the electron ponderomotive energy U_p, which represents the kinetic energy of the electron quiver motion in the field averaged over the optical cycle. Angle-resolved photoelectron spectra carry valuable information used to identify mechanisms that govern the ionization process. For instance, the electron rescattering on its parent core is found to be responsible for the energy plateau, stretching along the polarization axis of a linearly polarized field, with a cut-off energy of $10U_\mathrm{p}$. As another example, the non-monotonic structure

in angle-resolved spectra reveals the effect of quantum interference, which was clearly observed in recent experiments on strong-field photodetachment of atomic negative ions [64, 71].

Among theories developed for description of the ionization process, the theory based on the strong-field approximation (SFA) [65] is most fascinating, combining power of prediction and simplicity. The approximation consists of neglecting the core potential in the final state. The final state is then represented by a Volkov wave function [66]. The SFA theory enables us to describe the phenomenon of ionization on a fundamental level, relating it to a coherent superposition of electron trajectories in the continuum [69, 70, 91]. In particular, the effect of quantum interference is intrinsically included in the final expression describing the ionization rate. In fact, the SFA theory was used in [64, 71] to identify this effect in photoelectron spectra.

The SFA theory was recently extended to describe ionization of diatomic molecules [171–173]. Additional parameters, such as the molecular orientation and the symmetry of the initial electronic state, need to be considered in this case. The presence of two centers in a diatomic molecule gives rise to additional interference, related to a superposition of electron waves emitted from different centers. The dressing of the initial electronic state by the field represents an important issue here [173]. Similar to the standard atomic SFA, the undressed version of the molecular SFA [171–173] neglects the laser field in the initial state. Its dressed version is formulated in [173] by accounting for the difference in the electron potential energy at the two centers in the presence of the laser field. The dressing results in the phase shift $e^{i\mathbf{R}\cdot\mathbf{k}(t)}$ between waves emitted from different centers, where $\mathbf{R}$ is the internuclear distance, $\mathbf{k}_t = -e\int^t \mathbf{F}(t')dt'$ is the classical electron momentum due to the field, and e is the electron charge. This changes drastically the predictions of photoelectron distributions.

In the present work we aim to test the dressed and undressed versions of the molecular SFA experimentally. Analogously to the case of atomic ionization, molecular anions represent a well-suited system for this purpose. This is because the absence of the long-range Coulomb potential in negative ion detachment justifies applicability of the SFA approach. Below we present an angle-resolved photoelectron spectrum of F_2^- exposed to a laser pulse of 130 fs duration and 1300 nm wavelength. The field strength used in our experiment is of the order of the characteristic field experienced by the valence electron in F_2^-.

An added complexity in the present study is that interaction with the

laser field can also initiate photodissociation of the molecular anion, generating F^- and F. Since a typical dissociation period ($\sim 10^{-14}$ s) is shorter than the pulse length used here, the dissociation products can subsequently interact with the pulse. Because subsequent photodetachment of F^- contributes to the photoelectron yield, in the present work we consider the dissociation channel as well. (Subsequent ionization of F can be disregarded since the ionization potential of the fluorine atom is considerably higher than its electron affinity). Our experiment cannot distinguish between electrons detached from F_2^- and F^-. Therefore, we have separately recorded a photoelectron spectrum of F^-, exposed to the same laser pulse as F_2^-.

5.1 Methods

Both F_2^- and F^- are extracted from a glow discharge source operated with a gas mixture of NF_3 (10%) and Kr (90%). Negative ions, accelerated to a kinetic energy of 3 keV, pass through a Wien filter that selects either the F_2^- or F^- component of the ion beam. A typical ion current transmitted into the interaction region is 15 nA of F_2^- or 150 nA of F^-. The mass-selected ion beam is intersected with the laser beam inside an electron imaging spectrometer (EIS) operated in the velocity mapping regime. Linearly polarized laser pulses of 1300 nm wavelength are generated in an optical parametric amplifier (OPA) pumped with a mode-locked Ti:sapphire laser system at a repetition rate of 1 kHz. The output of the OPA is focused with a 15 cm focal length lens into the interaction region. A focus size of 46 μm (FWHM) and a pulse duration of 130 fs are measured with the standard beam diagnostic tools. Assuming a Gaussian shape of the spatiotemporal intensity distribution, the peak intensity in the focus is determined to be 3.4×10^{13} W/cm^2. The acquisition of F_2^- and F^- spectra is broken in alternating sequences in order to eliminate uncertainties caused by a long-term drift of the laser and ion beams. This ensures that both F_2^- and F^- negative ions are exposed to the same laser pulse. The images recorded with the EIS are processed using a conventional Abel inversion routine, which reconstructs the angle resolved momentum distribution of photoelectrons emitted from the interaction region. Further details on the experimental setup and the image processing can be found elsewhere [71].

The angle-resolved photoelectron spectra of F_2^- and F^- are presented in Fig. 5.1 in the $(p_\perp, p_\parallel)$ coordinates, where $p_\perp$ and $p_\parallel$ are the momentum components perpendicular and parallel to the laser polarization

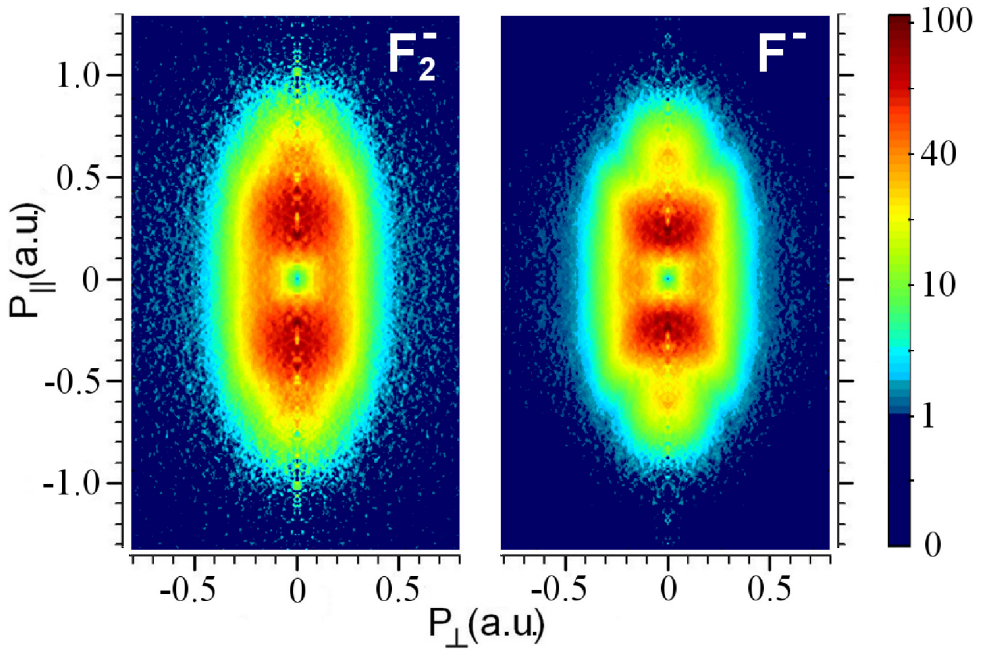

Figure 5.1: (color online). Momentum distribution of photoelectrons detached from F_2^- (left) and F^- (right) in a laser field of 1300 nm wavelength and 3.4×10^{13} W/cm^2 peak intensity. $p_\perp$ and $p_\parallel$ represent the momentum components perpendicular and parallel to the laser polarization axis, respectively.

axis, respectively. The distributions shown in Fig. 5.1 differ significantly. In particular, the F_2^- spectrum is broader along the polarization axis and it does not exhibit the nonmonotonic structure at higher momenta $p_\parallel$, which is well pronounced in the F^- spectrum. This structure, appearing as two islands on the $p_\parallel$ axis at $p_\parallel = \pm 0.6$ a.u., is due to the effect of quantum interference, which is discussed in detail in [71]. The considerable difference of the F_2^- and F^- spectra indicates that F_2^- does not dissociate at low intensities on the leading edge of the laser pulse and, thus, is exposed to a strong field.

5.2 Theory

Let us now describe photodetachment of F_2^- using the molecular SFA. The differential detachment rate in the laser field $\mathbf{F}(t) = \mathbf{F}\cos\omega t$ is given by the sum over n-photon channels [69] (atomic units are used

throughout)

$$dw = 2\pi \sum_{n \geq n_0} |A_{\mathbf{p}n}|^2 \delta(\frac{p^2}{2} + U_\mathrm{p} + E_0 - n\omega) \frac{d^3p}{(2\pi)^3} \ , \tag{5.1}$$

where $A_{\mathbf{p}n}$ is the n-photon transition amplitude to the final continuum state characterized by the electron momentum vector $\mathbf{p}$, n_0 is the minimum number of photons needed to overcome the ponderomotively shifted threshold, E_0 is the threshold energy, $U_\mathrm{p} = F^2/(4\omega^2)$ is the electron ponderomotive energy in a linearly polarized laser field, ω and F are the laser frequency and the field strength, respectively. The δ-function accounts for the energy conservation rule. For a given final vibrational state ν_f of the residual F_2 molecule, the threshold energy is $E_0 = E_{\nu_f} - E_{\nu_i}$, where ν_i and ν_f denote the vibrational quantum numbers of the initial state of F_2^- and the final state of F_2, respectively, and E_{ν_i} and E_{ν_f} are the energies of these states. This is illustrated in Fig. 5.2, which shows the potential curves of the ground electronic states $^2\Sigma_u^+$ and $^1\Sigma_g^+$ of the anion and its parent molecule, respectively. The potential curves are obtained from Ref. [174]. The fundamental vibrational frequency of F_2^- in its ground electronic state is 450 cm^{-1} [174]. One can easily estimate that only a few low vibrational states can be populated according to the Boltzmann distribution at a typical gas temperature of glow discharge. As an approximation, we therefore consider that all negative ions are produced in the lowest vibrational state $\nu_i = 0$.

Following results of Ref. [173], the transition amplitude for an initial state of ungerade symmetry has the form

$$\begin{aligned} A_{\mathbf{p}n} = -\frac{\omega}{2\pi} S_{\nu_f\nu_i} \sum_{s=\pm 1} s \int_0^T e^{\frac{i}{2}s(\mathbf{p}+\eta\mathbf{k}_t)\cdot\mathbf{R}_0} \tilde{\psi}(\mathbf{p}+\mathbf{k}_t) \\ \times \left(E_0 + \frac{(\mathbf{p}+\mathbf{k}_t)^2}{2} \right) e^{\frac{i}{2}\int^t (\mathbf{p}+\mathbf{k}_t)^2 d\tau + iE_0 t} dt \quad , \end{aligned} \tag{5.2}$$

where the sum accounts for contributions from the two centers of the diatomic anion, $\mathbf{R}_0$ defines the molecular axis and the equilibrium distance between nuclei in F_2^-, $S_{\nu_f\nu_i}$ is the overlap of nuclear wave functions of F_2^- and F_2, $T = 2\pi/\omega$, and $\tilde{\psi}(\mathbf{q})$ is the Fourier transform of the atomic orbital $\psi(\mathbf{r})$ which composes the highest occupied molecular orbital (HOMO) of σ_u-symmetry in F_2^-. The index η in Eq. (5.2) defines whether the initial state is considered to be dressed ($\eta = 0$) or undressed ($\eta = 1$).

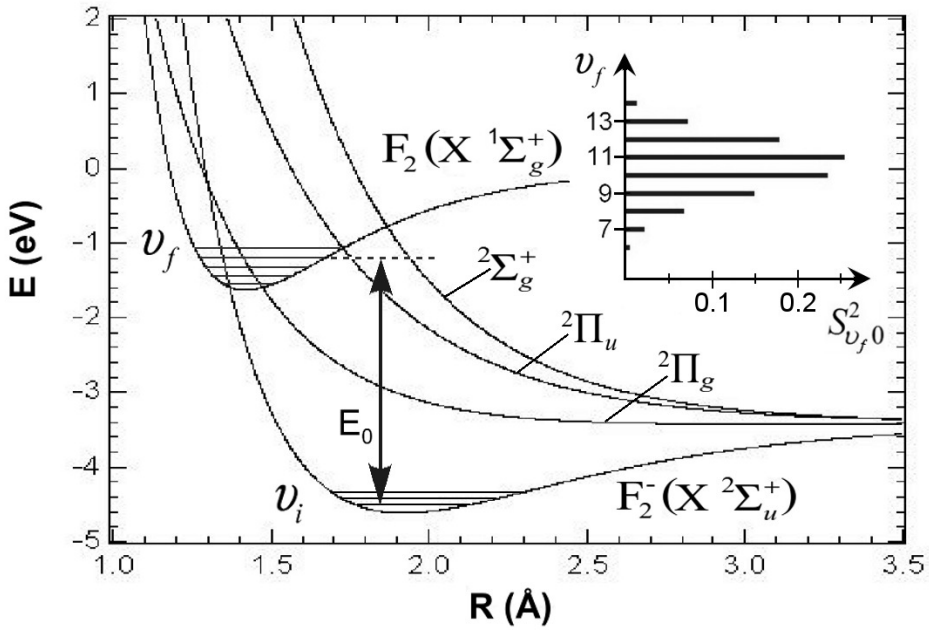

Figure 5.2: Potential energy curves of electronic states of F_2^- and the ground electronic state of F_2. ν_i and ν_f are the vibrational quantum numbers of F_2^- and F_2 vibrational states, respectively, E_0 denotes the threshold energy for a given $\nu_i \rightarrow \nu_f$ transition. The insert shows the squared overlap of nuclear wave functions, $S^2_{\nu_f \nu_i}$, for $\nu_i = 0$ and different ν_f values.

The values of $S^2_{\nu_f\nu_i}$ for $\nu_i = 0$ and different ν_f are presented in the insert of Fig. 5.2. It shows that the overlap of nuclear wave functions has a peak at $\nu_f = 11$. The large value of ν_f is due to the rather large difference in equilibrium positions of nuclei in F_2^- and F_2, as one can see from the potential energy curves in Fig. 5.2. The distribution of $S^2_{\nu_f\nu_i}$ over ν_f is rather narrow, and the energy interval between vibrational levels of F_2 in the vicinity of $\nu_f = 11$ is small (≈ 540 cm^{-1}) in comparison with the photon energy. Thus, the population spread over different final vibrational states can be disregarded, and we consider the formation of F_2 only in the $\nu_f = 11$ state and assign 1 to $S_{\nu_f\nu_i}$ in Eq. (5.2). The threshold energy E_0, explicitly defined by the difference $E_{\nu_f=11} - E_{\nu_i=0}$, is 3.965 eV. Five photons are required to overcome this threshold.

We evaluate Eq. (5.2) analytically by using the method of steepest descent in the same way as described in [69]. In order to simplify this task, the two-center zero-range potential model [103] is used for the description of the electronic state. In this model, the HOMO wave function of F_2^- can be represented analytically as $\Psi(\mathbf{r}) = \psi(\mathbf{r} + \mathbf{R}_0/2) - \psi(\mathbf{r} - \mathbf{R}_0/2)$, where

$$\psi(\mathbf{r}) = C\frac{e^{-\kappa r}}{r}Y_{10}(\theta_m, \phi_m) \,, \tag{5.3}$$

$C = 0.701$ is the normalization coefficient, Y_{10} is the spherical harmonic, the spherical angles (θ_m, ϕ_m) are defined with respect to the molecular axis, and $\kappa^2/2$ is the vertical electron affinity defined as the energy difference between the potential curves in Fig. 5.2 at the equilibrium distance $R_0 = 1.937$ Å. In the spherical coordinates (θ, ϕ) with respect to the laser polarization axis, the angular part of the atomic orbital in Eq. (5.3) can be represented as

$$\begin{aligned} Y_{10}(\theta_m, \phi_m) &= \cos(\alpha)Y_{10}(\theta, \phi) \\ &+ \sin(\alpha)\frac{1}{\sqrt{2}}(Y_{1-1}(\theta, \phi) - Y_{11}(\theta, \phi)) \,, \end{aligned} \tag{5.4}$$

where α is the angle between the molecular axis and the polarization axis. Since the molecular anions are randomly oriented in the laser focus, the photodetachment rate is averaged over α and ϕ.

5.3 Discussion and Conclusion

The simulation routine of photoelectron spectra is described elsewhere [71]. It involves integration of the electron yield over the spatiotempo-

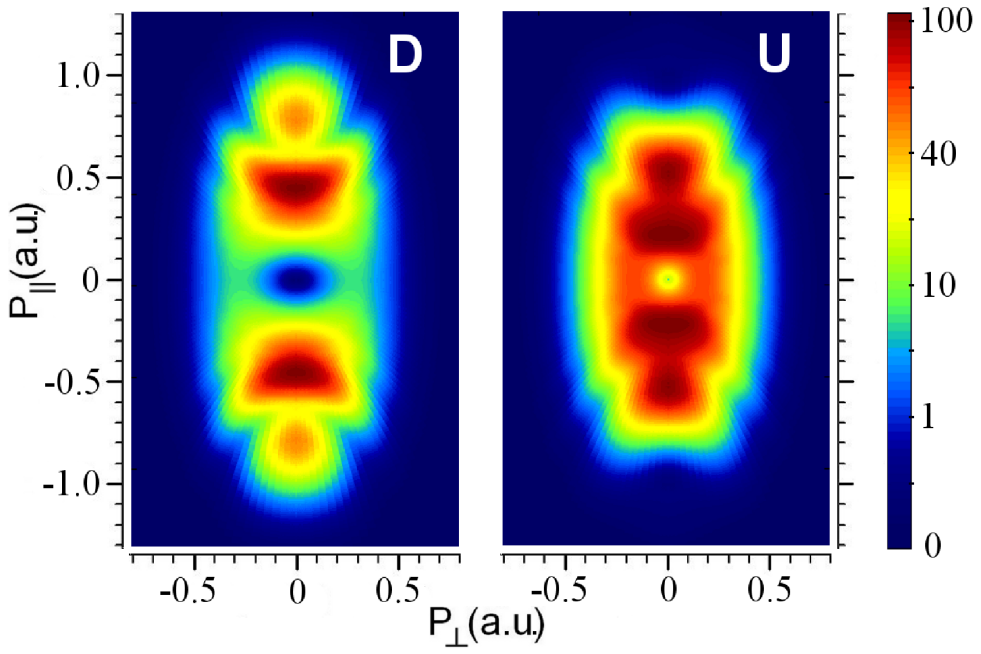

Figure 5.3: (color online). Photoelectron distributions of F_2^- predicted by the dressed (left) and undressed (right) versions of the molecular SFA.

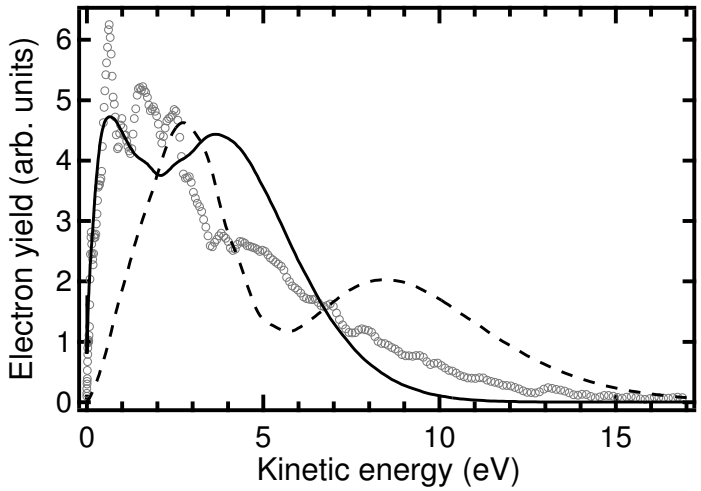

Figure 5.4: Energy distribution of photoelectrons emitted from F_2^- along the laser polarization axis. Circles represent experiment, solid and dashed lines show predictions by the undressed and dressed versions of the molecular SFA, respectively. The curves are normalized according to the integrated yield.

ral intensity distribution in the laser focus and accounting for depletion of negative ions during their interaction with the field. Results of simulations are presented in Fig. 5.3. Comparison of the predicted distributions with the measured spectrum of F_2^- (see Fig. 5.1) shows that neither the dressed nor undressed version of the molecular SFA agree with experiment. Both simulated spectra exhibit a nonmonotonic structure, caused by the effect of quantum interference, which consists of two maxima lying on the laser polarization axis. As expected, this structure is very different in the dressed and undressed versions of the molecular SFA. On closer inspection of the predicted spectra, one can see that the position of the broad maximum in the experimental spectrum is not reproduced in either simulation. This is quantitatively illustrated in Fig. 5.4, which compares the measured and predicted distributions of photoelectrons emitted along the laser polarization axis. We would like to point out that the low-energy contribution to the spectrum is suppressed in the dressed version of the molecular SFA (see Fig. 5.3 and Fig. 5.4). This result is explained in [173] as being due to the effect of two-center interference.

As an alternative description of the F_2^- spectrum, let us consider that dissociation of F_2^- occurs at high laser intensities and is followed by photodetachment of the created F^-. Thus, the atomic anions appear in the laser focus at a time t_0, which is close to the center of the temporal pulse envelope, and their detachment during the rest of the pulse ($t > t_0$) constitutes the electron yield. Photoelectron spectra of F^- are calculated by using our simulation routine [71] for different initial times $t_0 = -\sigma_t, -\sigma_t/2$, and 0. Here $\sigma_t = 79$ fs is the measured Gaussian width of the temporal intensity profile $I(t) = I\exp(-t^2/\sigma_t^2)$, and the peak of the pulse is at $t = 0$. The calculated energy distributions of electrons detached along the laser polarization axis are compared with the measured spectrum of F_2^- in Fig. 5.5. One can see that the distribution width is larger when t_0 is closer to the center of the pulse. This is because the negative ions are less depleted before they experience higher intensities generating photoelectrons of higher kinetic energies. The broadest electron distribution is obtained for $t_0 = 0$, since in this case the created F^- ions are immediately exposed to the peak intensity. However, even for $t_0 = 0$ the simulated spectrum is still narrower than the measured distribution at low energies ($\lesssim 3.5$ eV), while the simulation overestimates the higher-energy part of the spectrum. Each predicted distribution shown in Fig. 5.5 possesses a well-pronounced nonmonotonic structure caused by the quantum interference effect [71]. This structure, however, is not resolved in the experimental spectrum.

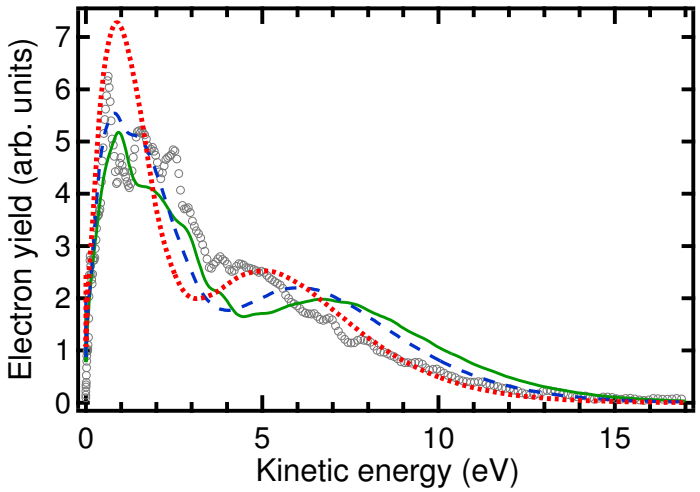

Figure 5.5: (color online). Comparison of the experimental energy distribution shown in Fig. 5.4 (circles) with predictions by the model that assumes strong-field dissociation of F_2^- followed by photodetachment of F^-. Calculations are performed for different initial times (see text): $-\sigma_t$ (dotted line), $-\sigma_t/2$ (dashed line), and 0 (solid line). The curves are normalized according to the integrated yield.

Considering that F^- ions are created by dissociation over a range of values of t_0, the predicted distribution should be averaged over t_0. Fig. 5.5 reveals that, depending on t_0, the simulation can either reproduce the high-energy tail of the experimental spectrum or better reproduce its low-energy part. Therefore, a superposition of curves calculated for various t_0 can not describe the experimental distribution in the entire energy range and the contribution from strong-field detachment of F_2^- needs to be reconsidered as well.

Summarizing, photodetachment of F_2^- in a strong laser field reveals complicated dynamics, involving both direct strong-field detachment of the molecular anion and detachment of F^- created in the laser focus by strong-field dissociation. A coincidence technique (e.g. similar to the one developed in [104]), allowing to distinguish between electrons produced in these processes, is required for the experimental test of the molecular SFA. We believe that our results will initiate development of more comprehensive methods, accounting for the complexity of molecular orbitals, where detachment and dissociation are considered as competing processes and the population dynamics of the molecular and atomic anions in the laser focus is taken into account.

The authors greatly appreciate fruitful discussions with Professor Hanspeter Helm. This work is supported by the Deutsche Forschungsgemeinschaft, Grant No. KI 865/3-1.

CHAPTER 6

Visualization of electronic motion in an atomic ground state

Hannes Hultgren*, Mikael Eklund*, Dag Hanstorp† and Igor Yu. Kiyan*◇

*Physikalisches Institut, Albert-Ludwigs-Universität, D-79104 Freiburg, Germany.
†Department of Physics, University of Gothenburg, 412 96 Gothenburg, Sweden.
◇Current address: Helmholtz-Zentrum Berlin für Materialien und Energie, Albert-Einstein-Strasse 15, 12489 Berlin, Germany.

in manuscript

Electron dynamics in atoms and molecules is a topic of fundamental interest. The ultimate goal is to monitor and control chemical reactions on an atomic level. We present the first direct observations of electron dynamics in the ground state of an atom. Using a femtosecond pump-probe laser scheme and velocity map imaging we project the electronic wave function on a macroscopic detector. Starting with a carbon anion and exposing it to a strong laser field, a wave packet is created in the ground state of the atom by strong-field detachment. Subsequently, the electronic wave packet in the atom is probed by means of strong-field ionization. We observe a strong temporal modulation in the yield of ionized electrons, revealing a direct visualization of a periodic spatial rearrangement of the electron cloud in the atom.

Classical mechanics provides a deterministic view of the world. The path of a particle can be calculated if we know its position, velocity and the forces acting upon it at any given position and time. The precision of our measuring device is the limiting factor for the accuracy of our knowledge of a particle's state, and the world in general.

This is not the case in the world of quantum mechanics. A particle is then described as a wave, as suggested by De Broglie in 1924 [5]. The wavelength λ of the particle is given by $\lambda = h/p$ where p is the linear momentum of the particle and h is the Planck constant. The position and momentum of a particle cannot be determined exactly. The wave dynamics is mathematically described by the Schrödinger equation, $i\hbar\frac{\partial}{\partial t}\Psi(\vec{r},t) = \hat{H}\Psi(\vec{r},t)$, where the solutions provide the probability density distributions for the particle in time and space. In this equation, Ψ is the wave function giving the probability density and H is the Hamiltonian operator associated with the total energy of the system. The quantum mechanical wave function displays all the characteristics of waves such as interference and diffraction. The wave nature of particles is normally only observable on a microscopic level. However, wave phenomena have been seen in a number of experiments, including electron and neutron diffraction [6,9] .

In a quantum-mechanical description, the probability distribution of a free particle can be localized in space by forming a superposition of complex-valued plane-wave functions $e^{i(\mathbf{k}\cdot\mathbf{r}-\omega t)}$ with different wave vectors $\mathbf{k}$ and frequencies ω, corresponding to different momenta. The waves interfere constructively in a limited region of space and destructively elsewhere. Thus, a so called wave packet is created representing a quantum analog of a classical particle. Considering an atom in an eigenstate, the electronic wave function represents a standing wave, with a spatial probability distribution being constant over time. It is, however, possible to create an electron wave packet within an atom. This occurs when multiple bound atomic states are coherently populated, forming an evolving system where the electron spatial distribution varies with time. The first demonstration of wave-packet dynamics in atoms was performed by Yeazell et al [106] in an experiment involving excitation of Rydberg states. In this case, temporal variations in the spatial electron distribution was probed by measuring the time variation of the ionization probability of the excited system. The time constant Δt of the spatial evolution is determined by the Heisenberg uncertainty principle [11], $\Delta E \cdot \Delta t \geq h$, where ΔE is the energy separation of the coherently excited states. Several other observations of the electronic motion have been made in excited atoms [107, 108], in highly excited Rydberg atoms [109, 110] and in positively charged ions [105, 111].

6.1 Methods

In the present work we describe a novel method to visualize the electronic motion in the ground state of an atom. A strong-field pump-probe laser scheme has been used to directly project the spatial part of the electronic distribution along the laser polarization direction onto a detector. We have applied this method to the ground state of the carbon atom and present the very first observations of a coherently created electronic wave packet moving in the ground state of an atom. Our basic idea is to initiate the experiment with a negative ion and detach one electron by applying a strong linearly polarized laser field of short pulse duration. Electron emission in a strong field is highly dependent on the orientation of the electron orbital, i.e. on the magnetic quantum number m_l of the initial state. The angular-momentum quantization axis is here provided by the laser polarization. Orbitals with $m_l = 0$ display emission rates orders of magnitude larger than orbitals with $m_\ell \neq 0$ [74, 112]. Hence, the residual carbon atom is created with a localized hole in the electron density distribution along the laser polarization direction. This constitutes the orbital alignment effect discussed in Refs [113–116, 118]. From the theoretical point of view, the spatially confined hole is created due to a superposition of the three spin-orbit components of the ground state of carbon. In order to populate these components coherently, the detachment process is required to be faster than the spin-orbit period of the ground state. In our experiment we probe the dynamics of the coherently created wave packet by ionizing the atom with a second strong laser pulse, applied at variable time delays. As describe above, the strong field mostly ionizes electrons with the density distribution localized along the laser polarization axis. By projecting the photoelectrons onto a position sensitive detector, it is therefore possible to directly visualize the electron density distribution in the residual atom. This method represents the most straightforward way to study the electron dynamics in atomic systems available today.

The experiment was performed using an electron imaging spectrometer (EIS) and a laser system that generated a pair of short laser pulses of 100 femtosecond duration in the infrared wavelength region. The optical setup is schematically shown in Fig. 6.1. Negative ions were created in a commercially available sputter ion source. The ions were accelerated and subsequently mass selected in a Wien filter before being intersected with the two laser beams inside the EIS. The experimental setup and procedure is described in more detail in the supple-

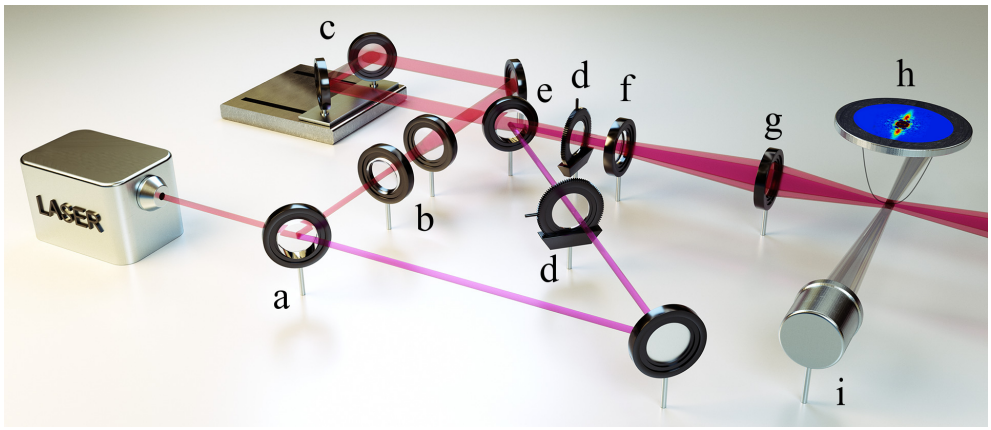

Figure 6.1: Schematic view of the experimental setup. An optical parametric amplifier (LASER) generates the linearly polarized pump (red) and probe (purple) pulses. The two laser beams are split in a dichroic mirror (a), and the pump beam divergence is controlled by a telescope (b). The time delay between the pump and probe pulses is controlled by a motorized micrometer translation stage (c). The polarizations of both beams can be rotated individually with two $\lambda/2$-plates, (d). The two laser beams are merged in a dichroic mirror (e). Both beams are expanded, (f), before focused into the interaction region with a 150mm focal length lens, (g), and intersected with the ion beam (grey). Detached electrons are projected onto the position sensitive detector inside the EIS, (h). The ion current is measured using a Faraday-cup (i).

mentary material.

The photo-processes induced in this experiment can be expressed as

$$C^- + n_1 h\nu_1 \rightarrow C + e^-$$

followed by

$$C + n_2 h\nu_2 \rightarrow C^+ + e^-$$

where n_1 and n_2 denote the number of photons absorbed in the pump and probe transitions, respectively, and $h\nu_1$ and $h\nu_2$ represent the corresponding photon energies. Electrons emitted in both steps were detected using the EIS.

The ground quartet state of C^- possesses three p-electrons having the same spin projection but different magnetic quantum numbers, $m_\ell = -1, 0, +1$. Since the strong field detaches primarily the $m_\ell = 0$ electron, this orbital becomes depleted immediately after the detachment step, and the atom acquires a high degree of orbital alignment. The wave packet of spin-orbit states in the residual atom, associated with the localized hole in the $m_\ell = 0$ orbital, is populated coherently. After a variable time delay the residual carbon atoms were ionized by the linearly polarized probe pulse hν_2. The yield was observed to be dependent of the hole-density state, controlled by the pump-probe delay. Following the pump pulse, the hole created in the ground state of the carbon atom starts its evolution. Its density distribution interchanges between being oriented along and perpendicular to the quantization axis defined by the pump pulse polarization. The probe pulse monitors the electron density distribution along its own polarization axis. The entire data acquisition procedure is described in the supplementary material.

6.2 Results

All data shown below were recorded with a time delay between the pump and probe pulses, Δt_p, larger than 600 fs. The two laser pulses were thus completely separated in time and effects associated with interference between the two laser beams were completely avoided. Fig. 6.2 shows three images recorded at Δt_p = 2000 fs, 2300 fs and 2600

fs. The images represent the angle resolved momentum distribution of the detected electrons. The electron's momentum is represented by the distance from center of the image, and the arrow in Fig. 6.2d displays the direction of the probe laser polarization. A momentum of 1.5 a.u. corresponds to the absorption of 45 photons. The main differences in the figures are the number of high- energy electrons emitted along the laser polarization, seen as vertically oriented jets.

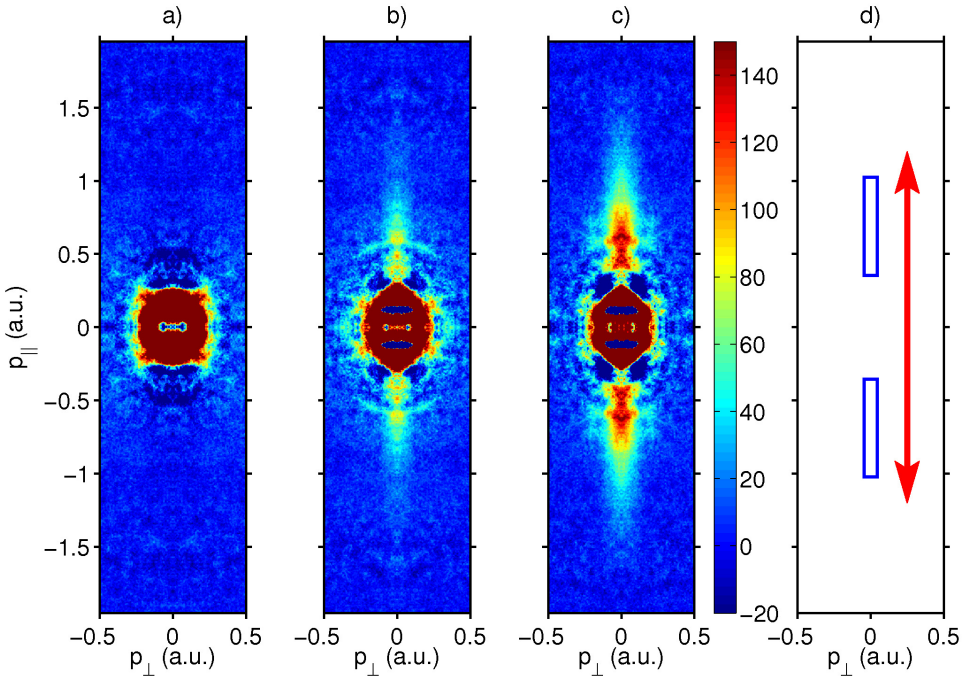

Figure 6.2: (color online) Images recorded at time delays between pump and probe pulses of 2000 fs (a), 2300 fs (b) and 2600 fs (c). $p_{\|}$ and $p_{\perp}$ represent the momentum of the electrons emitted parallel and perpendicular with respect to the laser polarization of the probe beam, shown as the arrow in (d). A strong modulation in the amount of high-energy electrons, caused by a coherently created wave packet in the ground state of the carbon atom, is observed. The two rectangles shown in d) represent the area over which the electron yield was integrated in the data shown in Fig. 6.3.

The experimental results presented in Fig. 6.2 can be directly understood from the time evolution of the created electronic wave packet. As discussed above, the photodatechment step creates a hole in the electron density distribution along the polarization axis. This hole has the form of a p-orbital aligned along the polarization axis, i.e. the spherical harmonic Y_{10}. Thereafter, the created atoms are exposed to a second laser pulse, which has an intensity sufficiently high to induce strong field ionization. However, there are no high-energy electrons

produced since a hole was previously created in the population density along the polarization axis. Hence, no jet of high-energy electrons is visible in Fig. 6.2a. In Fig. 6.2c, on the other hand, the hole in the electron density has moved to be localized around the horizontal plane, i.e. at 90° with respect to the pump polarization. This can be visualized as the Y_{11} spherical harmonic. At this stage there is a high electron density along the laser polarization axis, yielding a strong signal of high-energy electrons. A large modulation in the amount of ionized electrons are therefore seen in the three figures, manifested as a change in the intensity of the electron jet along the laser polarization. Hence, the three images displayed in Fig. 6.2 clearly reveal a time evolution of a coherently created wave packet moving in the valence shell of the atom. The interpretation is supported by Strong Field Approximation (SFA) simulations. The two extreme situations (a) and (c) in Fig. 6.2 are reproduced by SFA simulations described in the supplementary material.

The shortest spin-orbit period derived from the energy splitting of the $J = 0$ and $J = 2$ components of the ground state is 768 fs. This period is one order of magnitude larger than the rise time of the leading front of the pump pulse where the photodetachment process generates most of the atoms. According to our SFA simulations, this time interval extends over approximately 50 fs. While the intensity of the pump pulse is sufficiently high to deeply saturate the photodetachment process, our simulations show that its contribution to ionization of the residual atoms is negligible. This is due to the low pump photon energy of 0.60 eV, which requires 18 photons to overcome the ionization threshold of carbon.

The large signal of low energy electrons in the center of figures 6.2(a), (b) and (c) are primarily due to negative ions that survived the pump pulse and are photodetached by the probe beam. We put our focus on the high-energy electrons in the jets where the strong-field effects are the largest. Fig. 6.3 displays the time evolution of the amount of high-energy electrons, evaluated by integrating the signal within the area of the two rectangles shown in Fig. 6.2d.

The time evolution can be described as a quantum beat between the three fine structure components of the ground state of the carbon atom. The time period τ of the beat of two coherent states is given by $\tau = h/\Delta E$, where h is Planck constant and ΔE is the energy spacing between the states involved. In our case, there are three coherently populated fine structure components, which give rise to three beat periods

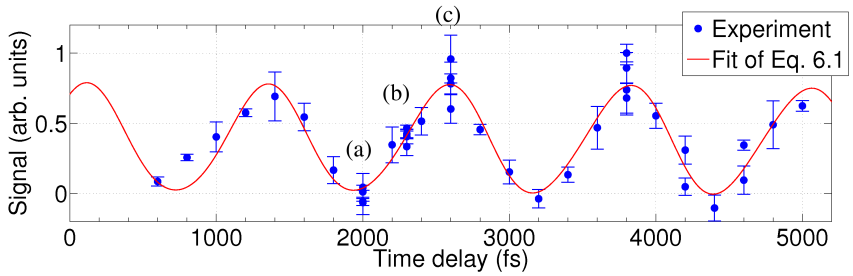

Figure 6.3: The yield of high-energy electrons emitted in the ionization step plotted as a function of the time delay between the pump and probe pulses. The solid line represents the fit result of Eq. 6.1 to the data set. Images shown in Fig. 6.2 are associated to the data points denoted by (a), (b) and (c).

represented by τ_1 (J=2,1), τ_2 (J=2,0) and τ_3 (J=1,0). A function containing the sum of three cosine functions is therefore fitted to the data set.

$$f(t) = \alpha + \sum_{i=1}^{3} \beta_i \cos\left(\frac{2\pi}{\tau_i}(t - t_0)\right), \tag{6.1}$$

where α represents a constant background and β_i are the amplitudes of the individual cosine functions. The uncertainty in the determination of $t = 0$, where the two laser pulses are perfectly overlapped in time, is represented by t_0 in the fit procedure.

The result of the fit is shown in table 6.1 together with the oscillation periods calculated using the tabulated values of the fine structure splitting ΔE_{FS} [85]. The experiment covers more than three spin-orbit periods. The fine structure levels of the ^3P state are expected to be populated in accordance to their degree of degeneracy. Thus the $J = 2$ level is fivefold degenerate, the $J = 1$ level is three-fold degenerate and the $J = 0$ level is non degenerate. Therefore, the main oscillation seen in Fig. 6.3 is due to the beat between the $J = 2$ and $J = 2$ levels. There is a good agreement between experimentally determined oscillation periods obtained from the fit and the values extracted from the tabulated fine structure splittings. In particular, the strong beat between J = 1 and J = 2 levels is measured to be 1229±16.5 fs is in excellent agreement with the value of 1235 fs calculated from $\tau = h/\Delta E_{FS}$.

We interpret the modulation of the amount of ionized electrons in the probe step as a manifestation of a spatial change of electron density in the carbon atom. For the very first time the electron dynamics in the ground state of an atom is directly visualized. The pump pulse creates

Beat	ΔE_{FS} (meV)	τ_{cal} (fs)	τ_{exp} (fs)	Rel. Ampl.
J_{01}	2.03	2034	1931±1456	0.01±0.075
J_{02}	5.38	769	637±23	0.081±0.070
J_{12}	3.35	1235	1229±16.5	1±0.056

Table 6.1: Fine structure splittings (ΔE_{FS}), calculated beat periods (τ_{cal}), measured beat periods (τ_{exp}) and relative amplitude of the quantum beats.

a wave packet in the carbon atom. The motion of the wave packet produces an oscillation in the electron probability density along the laser polarization direction. The method used to detect the probability density as a function of time shows a direct visualization of the oscillating wave packet. We see a near complete modulation of the ionization signal over a full oscillation period. No sign of decoherence is visible within four full oscillations. Further investigations on the time scale of decoherence are in progress. Strong field simulations support the view of a spatially moving wave packet in the valence shell of the carbon atom. The current results focus on the carbon atom, which is of wide interest in several fields, not only in physics but also in quantum chemistry and biochemistry. The method is general and can be applied to a wide field of quantum systems such as other atomic elements or more complex quantum mechanical systems. Future investigations will be performed to probe motions of electronic wave packets in diatomic molecules.

Acknowledgments: This work was funded by the Deutsche Forschungsgemeinschaft (DFG), Grant No. KI 865/3-1. DH acknowledges support by the Swedish Research council, ME acknowledges support by the ICONIC network.

6.3 Supplementary Material:

6.3.1 Experimental Setup

In short, the linearly polarized idler (2055 nm) and signal (1310nm) outputs from an optical parametric amplifier (OPA) pumped with a mode-locked Ti:sapphire laser system at a repetition rate of 1kHz were used as the pump and probe beams, respectively. The laser beams were split using a dichroic mirror. The polarization axes of both laser

beams were controlled by means of two $\lambda/2$ plates. The time delay between the pump and the probe pulses was varied by changing the optical path length for the pump beam with the use of an optical delay stage. A 150 mm focal length lens placed in front of the experimental chamber focused both laser beams into the interaction region. The focal positions along the beam propagation direction were made to coincide by adjusting the divergence of the pump beam with the use of a telescope. A negative lens expanded both beams before being focused into the interaction region. This decreased their diffraction limited focal sizes in the interaction region, hence increasing intensity. Focal sizes of 18μm (FWHM) and 10 μm. (FWHM) for pump and probe pulses, respectively, were measured using standard beam diagnostic tools. The pulse duration of the two beams were 100 fs (FWHM). The pulse energies of the pump and probe beams were 150 and 240 μJ, yielding the peak intensities of 8×10^{13} and 4×10^{14} W/cm^2, respectively. The two laser beams were merged using a dichroic mirror.

A beam of negative carbon ions was produced in a sputter ion source. The ion beam was accelerated to a kinetic energy of 4.5 keV, mass selected in a Wien filter and intersected with the two laser beams inside an Electron Imaging Spectrometer (EIS) [75, 76] operating in the velocity mapping regime [71]. The spectrometer allows the recording of angle resolved momentum distributions of photoelectrons. An ion current of 300 nA was measured after the spectrometer. The ion beam was focused using an Einzel lens to a beam waist of 1 mm. The linearly polarized pump pulse, $h\nu_1$, induced photodetachment of the $^4S_{3/2}$ ground state of C^-, leaving the residual carbon atom in the triplet ^3P ground state (see Fig. 6.4). It represents the only detachment channel for the C^- ground state since spin conservation does not allow transition to the ^1D and ^1S states, having the same $2p^2$ configuration. There is also a ^2D excited state in C^-. However, it has been shown that the amount of excited carbon anions generated in a sputter source is typically several orders of magnitude smaller than the amount of anions produced in the ground state [117]. Therefore, we can neglect the contribution of the ^2D state in our consideration and we conclude that photodetachment of C^- produces a pure ground-state population. Due to the larger focus size of the pump beam and the saturation condition in the photodetachment step, the region where carbon atoms are produced in the aligned ^3P state is considerably larger than the focal volume of the probe pulse. Substantial efforts were made to ensure that the probe beam overlaps with the ion beam in the center of the pump beam, where all negative ions are photodetached. The target ions move over a negligible fraction of the focal size during the time

span between the pump and probe pulses. Hence, the probe beam interacts solely with neutral carbon atoms created in the aligned state. The probe pulse has a higher photon energy than the pump pulse, requiring absorption of 11 instead of 18 photons to overcome the ionization threshold. The probe pulse was able to ionize the atoms due to the lower number of photons required, in combination with a higher intensity. A higher contrast is obtained by displaying the difference in the ionization yield recorded for different polarization directions of the probe beam with respect to the pump polarization. Therefore, for a given pump-probe time delay we recorded images with the pump and probe polarizations being parallel and perpendicular to each other and subtracted them. The probe polarization was always kept parallel to the detector plane of the EIS. The EIS does not reveal if the detected electrons have been generated by the pump pulse or the probe pulse. In order to isolate the ionization yield, photoelectron spectra generated by the pump pulse alone were therefore subtracted from the images as a background. The complete acquisition procedure is graphically depicted in Fig. 6.5.

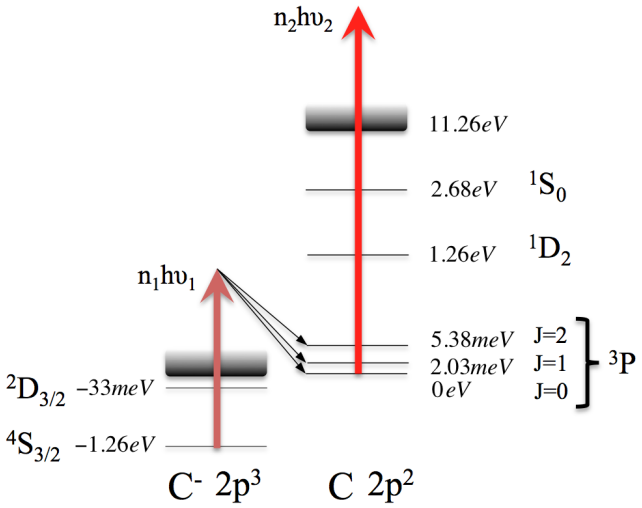

Figure 6.4: Energy level diagram (not to scale) of the negative carbon ion and selected low-lying states of the carbon atom [85]. The arrows schematically depict the phototransitions induced by the pump and probe pulse.

6.3.2 The Strong Field Approximation

Our experimental observation can readily be modeled using the Strong Field Approximation (SFA) introduced by Keldysh [65]. The approxi-

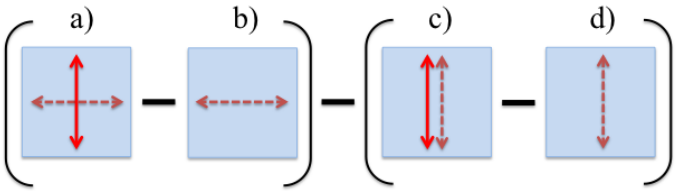

Figure 6.5: Acquisition procedure: Ionization yield with the parallel arrangement of the pump and probe polarizations (right parentheses) is subtracted from the yield with their perpendicular arrangement (left parentheses). Dashed and solid arrows represent the polarization direction of the pump and probe pulses, respectively.

mation consists in neglecting the core potential in the final continuum state. Thus, the final state is represented by the Volkov wave function [66], which describes a free electron quivering in an external laser field. We have simulated photodetachment followed by photoionization using the SFA approach developed by Gribakin and Kuchiev [69]. This approach has been proved to describe strong-field detachment very well [71] as well as sequential double detachment [72]. A detailed description of the theory is available in and its application to the case of negative ions together with the simulation routine are presented in a thorough manner in [71]. We use this routine to calculate strong-field ionization yields separately for the $m_\ell = 0$ and $m_\ell \neq 0$ states in the carbon atom. The simulation procedure includes integration of the electron yield over the spatiotemporal intensity distribution in the laser focus. Fig. 6.6 displays angle-resolved photoelectron spectra of strong-field ionization of carbon, obtained with the laser parameters used in the present experiment. In Fig. 6.6a, the result of strong-field ionization of the atom in the $m_\ell = 0$ state reveals a greatly enhanced ionization yield. Fig. 6.6b shows the result of simulations where the initial state has $m_\ell \neq 0$, i.e. the p orbital is aligned perpendicular to the linearly polarized probe laser field. The direction of the polarization of the probe beam is vertical in the figure. The simulations are in good agreement with the two extreme situations in the experiment, where the electron density distribution along the probe polarization axis has a minimum (Fig. 6.2a) and where it has a maximum (6.2c).

The authors gratefully acknowledge support from the Deutsche Forschungsgemeinschaft (DFG), Grant No. KI 865/3-1 and Swedish Research Council.

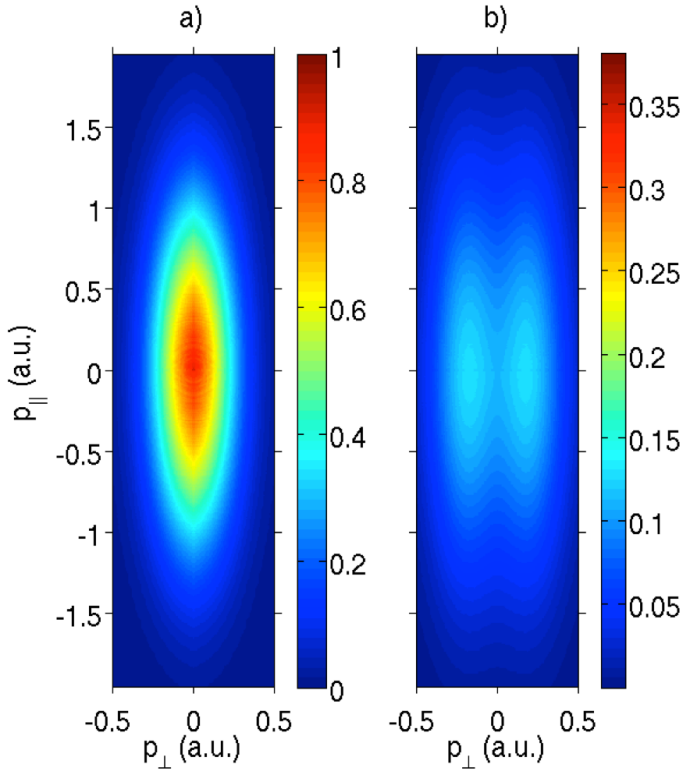

Figure 6.6: Simulated ionization spectra of carbon assuming that either a pure $m_\ell = 0$ (a) or a pure $m_\ell \neq 0$ (b) orbital is ionized. Note the difference in the color scales of the two figures.

CHAPTER 7

Visualization of electronic motion in the ground state of carbon and silicon atoms

Hannes Hultgren*, Mikael Eklund*, Dag Hanstorp†, A. O. Lindahl† and Igor Yu. Kiyan*◇

*Physikalisches Institut, Albert-Ludwigs-Universität, D-79104 Freiburg, Germany.
†Department of Physics, University of Gothenburg, 412 96 Gothenburg, Sweden.
◇Current address: Helmholtz-Zentrum Berlin für Materialien und Energie, Albert-Einstein-Strasse 15, 12489 Berlin, Germany.

in manuscript.

The advance of femto- and attosecond lasers has opened up for time resolved studies of electronic dynamics in atoms and molecules. The ultimate goal is to monitor and control chemical reactions on an atomic level. We present a novel method providing a direct visualization of electronic motion in the ground state of atoms. A femtosecond pump-probe laser scheme combined with velocity map imaging were used to project the electron density distribution onto a macroscopic detector. The pump laser pulse creates a coherent electronic wave packet in the ground state of the atom through multiphoton detachment of its parent negative ion. This wave packet is subsequently probed by strong field ionization. The energy and angular distribution of the emitted electrons are detected using a velocity map imaging spectrometer. We observe a strong temporal modulation in the yield of ionized electrons, due to a periodic spatial rearrangement of the electron cloud in the atom. The method has been applied to carbon and silicon atoms.

Electronic motion and correlations in the valence shell of an atom is a fundamental topic presently receiving a great deal of attention. The

advance of femto- and attosecond lasers has opened up a vast field of monitoring and controlling electron dynamics on ultrashort time scales. It is possible to create an electronic wave package within an atom, ion or molecule, forming a system where the spatial electron distribution evolves over time. This occurs when multiple states are coherently populated [118]. According to the Schrödinger equation the populated states have different phase velocities producing a quantum beat. The beat period is given by $\tau = \Delta E/h$, where ΔE is the fine structure splitting between two populated states, and h is the Planck constant. Yeazell *et al.* [106] created a wave packets and detect the resulting quantum beat in highly excited Rydberg atoms. Several other indirect observations of electron dynamics have been performed, e.g in excited atoms [107, 108], in highly excited Rydberg atoms [109, 110] in positively charged ions [105, 111].

In this work we describe a novel method to visualize electronic motion in the ground state of an atom. The current experiment was performed by combining a momentum and angular resolved Electron Imaging Spectrometer (EIS) [75, 76], operated in the velocity mapping regime [79], with a strong-field pump-probe laser scheme to directly project the spatial part of the electronic wave function along the laser polarization onto a detector. A key to the success of this experiment was to initiate the experiment with a negative ion. We have investigated the time evolution of a coherently created wave packet in carbon and silicon atoms. Both belong to the carbon group of the periodic table in which the negative ion have a p^3 ^3P configuration, i.e. with three electrons in half filled valence shell. Hence, the negative ion is spherically symmetric. The extra electron is removed through a strong-field photodetachment process. The probability of initiating a detachment process in a strong laser field is strongly dependent on the m_l quantum number of the individual electrons. Electron states with $m_l = 0$ display detachment rates orders of magnitude larger than substates having $m_l \neq 0$ [74, 112]. Hence, a short laser pulse will detach $m_l = 0$ substates first and a localized hole in the electron density distribution is created along the laser polarization. The residual atom has a reduced population in $m_l = 0$ while $m_l \neq 0$ substates are still populated. The atom is said to be in an aligned state [113–116, 118]. The spatially confined hole is created due to a superposition of the three spin-orbit components of the ground state of the atom. In order to populate these components coherently, the detachment process should be faster than the spin-orbit period of the ground state, this requires application of a femtosecond laser pulse. The localized hole in $m_l = 0$ is subsequently probed by strong-field ionization of the resid-

ual atom. The ionization yield is dependent on the spatial electron distribution in the atom which is changing due to the oscillating wave packet. The fine structure splitting in carbon and silicon atoms is of the order of a few meV, resulting in a wave packet evolving on a femtosecond time scale. The time evolution of the coherently created wave packet was observed by varying the time delay between the pump and probe pulses. The electron density along the direction of the probe pulse polarization was projected onto a detector and probed as a function of the pump-probe delay time. This method represents a more direct way to study the electron dynamics in atomic systems than the other approaches above.

7.1 Methods

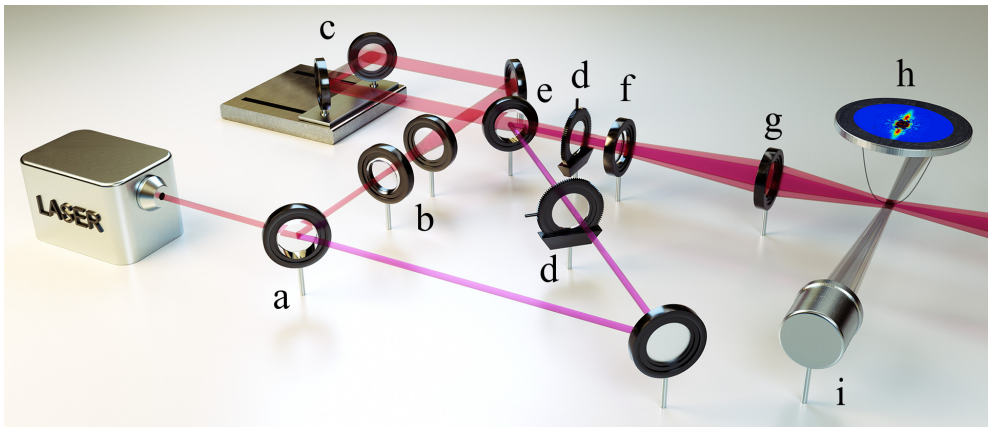

Figure 7.1: Schematic view of the experimental setup. The probe (purple) and pump (red) pulses are separated in a dichroic mirror (a). The pump beam divergence is controlled by a telescope (b). The time delay between pump and probe is controlled by a motorized micrometer translation stage (c). The polarizations of both beams can be rotated individually with two $\lambda/2$-plates, (d). The two laser beams are merged in a dichroic mirror (e). Both beams are expanded, (f), before focused into the interaction region with a 150mm focal length lens, (g), and intersected with the ion beam (grey). Detached electrons (solid black lines) are projected onto the position sensitive detector inside the EIS, (h). The ion current is measured using a Faraday-cup (i). [87].

An ion source [78] was used to produce negative ions. C^- ions were produced from a solid graphite cathod and Si^- from a cathode consisting of compressed silicon powder. The vacuum system and EIS are described in detail elsewhere [71,75,76]. The ions produced in the

source were accelerated to 4.5 keV and mass selected in a Wien filter. After mass selection the beam was bent by 90° in a quadrupole deflector to remove any neutral atoms or molecules present in the beam. The ion beam was focused by an electrostatic lens into the interaction region where it was intersected with the two laser beams inside the EIS. A typical ion current of 100-200 nA and a beam waist of less than 1 mm were obtained in the interaction region. The EIS consisted of a set of electrodes projecting electrons emitted in the entire solid angle onto a stack of multichannel plates. A phosphor screen placed behind the MCPs gave off a light flash for each electron detected. The flash was detected by a 12bit CCD-camera with 1280x1024 pixels from *LaVision* using the accompanying software *Davis* [119]. The EIS was operated in the velocity mapping regime [79]. Electrons having the same momentum vector, $\mathbf{p}$, were projected onto the same point on the detector regardless of where in the focal volume they were ejected. This was achieved by a nonuniform electric field. The projection voltage used in the EIS was 1.6 kV. The detector was calibrated by single photon absorption of H^-. The absorbed photon initiated a p-wave detachment of the initial, $1s^2$, electron configuration. Three different photon energies producing photoelectrons with kinetic energies of 0.804 eV, 1.347 eV and 2.363 eV, yielding a calibration coefficient of $0.976(3)\times10^6$m/s per pixel of the CCD [75, 76]. The pump-probe laser scheme used in the experiment is shown in Fig. 7.1. The linearly polarized idler and signal outputs from an optical parametric amplifier, TOPAS [120] from *Light Conversion*, were used as the pump and probe pulses, respectively. The TOPAS was pumped by a 800 nm mode-locked femtosecond Ti:sapphire laser system, from Clark-MXR, at a repetition rate of 1kHz. The pump beam and the probe beam were separated using a dichroic mirror. The polarization axes of both laser beams were individually controlled by means of two $\lambda/2$-plates. The time delay between the pump and the probe pulses was controlled by changing the optical path length for the pump with the use of a motorized linear micrometer translation stage. The two laser beams were merged again using a dichroic mirror. A 150 mm (carbon) or 200 mm (silicon) focal length lens placed in front of the experimental chamber was used to focus both laser beams into the interaction region. The focal points along the beam direction were made to coincide by adjusting the divergence of the pump beam using a telescope. The focal sizes were diffraction limited. In order to decrease those, both beams were expanded by a negative lens. Focal sizes of $18\mu m$ (FWHM) and 10 μm (FWHM) (carbon) or $24\mu m$ (FWHM) and $13\mu m$ (FWHM) (silicon) for pump and probe pulses, respectively, were achieved. Both pulses were

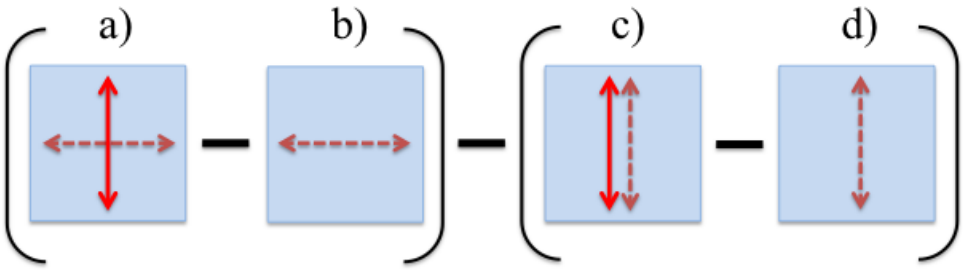

Figure 7.2: Acquisition procedure: Ionization yield with the parallel arrangement of the pump and probe polarizations (right parentheses) is subtracted from the yield with their perpendicular arrangement (left parentheses). Dashed and solid arrows represent the polarization direction of the pump and probe pulses, respectively.

of 100 fs duration. The pump had a pulse energy of 150 μJ, yielding a peak intensity of 8×10^{13}W/cm^2. The probe had a pulse energy of 240 μJ and a peak intensity of 4×10^{14}W/cm^2. First the two laser beams were overlapped in time using a BBO crystal. In the BBO crystal the pump and probe pulses were recombined into the 800 nm pulse produced by the Ti:Sapphire laser. This time was set to $t = 0$. The laser focal position in the ion beam was optimized by observing the detachment signal in the EIS. The atoms produced by the pump beam were subsequently exposed to the probe beam. The alignment effect in the probe step was observed by making four different recordings at each pump-probe time delay. Each recording is built up through 300 seconds of exposure time. First, an image is recorded with the pump and probe beam polarizations aligned perpendicularly (Fig. 7.2a). Second, a background image with only the pump laser present is recorded (Fig. 7.2b). The third image was obtained with the pump and probe beams aligned parallel (Fig. 7.2c). Finally, a background image with only the pump laser present is recorded (Fig. 7.2d). The effect of the probe beam is isolated by subtracting (b) from (a) and (d) from (c). The alignment effect in the carbon atom is visualized by comparing the probe yields obtained with the perpendicular and parallel polarization geometries.

7.2 Theoretical aspects

The system is simulated by statistically populating a density matrix. The ground state of C^- and Si^- is a quadruplet state with total spin

projection $M'_S \in \{-3/2, -1/2, 1/2, 3/2\}$. $M'_S = M_S + m_s$ where M_S is the total spin projection of the neutral atom and m_s is the spin projection of the electron that is to be detached. In the ground state of C^- and Si^-, $m_s \in \{-1/2, 1/2\}$ and $M_S \in \{-1, 0, 1\}$. $M_S = 0$ and $M_S \neq 0$ are equally populated. As mentioned previously the detachment rate for electrons with $m_l = 0$ is higher than that for $m_l \neq 0$. Since the ground state of the negative ion has three $2p$ electrons in its valence shell, there will be one electron occupying each of the three subshells $m_l = -1, 0$ and 1. Detachment of the $m_l = 0$ electron leaves the residual atom in a $M_L = 0$ state, while detachment of an $m_l = \pm 1$ electron leaves the atom in an $M_L = \mp 1$ state. With defining the detachment rate ratio between electrons with $m_l = 0$ and $m_l \neq 0$ to be d_{NI}, states with M_L is given a weight W_{M_L} by

$$W_{M_L} = \begin{cases} d_{NI}, & M_L = 0 \\ 1, & M_L \neq 0 \end{cases} \tag{7.1}$$

The weight W_{M_L} is found by simulating strong field detachment using a Keldysh-like Strong Field Approximation theory (SFA) [65] developed by Gribakin and Kuchiev [69]. The spatiotemporal intensity distribution in the laser focus is taken into account as well as the depletion of negative ions. The simulation routine is described in more detail in [71]. By integrating the total number of events in the simulation the ratio has been determined to be $d_{NI} = 27.4$ for carbon and $d_{NI} = 19.9$ for silicon.

With the statistical weights given by Eq. (7.1) the density operator for the neutral atoms at time $t = 0$ is given by

$$tr(\rho(0))\rho(0) = \sum_{M_L=-1}^{1} \sum_{M_S=-1}^{1} W_{M_L} |M_L, M_S\rangle \langle M_L, M_S| \tag{7.2}$$

The $tr(\rho(0))$ on the left hand side of Eq. (7.2) represents the fact that the right hand side is not normalized. Note that even though ρ is diagonal in the $|M_L, M_S\rangle$ representation, it will have non-zero off-diagonal entries in the $|JM_J\rangle$ basis and therefore describes a coherently populated state. The time evolution of the density operator is given by

$$\rho(t) = e^{-(it/\hbar)H} \rho(0) e^{(it/\hbar)H} \tag{7.3}$$

where H is the hamiltonian of the system.

A reduced density operator $\rho^{M_L}(t)$ can be constructed by taking the partial trace with respect to the spin magnetic quantum number space

$$\rho^{M_L}(t) = tr_{M_S}(\rho(t)). \tag{7.4}$$

The population $p_{M_L}(t)$ of atoms in state M_L at time t is then given by the projection of the reduced density operator onto the state $|M_L\rangle$.

$$p_{M_L}(t) = \langle M_L | \rho^{M_L}(t) | M_L \rangle \tag{7.5}$$

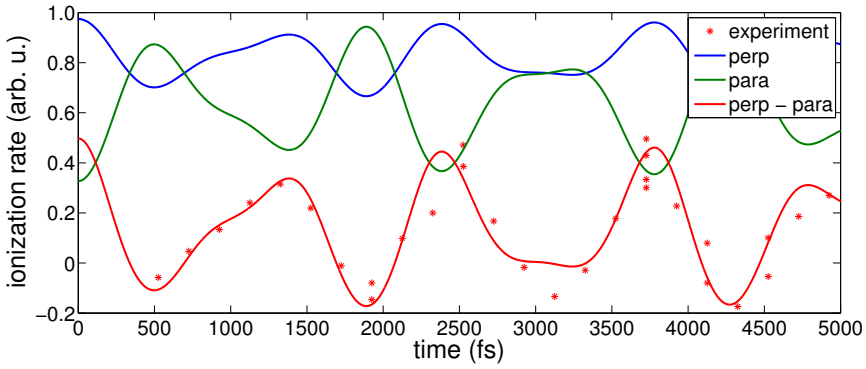

Figure 7.3: Ionization rate of carbon. Blue and green lines represent the ionization rate with the pump and probe beam polarizations aligned perpendicular and parallel with respect to each other, respectively. The red line is the parallel result subtracted from the perpendicular results. Stars represent experimental data.

These populations are then ionized using the same scheme as above for the detachment producing the ionization rate as a function of the time delay, as can be seen in Fig. 7.3 for carbon and Fig. 7.4 for silicon. The difference between the ionization rate for perpendicular and parallel pump beam is also formed and compared to the corresponding experimental results. Note that the amplitude of the experimental data has been scaled to the theoretical curve. The reduced amplitude of the experimental data is due to photoelectrons produced through other channels which do not display an alignment effect, and averaging over the duration of the laser pulses.

7.3 Results

Figure 7.5a, b and c present momentum and angular resolved photoelectron spectra of ionized electrons from aligned carbon atoms recorded

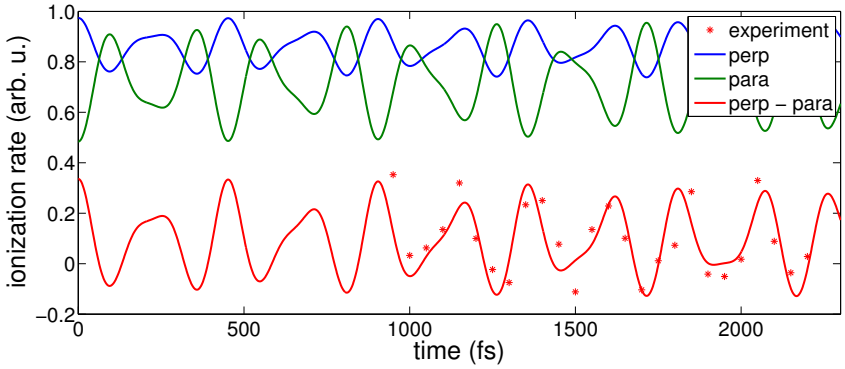

Figure 7.4: Ionization rate of silicon. Blue and green lines represent the ionization rate with the pump and probe beam polarizations aligned perpendicular and parallel with respect to each other, respectively. The red line is the parallel result subtracted from the perpendicular results. Stars represent experimental data.

at pump-probe delays of 2000 fs, 2300 fs and 2600 fs, respectively. The momentum of the electrons are represented by the distance from the point of impact to the center of the image. The probe laser polarization is vertical in all the images. $P_{\parallel}$ and $P_{\perp}$ refer to electron momenta measured parallel and perpendicular to the laser polarization direction, respectively. The main difference in the images are the number of high-energy electrons emitted along the laser polarization. These electrons are seen as vertically oriented jets. An electron momentum of 1.5 a.u. corresponds to an absorption of 45 photons.

The time dependence of the alignment effect is visualized by integrating the number of electrons on the detector within the area marked by the blue rectangles (Fig. 7.5d). The yield is plotted as a function of the pump-probe time delay. The result of experiment on the carbon atom is presented in Fig. 7.7. The pump-probe delay was varied between 600 fs and 5000 fs. We observe a periodic modulation of the ionization yield. The result from an experiment on silicon, where the same method has been applied is presented in Fig. 7.8. The time span investigated in silicon was 950 fs to 2200 fs. A sum of three cosine functions

$$f(t) = \alpha + \beta\cos(\frac{2\pi}{\tau_{01}}(t+\Delta)) + \gamma\cos(\frac{2\pi}{\tau_{02}}(t+\Delta)) + \epsilon\cos(\frac{2\pi}{\tau_{12}}(t+\Delta)), \quad (7.6)$$

were fitted to each of the two data sets. Here $\tau_{01,02,12}$ are the three expected quantum beats discussed previously. There is a clear oscillation in the yield of photoelectrons depending on the pump-probe delay. The larger fine structure splitting in silicon compared to carbon

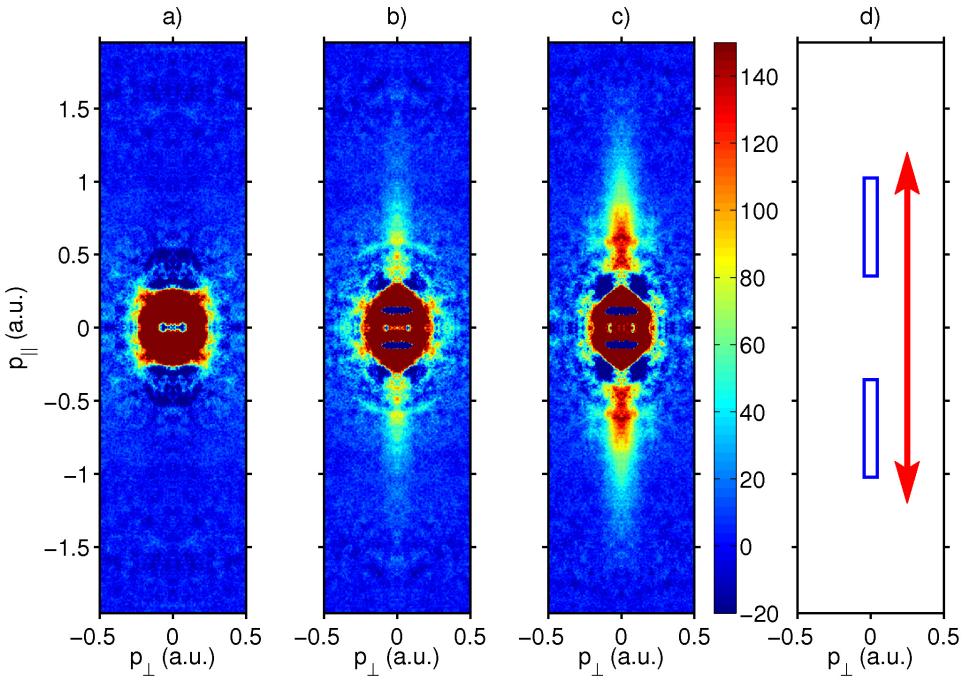

Figure 7.5: Images recorded at time delays between pump and probe pulses of 2000fs, 2300fs and 2600fs. A strong modulation is observed. The amount of ionized high-energy electrons depends strongly on the phase of the created wave packet in ground state of the atom. $P_{\|}$ and $P_{\perp}$ (perpendicular) refer to the electron momenta measured parallel and perpendicular to the laser polarization direction, respectively.

gives a time period approximately five times shorter than in carbon. The agreement between the time periods calculated from $\tau = \Delta E/h$ using tabulated fine-structure splittings [121] and experimentally obtained values are excellent in the case of the strongest observed beat, J_{12}.

Discussion

As described in section 7.2, the detachment rate via tunneling has a strong dependence on the magnetic quantum number m_l, with substates having $m_l = 0$ displaying detachment rates substantially larger than those for substates with $m_l \neq 0$. After detachment the remaining neutral atom will be left in an aligned state with a hole in the $m_l = 0$ distribution. A plot of the wavefunction of such a hole is shown in Fig. 7.6. Since we remove one out of three electrons from a spherically symmetric state we find it more expressive to show the spatial probability distribution of the created hole. The oscillation can be directly understood by observing the hole probability density plots shown in Fig. 7.6. Considering carbon, in Fig. 7.6a, a hole has been burnt along the polarization axis (vertical in the figure). The photoionization yield at this instance is very low. The electron density along the polarization axis has then been depleted, corresponding to the situation shown in Fig. 7.5a. 600 fs later, shown in Fig. 7.6c, the time evolution of the different substates has changed the electron distribution completely. The partial waves are now interfering constructively along the laser polarization direction. The electron density along the laser polarization is substantially larger, and the ionization yield is enhanced, corresponding to (Fig. 7.5c). The population along the laser polarization axis in the atom is projected directly onto the detector. We interpret the oscillation in the yield of photoelectrons as a periodic spatial rearrangement of the electron density in the atom.

In table 7.1 the beat periods calculated from the tabulated fine-structure splittings are presented together with the experimental results acquired from the fit of Eq. 7.6. In both carbon and silicon the main beat frequency observed is $J_{1\leftrightarrow 2}$. We create a wave packet in the carbon atom and the motion of the wave packet gives rise to an periodic rearrangement in the electron probability density along the laser polarization direction. The electron density is probed by strong field ionization projecting the spatial part of the electronic wavefunction onto the detector. We see a clear oscillation in the ionization yield corresponding

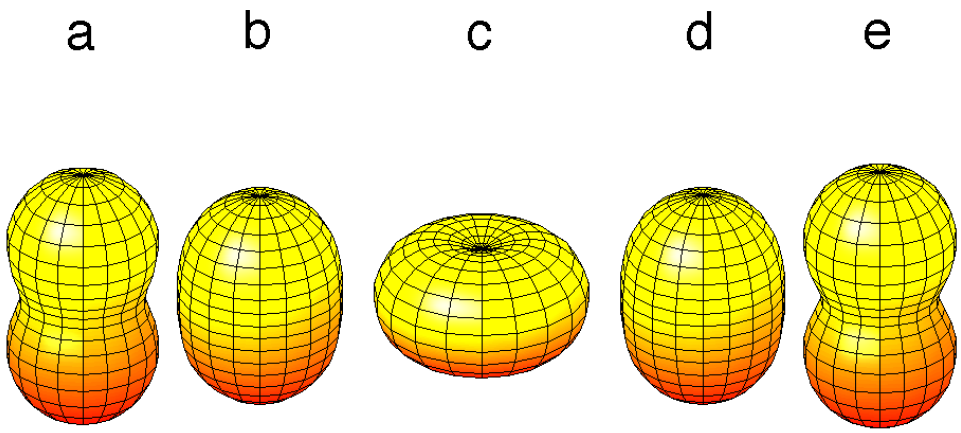

Figure 7.6: Spatial hole density distributions in the carbon atom. (a) The distribution after exposure to a strong laser field where a hole has been burnt along the axis of polarization (vertical in the figure). (b) The hole distribution after 300 fs. (c) The probability distribution after 600 fs, where the wave package movement has filled the hole along the laser polarization. (d) The probability distribution after 900 fs. (e) Revival of the initial hole distribution takes place 1200 fs after the wave packet is created.

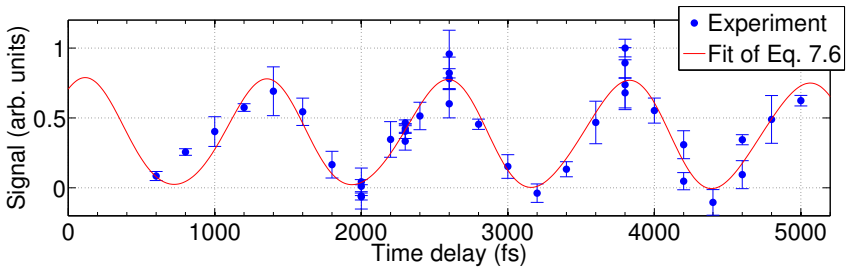

Figure 7.7: The number of high-energy electrons emitted from the aligned carbon atoms in the ionization step plotted as a function of the time delay between the pump and probe pulses.

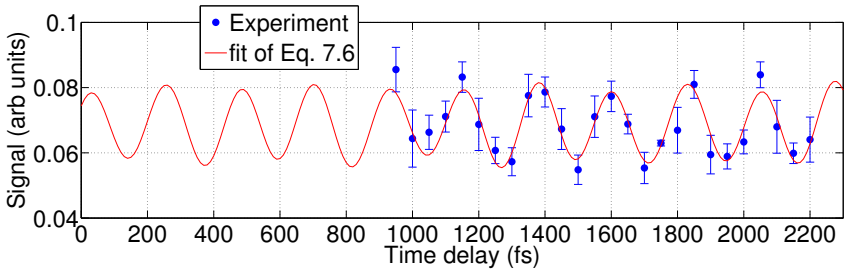

Figure 7.8: The number of high-energy electrons emitted from the aligned silicon atoms in the ionization step plotted as a function of the time delay between the pump and probe pulses.

Table 7.1: Carbon and Silicon

Carbon	ΔE (meV)	$\tau_{cal} \pm \sigma$ (fs)	$\tau_{exp} \pm \sigma$ (fs)	Rel. Amp.
$J_{0\leftrightarrow1}$	2.03	2034	1931 ± 1456	0.01 ± 0.075
$J_{0\leftrightarrow2}$	5.38	769	637 ± 23	0.081 ± 0.070
$J_{1\leftrightarrow2}$	3.35	1235	1229 ± 16.5	1 ± 0.056
Silicon				
$J_{0\leftrightarrow1}$	2.03	433	408 ± 13.2	0.139 ± 0.12
$J_{0\leftrightarrow2}$	5.38	149	175 ± 6.7	0.049 ± 0.12
$J_{1\leftrightarrow2}$	3.35	228	225 ± 2.7	1 ± 0.12

to an electronic wave packet moving in the valence shell of the carbon and silicon atoms. SFA simulations in combination with a density matrix formalism support the view of a spatially moving wave packet in the valence shell of the carbon atom. No sign of decoherence is visible within the investigated time window of carbon and silicon. The same experiment was also conducted on germanium. In this case, however, the $J_{1\leftrightarrow2}$ beat period is 40 fs, which is too short to be observed with our 100 fs long laser pulses. Further investigations on the time scale of decoherence are in progress. We have investigated carbon and silicon, which are of interest not only in physics but also in biochemistry and material science. The method used is general and can be applied to a wide field of quantum systems such as other atomic elements or molecules. Investigations of negatively charged diatomic silver and germanium molecules are underway where we intend to create and observe a vibrational wavepacket in the neutral species of the molecule.

The authors greatly appreciate the fruitful discussions with Sten Salomonson. HH and IK acknowledge the support by the Deutsche Forschungsgemeinshaft, Grant No KI865/3-1. ME acknowledges Marie Curie Actions and the ICONIC network. Financial support from the Swedish Research Council is gratefully acknowledged by DH.

CHAPTER 8

Threshold photodetachment in a repulsive potential

A. O. Lindahl[1], J. Rohlén[1], H. Hultgren[1,2], I. Yu. Kiyan[2], D. J. Pegg[3], C. W. Walter[4] and D. Hanstorp[1].

[1]*Department of Physics, University of Gothenburg, 412 96 Gothenburg, Sweden.*

[2]*Albert-Ludwigs-Universität, D-79104 Freiburg, Germany.*

[3]*Department of Physics, University of Tennessee, Knoxville, TN 37996, USA.*

[4]*Department of Physics and Astronomy, Denison University, Granville, Ohio 43023, USA.*

published in Physical Review Letters **108**, 033004 (2012).

We report on the first experimental observation of a new threshold behavior observed in the 5 ^2G partial channel in photodetachment of K^-. It arises from the repulsive polarization interaction between the detached electron and the residual K(5 ^2G) atom, which has a large negative dipole polarizability. In order to account for the observation in the K(5 ^2G) channel, we have developed a semiclassical model that predicts an exponential energy dependence for the cross section. The measurements were made with collinear laser-ion beams and a resonance ionization detection scheme.

Inelastic scattering processes involving resonant excitation have provided a wealth of information on bound and quasibound states, whereas less emphasis has been placed on nonresonant or continuum processes. Studies of threshold behavior in such processes are of fundamental interest since they allow us to better understand the nature of the interactions between particles created by fragmentation. For example, Einstein's interpretation [2] of the frequency dependence of the threshold

position in the photoelectric effect was instrumental in the development of quantum mechanics. Threshold effects have been shown to be important in diverse areas of physics including atomic and molecular, subatomic and solid state physics [122]. Specific examples include nuclear halo states [123], evaporative cooling of fermionic atoms [124], molecular dissociation [125] and the neutron capture process [126].

In the field of atomic physics, the interpretation of particle scattering and photo-fragmentation experiments is aided by the fact that the interparticle interactions are well understood. One particularly interesting photo-fragmentation process is photodetachment. Here an electron is ejected from a negative ion following the absorption of a photon. Studies of threshold behaviors in one-electron photodetachment are of fundamental interest. Just above threshold, the detached electron moves very slowly relative to the residual atom and its motion and that of the remaining atomic electrons become highly correlated. In this system, subtle correlation interactions are not masked by far stronger Coulomb forces, which is the case in photoionization. Wigner showed that the centrifugal potential determines the behavior of the cross section in the threshold region for two-particle breakup reactions for which the interaction approaches zero faster than r^{-2} [23]. The cross section is then given by $\sigma_{\mathrm{W}} \sim (E_{h\nu} - E_{\mathrm{th}})^{\ell+1/2} = {E_e}^{\ell+1/2}$, where $E_{h\nu}$ is the photon energy, E_{th} is the threshold energy and E_e and ℓ are the kinetic energy and angular momentum of the detached electron, respectively.

The Wigner law is strictly valid only at threshold. However, good agreement between the Wigner law and measured cross sections are typically observed up to energies on the order of 10 meV above threshold, see for example Refs. [127–129]. In one particular case, however, when detachment of an inner-shell electron was investigated, the data followed the Wigner law up to 2 eV above threshold [130]. The lowest order correction terms to the Wigner law include the effects of the finite size of the initial state wave function [131] and the polarizability of the residual atom [132]. Several theoretical studies of threshold behavior in the presence of an attractive polarization interaction have been made [132, 133]. The approximations made in the model by O'Malley [132], however, severely reduce its applicability when the polarizability is large [134]. In photodetachment experiments on Li^- and K^-, in which the atoms were left in highly polarizable states, a more advanced modified effective range model [133] had to be applied to describe the observed threshold behaviors [134].

In this Letter we present the results of an experiment on one-electron

photodetachment from the K^- ion. Specifically, the partial cross sections for the $K^- + e^-(\epsilon d)$ and K(5 ^2G)$+e^-(\epsilon f)$ final state channels have been measured. The dipole polarizabilities of the K atom in the K(5 ^2F) and the K(5 ^2G) states have been calculated to be $3\,936\,137$ and $-3\,097\,696$ a.u., respectively [135]. The polarizability of the $4\,^2S$ ground state is 307 a.u. The large polarizabilities arise since the 5 ^2F and 5 ^2G states are energetically close (separated by only 1.3 meV [136]) and thus interact strongly in an external field, while other states are far away. Because of the large polarizabilities, the polarization potential is expected to play a significant role in determining the behavior of the cross section above both thresholds. Our measurements exhibit very different behaviors above the two thresholds: a steplike onset in the K(5 ^2F) channel, while the increase of the cross section in the K(5 ^2G) channel is very slow. This difference is attributed to the sign difference of the polarizability and thus whether the final state interaction is attractive or repulsive. This is the first reported observation of the effect of a strong, repulsive polarization interaction on a photodetachment threshold.

The effects of the attractive and repulsive potentials on the onset of production of electrons in photodetachment are reminiscent of the effects seen in the nuclear β decay distributions [137]. In β^- decay there is a steplike onset at the low-energy end of the electron distribution, in sharp contrast to the suppressed production of low-energy β^+ particles. This difference is explained by the attractive and repulsive Coulomb interactions, respectively, in the final states.

8.1 Methods

In order to measure the small partial cross sections for the K(5 ^2F) and K(5 ^2G) channels, the experiment was performed in a collinear laser-ion beam geometry to maximize the sensitivity. A resonance ionization scheme was used to distinguish the two channels. The experiment was performed at Gothenburg University Negative Ion Laser Laboratory. Negative ions of potassium were created from K_2CO_3 in a sputter ion source and were accelerated to 6 keV energy. The ion beam was mass selected in a magnetic sector before it was bent by an electrostatic quadrupole deflector into an interaction region defined by two 3 mm apertures placed 61 cm apart. This part of the setup has been described in detail by Diehl *et al.* [138]. The interaction region is shielded against stray electric fields by means of a stainless steel

tube centered along the path of the ions. A SIMION [139] simulation showed that the residual electric field in the interaction region is substantially smaller than 1 V/cm. An electric field of this strength would result in a mixing of the $5\ ^2F$ and $5\ ^2G$ states that is less than 10^{-4}, and this effect can thus be neglected. In the interaction region, the ion beam was merged with two copropagating laser beams. A pulsed UV laser was used to photodetach the K^- ions. A pulsed IR laser resonantly excited the residual atoms to specific Rydberg states. After the interaction region, an inhomogeneous electric field and a position sensitive detector (PSD) served as a Rydberg state analyzer. The analyzer will be described in more detail in a forthcoming publication. Rydberg atoms in different states were field ionized at different positions in the field so that the resulting positive ions were deflected at different angles into the detector. Information on where the ions hit the PSD was used to distinguish between different Rydberg states and to separate the field-ionized Rydberg atoms from positive ions created in sequential photodetachment-photoionization by two UV photons. Another advantage of the PSD was that it enabled subtraction of diffuse background processes. The electrical field in the Rydberg analyzer also deflected the negative ion beam into a Faraday cup. For each shot of the two lasers, the data from the PSD were recorded together with the measured wavelength and pulse energy of the UV radiation and the ion current.

The ion current in the interaction region was on the order of 1 nA. Both lasers were Nd:YAG-pumped Optical parametric oscillators delivering about 6 ns pulses with repetition rates of 10 Hz. The specified bandwidths were 0.2 $cm^{-1} \approx 25\ \mu$eV. The pulse energy of the IR laser after the chamber was approximately 0.2 mJ, which was sufficient to saturate the resonant transitions to the Rydberg states. The UV energy was approximately 0.7 mJ, far from saturating the nonresonant photodetachment process. In order to investigate the threshold regions, the UV radiation was tuned from 4.290 to 4.352 eV in the ion rest frame. The IR laser was tuned to one of the resonant transitions $7\ ^2S \rightarrow 25\ ^2P$, $5\ ^2F \rightarrow 23\ ^2D$ or $5\ ^2G \rightarrow 22\ ^2F$, which, in the rest frame, correspond to 562.050, 519.566, and 516.461 meV, respectively [136]. The UV pulse arrived at the chamber approximately 50 ns before the IR pulse.

Counts in a selected area of the detector were summed, and the background around the selected area was subtracted. This number was normalized with respect to the ion current and the pulse energy of the UV laser and finally sorted and binned based on the measured UV wavelength. The measured photon energies were converted to the ion

rest frame based on the kinetic energy of the ion beam. This induced an uncertainty in the energy scale that is less than 20 μeV, which is on the order of the laser bandwidth.

8.2 Results

Figure 8.1 shows the thresholds for photodetachment to the K(5 ^2F) and K(5 ^2G) channels in panels (a) and (b), respectively. Note that the energy range in (a) is 25 times smaller than in (b). Figure 8.1 (a) covers the fast onset of the cross section in the K(5 ^2F) channel, which plateaus approximately 200 μeV above the threshold. The small signal just below the channel opening is caused by the finite bandwidth of the laser. This steplike rise at threshold is the same energy dependence that has been seen in photodetachment experiments leaving the residual atom in a state with high positive polarizability [134], as discussed above. The observed threshold behavior deviates strongly from the Wigner law. Even with the correction term of O'Malley [132], the Wigner law cannot be used to reproduce any part of the data in Fig. 8.1 (a).

With the large positive polarizability, the height of the centrifugal barrier in the K$(5\ ^2F) + e^-(\ell = 2)$ channel is reduced to only 31 μeV. At detachment energies above this value, the electron can pass above the barrier. Therefore, the cross section is expected to rise very rapidly to its maximum value. This is in good agreement with Fig. 8.1 (a), in which the cross section reaches 80 % of the maximum value at 100 μeV above threshold.

In sharp contrast, the cross section for the K(5 ^2G) channel, shown in Fig. 8.1 (b), has a very slow onset. Moreover, a broad resonance is seen to modulate the cross section at energies around 4.32 eV. Except for this modulation, the cross section is increasing over the whole observable range. The figure contains data up to 54 meV above threshold, which is just below the K(7 ^2P) channel opening.

The presence of the resonance in Fig. 8.1 (b) complicates the analysis of the nonresonant threshold behavior. The same resonance appears in the partial cross section for the K(7 ^2S) channel (not shown), which opens at 4.255 eV [136, 140]. A fit of a Shore profile to this resonance yielded a resonance energy $\mathrm{E_r^{7\,^2S}} = 4.320(3)$ eV and a width $\Gamma_\mathrm{r}^{7\,^2\mathrm{S}} = 25(9)$ meV.

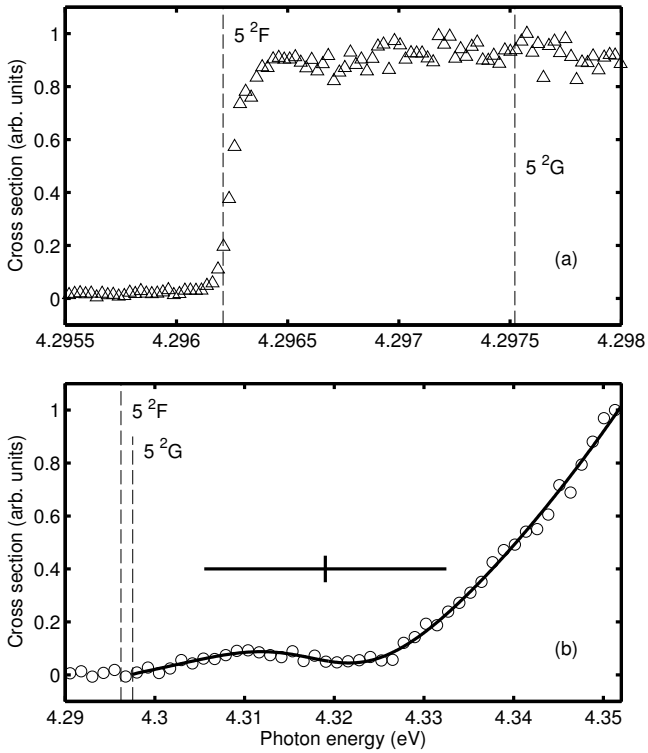

Figure 8.1: Partial photodetachment cross sections measured in the K(5 ^2F) channel (a) and K(5 ^2G) channel (b). Note that the energy range in (a) is 25 times smaller than in (b). The dashed vertical lines indicate the experimentally known threshold positions [136, 140]. The solid line in (b) is a fit of the function in Eq. (8.3) with σ_{th} from Eq. (8.2). The resonance position and width, as extracted from the fit, are indicated by the vertical and horizontal bars in (b).

The primary interest of this Letter is the nonresonant threshold behavior of the K(5 ^2G) photodetachment channel. Photodetachment into this channel yields an electron emitted primarily as an f wave near threshold and hence the Wigner law predicts a cross section that should scale as ${E_e}^{7/2}$. However, due to the large polarizability of the 5 ^2G state, a deviation from the Wigner law on the order of 20 % is expected at energies as low as 10 μeV above threshold [132].

8.3 Theory

As was the case for the threshold in the K(5 ^2F) channel, the Wigner law with the O'Malley correction fails to reproduce the shape of the

onset seen in Fig. 8.1 (b). Analysis of the experimental data therefore requires a treatment in which the polarization potential is included in a more sophisticated manner. As discussed above, modified effective range theories have been developed to describe thresholds in the presence of a large positive dipole polarizability. To gain a qualitative understanding of the observed cross section we have developed a semiclassical model that takes the negative polarizability into account.

In this model we consider the effective potential $U(r) = \ell(\ell+1)/2r^2 - \alpha/2r^4$ (in atomic units) for an electron moving in the field of an atom with the static dipole polarizability α. Since the polarizability of the (5 ^2G state is negative, this represents a purely repulsive potential. By comparing the centrifugal and induced dipole terms, one estimates that, with the polarizability calculated by Liu [135], the polarization potential dominates for electron energies larger than 1 meV. Since the energy range in the experiment extends significantly above this value, we consider the limiting case where the centrifugal potential is neglected. Furthermore, the repulsive potential spatially separates the classically allowed regions of the initial and final states to such an extent that it is only the exponential tails of the wave functions, in the classically forbidden region, that contribute significantly to the transition amplitude. In the classically forbidden region, the wave function of the free electron in the final state can be expressed by using the semiclassical approximation:

$$\psi_k(r) = \frac{C(E_e)}{r\sqrt{p(r)}} \exp\left(-\int_r^{r_0} p(x)\,dx\right), \quad r < r_0, \tag{8.1}$$

where $k = (2E_e)^{1/2}$ denotes the electron momentum, $p(r) = (|\alpha|/r^4 - 2E_e)^{1/2}$, $r_0 = (|\alpha|/2E_e)^{1/4}$ is the classical turning point, and $C(E_e) \sim E_e^{-1/4}$ is a normalization coefficient on the $k/2\pi$ momentum scale. The integral in Eq. (8.1) can be expressed in terms of the hypergeometric function ${}_2F_1\left[-\frac{1}{2}, -\frac{1}{4}; \frac{3}{4}; (\frac{r}{r_0})^4\right]$. Since the region of significance of the wave function overlap lies at $r << r_0$, ψ_k can be expanded in a power series of $(r/r_0)^4$. Taking only the first-order term into account results in an expression for ψ_k with separated r and E_e dependencies. This form allows calculation of the energy dependence of the photodetachment cross section, which is defined by the integral of the squared transition amplitude over the momentum space of the detached electron. Since the transition amplitude depends on the energy E_e only through $\psi_k(r)$, it has the same energy dependence as the exponential tail (8.1) of the continuum wave function. The integral over the momentum space of

final states yields a factor ${E_e}^{1/2}$, which cancels the square of $C(E_e)$. This results in an analytic function for the cross section of the form

$$\sigma_{\rm th} \sim \exp\left[D\,{E_e}^{1/4}\right], \tag{8.2}$$

where $D = 2^{11/4}\,\pi^{3/2}\,|\alpha|^{1/4}/\Gamma^2(\frac{1}{4}) \approx 2.850\,|\alpha|^{1/4}$ is a numerical constant. Very close to threshold, the centrifugal potential cannot be neglected. The Wigner law should therefore give a better description of the cross section for small energies. As mentioned previously, however, the range over which the Wigner law correctly describes the energy dependence of the cross section is very small due to the large polarizability of the 5 ^2G state. In situations where $\ell = 0$, on the other hand, the induced dipole potential is indeed the longest range interaction and the model is thus expected to be valid at threshold. In such cases, Eq. (8.2) represents the true behavior of the cross section, including the noticeable property that the cross section is finite at threshold.

The data shown in Fig. 8.1 (b) have been fitted with a function that takes the presence of a resonance due to a doubly excited state into account. The function is a slightly modified expression by Liu and Starace [141]:

$$\sigma_{\rm pd} = A\,\sigma_{\rm th}\left(1 + \frac{\epsilon a + b}{1+\epsilon^2}\right), \tag{8.3}$$

where $\epsilon = (E_{h\nu} - E_{\rm r})/(\Gamma_{\rm r}/2)$. The nonresonant component, $\sigma_{\rm th}$, is represented by Eq. (8.2). The electron that is emitted in the decay of the doubly excited state experiences the same repulsive polarization potential as electrons emitted directly by photodetachment. The influence of the resonance can therefore be reasonably approximated as a product of the threshold law and a Shore profile, as in Eq. (8.3). The function contains 6 free parameters: the common amplitude factor A, the factor D in the exponent, the resonance energy $E_{\rm r}$, the resonance width $\Gamma_{\rm r}$, and the Shore parameters a and b, characterizing the shape of the resonance. Tabulated experimental values [136, 140] were used for the threshold energy in the fitting procedure. Our model yielded a good fit to the data and the extracted energy and width of the resonance were $\mathrm{E}_{\rm r}^{5\ {}^2{\rm G}} = 4.319(4)$ eV and $\Gamma_{\rm r}^{5\ {}^2{\rm G}} = 27(4)$ meV, respectively. The fit is shown in Fig. 8.1 (b) together with a horizontal bar indicating the resonance parameters. The resonance parameters are in agreement with those extracted in the K(7 ^2S) channel and those calculated by Liu [135]. Table 8.1 compares the three sets of values. We also performed the fitting using fixed values of $E_{\rm r}$ and $\Gamma_{\rm r}$ given by either the fit to the K(7 ^2S) channel data or the calculation by Liu [135]. These fits,

Table 8.1: A comparison of resonance parameters, with quoted uncertainties representing 1 standard deviation.

Origin	Position, E_{r} (eV)	Width, Γ_{r} (meV)
K(5 ^2G) channel	4.319(4)	27(4)
K(7 ^2S) channel	4.320(3)	25(9)
Calculation [135]	4.32339	27.7183

with only four free parameters, gave curves that are indistinguishable from the fit shown as the solid line in Fig. 8.1 (b).

The good fit to the data in Fig. 8.1 (b) and the good agreement with resonance parameters in Table 8.1 indicates that the nonresonant background can be well represented by the exponential function in Eq. (8.2). This function includes the polarizability of the excited atomic state. This means that it is, in principle, possible to extract an estimate of the polarizability of the 5 ^2G state from the shape of the curve shown in Fig. 8.1 (b). The result from the fit gives a polarizability of -2.7×10^4 a.u., indeed a very large value, although significantly smaller than -3.1×10^6 a.u. as calculated by Liu [135]. However, we do not expect our model, which was developed to achieve a qualitative understanding of the threshold behavior, to be able to give a reliable value of the polarizability. In particular, to neglect the centrifugal potential and consider only the polarization interaction is most likely an oversimplification. In addition, the simple $1/r^4$ radial dependence of the induced dipole potential might not be a complete description of the polarization interaction, especially for small radial distances. When the interaction between the atom and the free electron is weak, a perturbative treatment results in the simple $1/r^4$ radial dependence. When, on the other hand, the interaction becomes strong, nonperturbative methods may be needed. This could result in a more complicated radial dependence of the repulsive potential than used in our analysis. It might also be important to take the dynamical effects on the polarizability into account in a full model of the threshold behavior.

8.4 Conclusion

In summary, we have investigated near-threshold cross sections for two channels in which the residual atom is left in highly excited and highly polarizable excited states. The channels differ in that the sign of the dipole polarizability is different. The induced dipole interaction

is so strong that it dominates and determines the general shape of the photodetachment cross sections. In the case of the K($5\,^2F$) channel, the attractive polarization potential reduces the height of the centrifugal barrier. This leads to a steep onset of the cross section, which plateaus once the electron can pass above the barrier. In sharp contrast, the K($5\,^2G$) channel exhibits a much slower onset above threshold. This is due to the repulsive potential, which precludes a large overlap of the wave functions at low electron energies. We have shown that a qualitative understanding of the shape of the cross section can be obtained through a semiclassical model. The resulting exponential energy dependency has been successfully used to represent the nonresonant component in a fit to the data, which also includes a resonance.

It is expected that the data and model presented in this Letter will initiate further theoretical work, resulting in a more detailed understanding of the observed threshold behaviors. There are many pairs of states in the alkali atoms that have large polarizabilities with opposite signs. It is our intention to systematically probe these states in order to investigate the threshold behaviors as a function of polarizability.

We thank Sten Salomonson for enlightening discussions on polarizability and induced polarization potentials. Financial support from the Swedish Research Council is gratefully acknowledged. CWW received support from the Wenner-Gren Foundation, the Andrew W. Mellon Foundation, and NSF Grant No. 0757976. HH and IK acknowledge the support by the Deutsche Forschungsgemeinshaft, Grant No KI 865/3-1.

CHAPTER 9

Experimental studies of partial photodetachment cross sections in K^- below the K($7\,^2P$) threshold

A. O. Lindahl[1], J. Rohlén[1], H. Hultgren[1,2], I. Yu. Kiyan[2], D. J. Pegg[3], C. W. Walter[4] and D. Hanstorp[1].

[1]*Department of Physics, University of Gothenburg, 412 96 Gothenburg, Sweden.*

[2]*Albert-Ludwigs-Universität, D-79104 Freiburg, Germany.*

[3]*Department of Physics, University of Tennessee, Knoxville, TN 37996, USA.*

[4]*Department of Physics and Astronomy, Denison University, Granville, Ohio 43023, USA.*

published in Physical Review A **85,** 033415 (2012).

A collinear beams apparatus has been used to determine photodetachment cross sections for K^- in the photon energy range 4.250–4.360 eV. State selective detection, utilizing a resonance ionization scheme, was applied to measure partial cross sections for those channels which leave the residual K atoms in the excited $7\,^2S$, $5\,^2F$ and $5\,^2G$ states. The energy region studied encompassed the openings of the aforementioned channels, as well as the channel that leaves the K atom in the $7\,^2P$ state. Two previously unobserved resonances were seen in all three partial cross sections between the K($5\,^2G$) and K($7\,^2P$) thresholds. It is shown that a more reliable determination of resonance parameters can be made if the same resonances are observed in several channels. In the region below the K($5\,^2F$) threshold, three previously observed resonances were investigated [Kiyan et al. Phys. Rev. Lett. ***84****, 5979 (2000)]. A greatly increased modulation of the signal was obtained by detecting in the K($7\,^2S$) channel, instead of the K($5\,^2S$) channel used in the previous study.*

Furthermore, the shapes of the cross sections in the threshold regions are discussed. A detailed description of the apparatus and the experimental procedure employed is presented in the paper.

9.1 Introduction

The structure and reaction dynamics of negative ions are of fundamental interest. Due to the nature of the binding of the outermost electron in negative ions, they are significantly different from atoms and positive ions. The interaction in atoms and positive ions can be described by a Coulomb potential when the electron is at large distances from the core. A consequence of this is the infinite series of Rydberg states. In negative ions, on the other hand, the asymptotic potential is described by a much shorter ranged induced dipole potential. If the extra electron is close to the parent atom, a full many-body treatment is needed to describe the interaction. The short-range potential is able to bind only a finite number of states. Atomic negative ions usually have only a single bound state. The binding energy is typically one order of magnitude smaller than that of the isoelectronic atom. The standard method to gain information about the structure of negative ions is through the photodetachment process, in which an electron is emitted due to the absorption of a photon. Valuable information regarding electron-electron correlation can be obtained by comparing photodetachment data with results from atomic many-body calculations.

The general lack of bound excited states in negative ions excludes the observation of bound-bound transitions in most ions. In the continuum above the detachment limit, however, there exists a rich spectrum of doubly excited states. Some of these states have configurations that can be excited with single photon transitions from the ion ground state. These states can be viewed as an atom in an excited state to which an additional electron is attached. Doubly excited states are unstable and have lifetimes on the order of picoseconds. They decay via autodetachment to a neutral atom and a free electron. The properties of such states are substantially influenced by the effects of electron-electron correlation. A great amount of theoretical and experimental effort has been devoted to the prototype negative ion, H^- [142–148]. Here, two electrons move in the pure Coulomb field of the nucleus, a case resembling the helium atom. The negative ions of the alkali metals can be considered to be quasi two-electron systems in the frozen-core approximation. This is especially true for high lying doubly ex-

cited states, where the effects of penetration and polarization of the core are smaller. Previous experimental work in the field includes studies of Li^- [149, 150], Na^- [151] and K^- [152].

An interesting energy region is that just above the threshold for photodetachment. In this case the slow outgoing electron spends a significant time close to the core and the interaction between the electron and the residual atom becomes very important. The photodetachment cross section just above threshold can be described by the Wigner law [23]. Wigner showed that it is the effective centrifugal potential that determines the shape of the threshold cross section, which is given by

$$\sigma \sim {E_e}^{\ell+1/2}, \tag{9.1}$$

where ℓ and E_e are the angular momentum and the kinetic energy, respectively, of the outgoing electron. However, the energy range over which the dependency in Eq. (9.1) is valid is limited by the magnitude of other interactions such as the induced polarization interaction. O'Malley has developed a description that takes the polarizability of the residual atom into account [132], while the correction factor introduced by Farley described the effect of the finite size of the initial state wavefunction [131]. In an experiment reported by Sandström *et al.* [134] the threshold behaviors for photodetachment to final excited states with different, but large, positive polarizabilities were investigated. A modified effective range theory, developed by Watanabe and Greene [133], was successfully applied to the threshold data in this case. However, it is also possible for an excited atomic state to have a negative polarizability. This more unusual case was discussed in a recent publication [153] where the fundamentally different behaviors of the cross sections at the K(5 ^{2}F) and K(5 ^{2}G) thresholds were described. These two states have dipole polarizabilities of approximately the same large magnitude (10^6 a.u.), but with opposite sign [135]. A semiclassical model was developed to describe threshold cross sections in cases where the interaction in the final state is dominated by a negative polarizability of the residual atom. This model predicts a fundamentally different, exponential, energy dependence for the cross section given by the expression

$$\sigma \propto \exp\left[D{E_e}^{1/4}\right], \tag{9.2}$$

where the constant D depends on the polarizability as $D \propto |\alpha|^{1/4}$.

The present paper describes an investigation of the photodetachment of K^-. The experiment was performed using an upgraded collinear

beams apparatus at GUNILLA (Göteborg University Negative Ion Laser LAboratory). The apparatus and the experimental procedure employed are described in detail. The same facility was used in the study of threshold behaviors of the cross sections at the K(5 ^{2}F) and K(5 ^{2}G) thresholds [153] discussed above. In the present work, partial cross sections were measured for final state channels leading to the formation of the residual K atom in the excited 7 ^{2}S, 5 ^{2}F and 5 ^{2}G states. Two predicted resonances [135], which thus far have not been observed, were identified in the region between the K(5 ^{2}G) and K(7 ^{2}P) channel openings in all three partial cross sections. The advantage of investigating the same resonances in more than one detachment channel is illustrated in the paper. In the region between the K(7 ^{2}S) and K(5 ^{2}F) channel openings three resonances were observed in the K(7 ^{2}S) channel, in agreement with previous experimental [152] and theoretical [135] results. The measurements described in this paper were made possible by the use of an apparatus that combines high sensitivity and resolution with a high level of selectivity. This was achieved by a combination of a long collinear interaction region and a laser-based detection scheme.

9.2 Experiment

Figure 9.1 shows the optical excitation scheme used in the experiment. K^- ions were photodetached by UV photons generated by an optical parametric oscillator (OPO). The energy of the UV photons was substantially larger than the electron affinity of K, thus leaving the residual atoms in a distribution of final excited states. A state selective detection scheme based on resonance ionization was used to measure the partial cross sections to specific excited states of the K atom. A second OPO generated infrared radiation and its photon energy was tuned to match the transition energy from a chosen excited state of K to a Rydberg state. The Rydberg atoms thus produced were field ionized in an electric field, enabling the resulting positive ions to be separated from the negative ions and the neutral atoms. The positive ions were detected with a position sensitive detector. The three photodetachment channels studied in the present work are

$$\mathrm{K}^-(4\,^1S) + \gamma_{\mathrm{UV}} \rightarrow \mathrm{K}(7\,^2S) + e^-, \tag{9.3}$$

$$\rightarrow \mathrm{K}(5\,^2F) + e^-, \tag{9.4}$$

$$\rightarrow \mathrm{K}(5\,^2G) + e^-, \tag{9.5}$$

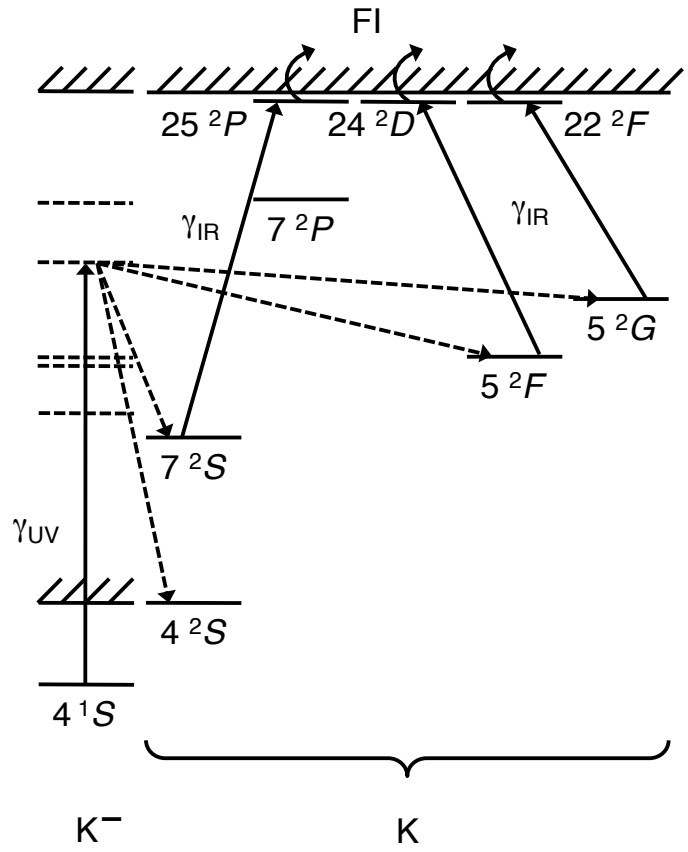

Figure 9.1: Partial energy level diagram (not to scale) of the K^- and K systems. A K^- ion absorbs a UV photon (γ_{UV}) and is promoted to a doubly excited state (dashed energy levels), which decays via autodetachment (dashed arrows). State selectivity in the detection is achieved by resonant excitation using an IR photon (γ_{IR}) followed by field ionization (FI).

which have threshold energies of 4.254 987(12), 4.296 210(14) and 4.297 522(12) eV respectively [136, 154]. The main uncertainty in the threshold energies results from the uncertainty in the electron affinity of potassium, which is 0.501 459(12) eV [154]. The energy range studied includes the openings of the three aforementioned channels as well as that of the K(7 ^{2}P) channel, which has a threshold energy of 4.353 636(14) eV.

Measurement of the partial cross sections to highly excited final states requires a method with high sensitivity and resolution and a high level of selectivity. A high sensitivity is needed since such cross sections are generally very small. The magnitude of the partial cross section for the K(7 ^{2}S) channel, for example, is predicted to be only 0.008 Mb at 4.26 eV [135]. The sensitivity of the measurement was enhanced by a large interaction volume, defined by the collinear overlap of the superimposed laser and ion beams, and by an efficient detection of the residual atoms. Furthermore, the energy separation of adjacent states is small at high levels of excitation, necessitating high energy-resolution and selectivity in the final state detection. The present experiment relies, for example, on the correct identification of the K(5 ^{2}F) and K(5 ^{2}G) channels, whose thresholds are separated by as little as 1.3 meV [136]. The state selective detection of these atoms via resonance ionization was the basis for the high selectivity. The energy resolution was enhanced by the large reduction in kinematic broadening brought about by the collinear interaction of the ion and laser beams [155]. In the present measurement the energy resolution was determined primarily by the bandwidth of the laser used for photodetachment, which is approximately 25 μeV.

The collinear laser and ion beams apparatus at GUNILLA is shown schematically in Fig. 9.2. Negative ions were produced in a cesium sputter ion source, from a sample of compressed K_2CO_3 powder, and were accelerated to 6 keV. A sector magnet was used for mass dispersion and a quadrupole deflector merged the ion beam with the laser beams. The beams were merged over a 61 cm long interaction region defined by two apertures with a diameter of 3 mm. The ion current through the interaction region was typically on the order of 1 nA. The apparatus was recently upgraded to improve the mass resolution and the transmission through the interaction region, as described in detail by Diehl *et al.* [138]. The sector magnet was only single focusing, therefore, two single focusing Einzel lenses were used in order to achieve a symmetric beam and improve the transmission through the system. The ion optics also included two Einzel lenses designed for symmetric focussing in two directions and a quadrupole triplet for beam shaping.

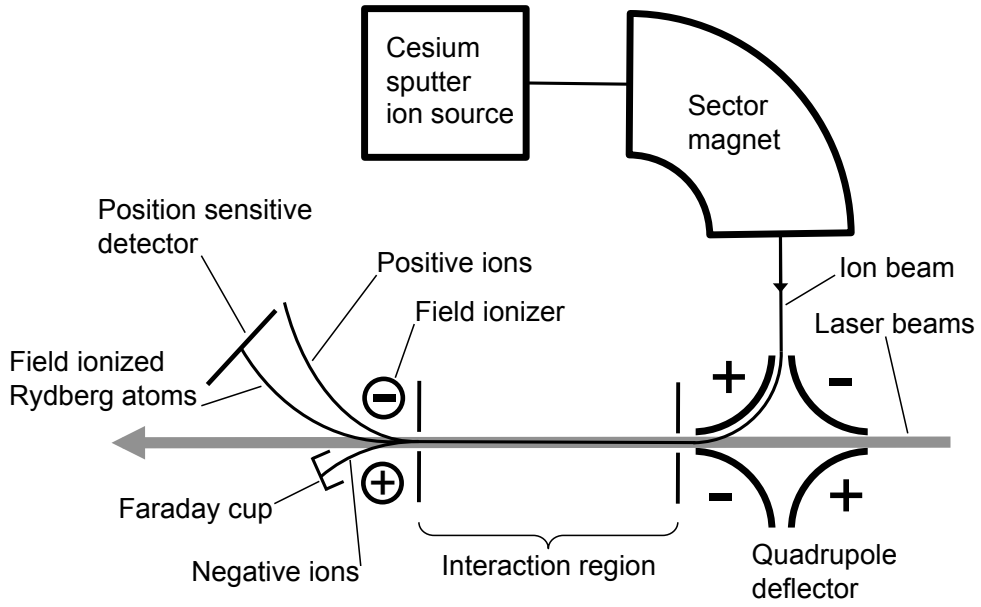

Figure 9.2: A schematic of the collinear beams apparatus. Two laser beams and an ion beam are superimposed in a collinear co-propagating geometry. The field ionizer separates the beam particles from the interaction region.

Two Nd:YAG-pumped OPOs were used in the experiment. They operated synchronously at a 10 Hz repetition rate and generated pulses of 6 ns duration and 25 μeV spectral bandwidth. The two OPOs have tuning ranges covering 0.65–5.6 eV and 0.25–0.92 eV, respectively. In the experiment, the photon energy of the UV radiation was tuned between 4.250 and 4.360 eV. The IR laser, on the other hand, was tuned to one of the resonant transitions $7\,^2S \rightarrow 25\,^2P$, $5\,^2F \rightarrow 24\,^2D$ and $5\,^2G \rightarrow 22\,^2F$, corresponding to photon energies of 562.050, 521.740 and 516.461 meV, respectively [136]. The UV and the IR beams were overlapped, co-propagating with the ion beam. They were merged prior of the chamber using a mirror that reflected UV radiation and transmitted IR radiation. The pulse from the IR laser was triggered to arrive 50 ns after the UV laser pulse. The jitter in the delay time was on the order of a few nanoseconds. After the chamber the laser beams were separated by a Pellin-Broca prism. The pulse energies of the two laser beams measured behind the interaction region, were approximately 0.7 mJ for UV radiation and 0.2 mJ for IR radiation. With such energies, the non-resonant photodetachment transition driven by the UV radiation was far from saturation. The resonant transition driven by the IR radiation was saturated.

OPOs typically suffer from an inherent problem when used for high resolution spectroscopy. The center frequency jitters from pulse to pulse. The bandwidth of each pulse is small but the effective bandwidth, when averaged over several pulses, is larger. To overcome this problem, the wavelength of each UV pulse was measured using a commercially available wavelength meter. The absolute accuracy of the device was 2.5 μeV. The wavelength meter was calibrated using a Doppler-free, saturated absorption measurement in Rb vapor. The UV pulse energy and the ion current were measured for each laser pulse and stored together with the measured wavelength and the output from the detector (described in detail below). A thorough description of the data acquisition system can be found in the earlier paper by Andersson *et al.* [156]. In the analysis of the data, which was done offline, all the data was binned according to the measured photon energy of the UV radiation.

The high velocity of the unidirectional ions moving collinearly with respect to the laser beam causes a Doppler shift. A correction for this shift was made by calculating the ion velocity from the known acceleration voltage in the ion source. The uncertainty of the ion beam kinetic energy gave an error in the corrected photon energy of less than 20 μeV, which is on the order of the laser bandwidth. The calibration of the photon energy scale was confirmed by the observation of the known position of the sharp onset of the K(5 ^{2}F) threshold.

State selective detection of the K atoms in Rydberg states was achieved by using a combination of an electric field ionizer and a position sensitive detector. An inhomogeneous electric field was produced in the field ionizer, which consisted of two cylindrical electrodes placed 2 cm apart, as illustrated in Fig. 9.2. The electrodes were symmetrically biased with positive and negative voltages on the order of 4 kV. The field strength varied along the beam axis, having its maximum value between the two electrodes. Negative ions entering the field region were deflected into a Faraday cup. Rydberg atoms followed a straight path until the field strength was sufficient for field ionization to occur. Once ionized, the positive ions were deflected by the same field and finally detected with a position sensitive detector placed approximately 10 cm from the field ionizer. Atoms in different Rydberg states have different binding energies and were ionized at different positions along the path through the field ionizer. They therefore followed different trajectories and hit the position sensitive detector at different positions.

The position sensitive detector consists of a microchannel plate (MCP)

stack positioned in front of a pair of delay line anodes [1]. The active area of the detector has a diameter of 40 mm. Signals from the delay lines and the MCPs were amplified and converted to timing pulses by constant fraction discriminators. The timing pulses were digitized in a time-to-digital converter (TDC) with a 25 ps time resolution. The accumulated TDC data were used to calculate the position and time of arrival of positive ions at the detector. The velocity of the 6 keV K^- ions was approximately 0.17 m/μs. This gives a time of flight from the interaction region to the detector of between 1 and 4.5 μs.

A background of positive ions was caused by sequential two-electron detachment induced by the UV laser and by collisional double-detachment of negative ions with the residual gas in the interaction chamber. A pressure of 10^{-8} to 10^{-9} mbar in the interaction chamber minimized the collisional events, leaving the photo-induced background as the dominant one. These background ions were immediately deflected by the electric field when they entered the field ionizer. Therefore, they followed a different path compared to that of the positive ions created by field ionization of Rydberg atoms, which constituted the signal in the experiment. Signal and background ions were thus spatially well separated at the detector. However, the multi-hit dead-time of the detector limited the maximum count rate for which individual hits could be unambiguously identified. This problem was minimized by adjusting the voltage of the field ionizer electrodes such that background ions were directed outside the active area of the detector. The trajectories of the ions through the field ionizer are illustrated in Fig. 9.2.

A known problem in experiments utilizing UV radiation and MCP-based detectors, is that scattered light can potentially saturate the detectors. This problem was avoided by reducing the potential across the MCP stack during a time interval that covered the duration of the UV laser pulse. In the presence of the laser pulse the front of the MCP stack was biased at +800 V, while the back was at the operational +2.2 kV, giving a voltage over the MCP stack of 1.4 kV. After the UV pulse the front was set to ground potential, hence increasing the voltage across the MCP stack to the operational value of 2.2 kV. The switching time of the front voltage was approximately 0.5 μs. Hence, the MCP stack was inactive when the photons hit and active at the time when the particles produced in the interaction region arrived at the detector.

Ultraviolet photons also produced secondary particles as a result of reflections on windows and walls in the vacuum chamber. These par-

[1] Commercially available from RoentDek Handels GmbH

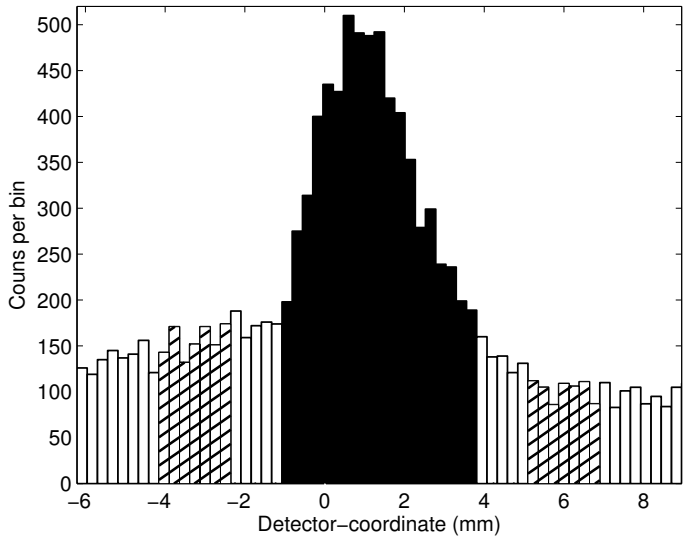

Figure 9.3: Two dimensional projection of the field-ionized Rydberg atoms in state $24\,^2D$ from measurement of the K(5 ^{2}F) channel. The selected signal region is shown in black. The hatched regions are used to estimate the background in the signal region.

ticles arrived at the detector over a time span of approximately 10 μs, which overlapped with the arrival times of the positive ions that constituted the signal. In addition, fast ions produced secondary particles when striking electrodes and walls of the vacuum chamber. Background originating from these two sources was spatially spread out and was slowly varying over the active area of the detector. The value of this contribution could therefore be estimated and subtracted from the signal. Figure 9.3 shows a cut across the detector through the distribution of detected particles. For each photon energy bin in the data analysis, the number of counts in the area of the detector containing the signal (marked black in the figure) was integrated. The background was determined as the mean count density around the signal region (hatched in the figure) and was subtracted accordingly. No further background subtraction was performed. The mean number of counts per laser shot was then normalized according to the average ion current and mean number of UV photons in the corresponding laser pulses. As can be seen in Fig. 9.3, the background was not completely flat. The shape of the background varied with experimental parameters and thus the subtraction worked better for some data sets than others.

Mechanical and optical instabilities in the OPOs caused small pulse-to-

pulse pointing instabilities in the laser beams. There might also have been a small drift of the UV beam direction as the wavelength was scanned. These effects were estimated to give uncertainties smaller than 10% within a measured cross section. Absolute measurements of cross sections are precluded, however, as a result of the unknown, and possibly changing, overlap of the ion and laser beams and the unknown efficiency of the detection system.

9.3 Results

Figure 9.4a shows the partial photodetachment cross section for the K(7 ^{2}S) channel from below the K(7 ^{2}S) threshold to just above the K(5 ^{2}F) channel opening. The region just below the K(5 ^{2}F) threshold is shown in Fig. 9.4b, where a second data set with higher point density is visible above 4.295 5 eV. The signal is essentially zero below threshold and rises sharply at the threshold energy. The large modulations in the cross section above threshold are due to the presence of resonances in this region. The shape of such modulations can be described by the Fano parameterization using the energy, E_r, the width, Γ, and an asymmetry parameter, q, [157] to model a resonance. An alternative, but equivalent, description of a resonance shape was given by Shore [158]. In the present work we extracted the resonance parameters by fitting the experimental data with an expression based on the Shore parameterization. The presence of resonant and non-resonant contributions was treated using the method presented by Liu and Starace [141]. The expression used in the fit includes a summation over multiple resonances and has the form

$$\sigma = (c + \hbar\omega\, d)\left(1 + \sum_i \frac{a_i\,\epsilon_i + b_i}{{\epsilon_i}^2 + 1}\right) \tag{9.6}$$

where i denotes the resonance index, $\hbar\omega$ is the photon energy, and $\epsilon_i = (\hbar\omega - E_{r,i})/\frac{\Gamma_i}{2}$ is a normalized energy parameter expressed in terms of the energy and the width of the *i*:th resonance. The shape of a single resonance is described by the Shore parameters a_i and b_i. The non-resonant cross section is represented by a linear function with coefficients c and d. The Fano shape parameter, q_i, was obtained from the best fit values of a_i and b_i, according to the method of McDonald and Crowe [159]. Strictly speaking, the formula presented in Eq. (9.6) is valid only for isolated resonances [157,158]. In the present experiment some of the resonances are overlapping. Resonance A, for example,

overlaps both resonances *B* and *D*. The width of *A* is, however, much larger than the widths of *B* and *D*. This means that the phase of the contribution from resonance *A* varies only a little over the other two resonances. Due to the small phase variation the resonances can be treated individually with the parameterization in Eq. (9.6). For resonances *B* and *D* only the wings are overlapping; since the magnitude of this overlap is small the resonances can as a good approximation be treated as isolated.

The solid curves shown in Figs. 9.4a and 9.4b represent the best fit of Eq. (9.6) to the data. Contributions from three resonances are considered in this fit. The energies and widths that were extracted for resonances *A*, *B* and *D* are presented in Table 9.1 and are marked in Fig. 9.4. Resonance *C* was not observed in the present experiment.

Cross sections for the K(7 ^{2}S), K(5 ^{2}F) and K(5 ^{2}G) photodetachment channels in the energy region 4.29–4.36 eV are shown in Fig. 9.5. This region encompasses the thresholds for the K(5 ^{2}F), K(5 ^{2}G) and K(7 ^{2}P) channel openings. Two resonances are observed in all three partial cross sections. A relatively broad resonance appears at approximately 4.324 eV and a much narrower one is seen at 4.353 eV, just below the K(7 ^{2}P) channel opening. Data sets with higher point density were used to resolve the structures around the narrow resonance. The threshold region for photodetachment to the K(5 ^{2}F) channel (see Fig. 9.5c) looks much like a step function. In the K(5 ^{2}G) channel (see Fig. 9.5d), in contrast, the photodetachment cross section is slowly increasing with energy above threshold. The signal below threshold in Fig. 9.5c is nonzero. This finite valued baseline indicates that the background subtraction described in section 9.2 is not completely successful in the K(5 ^{2}F) channel. In comparison, the baselines in Figs. 9.4a and 9.5d align better with the zero line.

The data of the K(7 ^{2}S) and K(5 ^{2}F) channels were fit using Eq. (9.6) involving two resonance contributions. In the K(5 ^{2}G) channel the slowly varying cross section in the threshold region extends over the whole region up to the K(7 ^{2}P) threshold. In this case, we replaced the linear part in Eq. (9.6), which represents the non-resonant cross section, with the threshold law from Eq. (9.2), yielding an expression

$$\sigma = \sigma_0 \, \exp\left[D \, (\hbar\omega - E_{5\,^2G})^{1/4}\right] \left(1 + \sum_i \frac{a_i \, \epsilon_i + b_i}{{\epsilon_i}^2 + 1}\right), \qquad (9.7)$$

where σ_0 is a normalization parameter and $E_{5\,^2G}$ is the threshold energy for the K(5 ^{2}G) channel. The values for the resonance energies

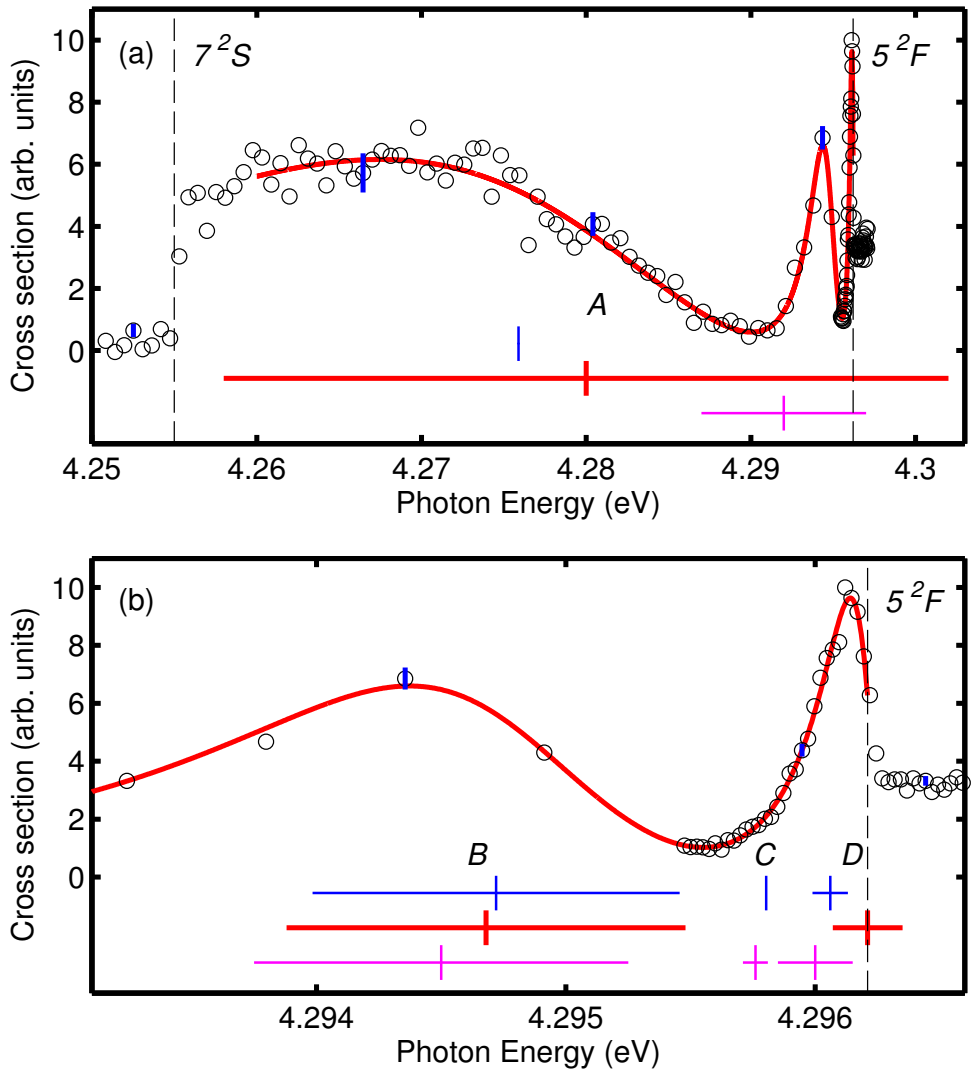

Figure 9.4: (Color online) Partial cross section for the K(7 ^{2}S) channel. Vertical dashed lines indicate threshold energies. Panel (a) shows the full energy region between the K(7 ^{2}S) and the K(5 ^{2}F) thresholds. Panel (b) shows a close-up of the region just below the K(5 ^{2}F) threshold. Error bars (blue online) indicating the one sigma statistical uncertainty are shown for a few representative data points. The solid curve (red online) is a fit of Eq. (9.6) with three resonances. Resonance energies are shown as short vertical lines, while the horizontal lines indicate the widths. The lowest lines (magenta online) represent the previous experimental results by Kiyan *et al.* [152], the middle lines (red online) represent the present data and the upper lines (blue online) are the theoretical values by Liu [135].

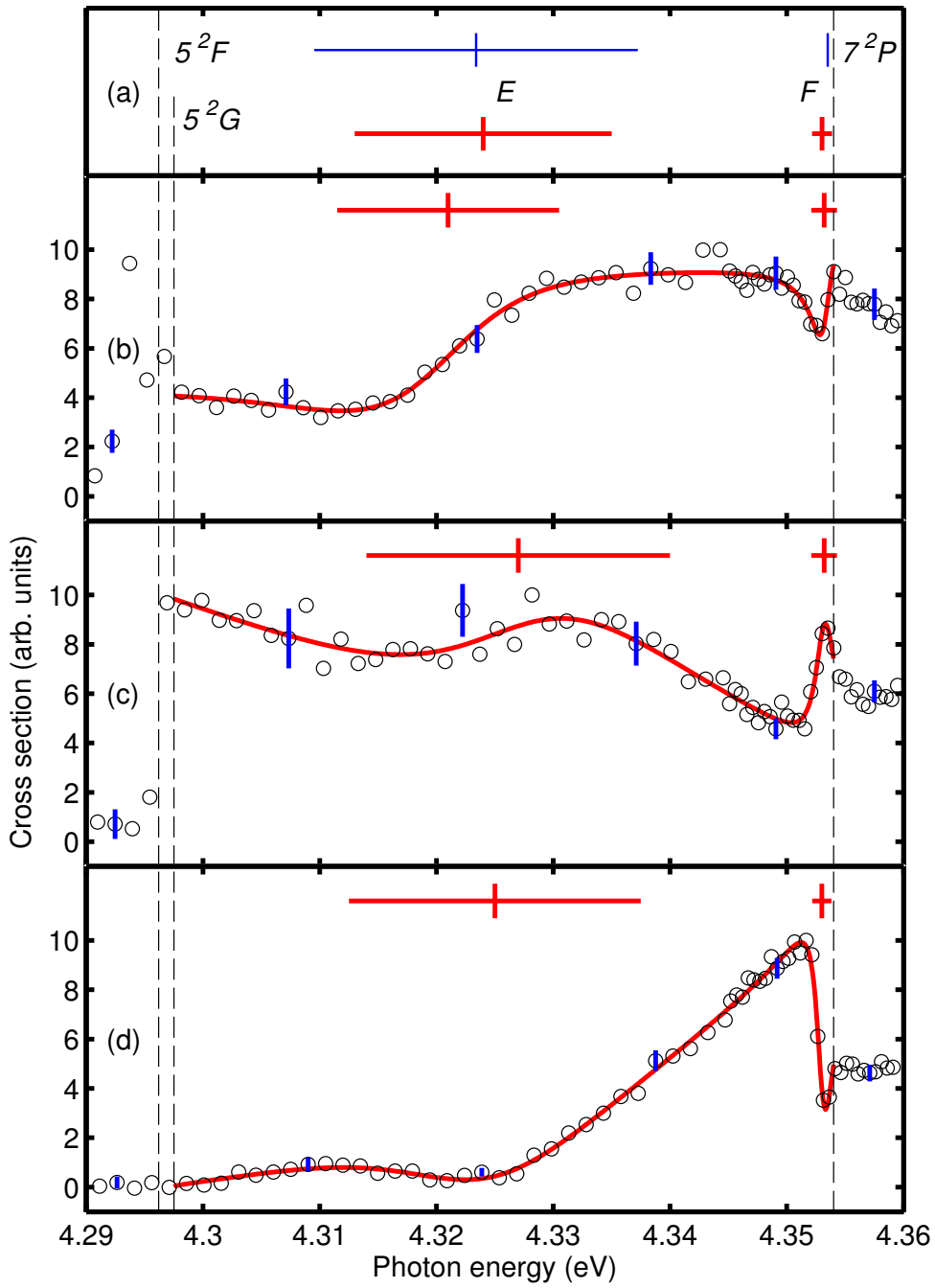

Figure 9.5: (Color online) Partial photodetachment cross sections for the K(7 ^{2}S), K(5 ^{2}F) and K(5 ^{2}G) channels, shown in panels (b), (c) and (d), respectively. Error bars (blue online) indicating the one sigma statistical uncertainty are shown for a few representative data points. Representative fits to the data are shown as solid curves (red online). Energies and widths of the resonances extracted from the three fits are indicated in the corresponding panels. Panel (a) shows the weighted mean of the resonance parameters (lower line, red online) as well as the values by Liu (upper line, blue online). Threshold energies are indicated by vertical dashed lines.

Table 9.1: *Resonance parameters extracted in the present experiment compared with previous results.*

Label	Channel / source	E_r (eV)	Γ (meV)	q
A	K(7 ^{2}S)	4.28(2)	44(20)	-1.4
	K(5 ^{2}S)[a]	4.292(2)	10(2)	
	Calculation[b]	4.275 90		
B	K(7 ^{2}S)	4.294 68(9)	1.6(3)	-2.8
	K(5 ^{2}S)[a]	4.2945(1)	1.5(2)	
	Calculation[b]	4.294 72	1.472 2	
C	K(7 ^{2}S)[c]			
	K(5 ^{2}S)[a]	4.295 76(4)	0.10 (8)	
	Calculation[b]	4.295 803 1	0.002	
D	K(7 ^{2}S)	4.296 21(5)	0.28 (5)	-2.1
	K(5 ^{2}S)[a]	4.2960(2)	0.30 (3)	
	Calculation[b]	4.296 06		
E	K(7 ^{2}S)	4.321(5)	19 (6)	0.5
	K(5 ^{2}F)	4.327(7)	26 (9)	1.1
	K(5 ^{2}G)	4.325(4)	25 (8)	0.031
	Mean[d]	4.324(3)	22 (5)	
	Calculation[b]	4.32339	27.718 3	
	K(7 ^{2}S)[e]	4.320(3)	25 (9)	
	K(5 ^{2}G)[e]	4.319(4)	27 (4)	
	Mean[e]	4.320(3)	27 (4)	
F	K(7 ^{2}S)	4.353 2(6)	2.2 (5)	0.23
	K(5 ^{2}F)	4.353 2(5)	2.2 (4)	8.7
	K(5 ^{2}G)	4.353 00(13)	1.66 (12)	-0.23
	Mean[d]	4.353 02(13)	1.72 (12)	
	Calculation[b]	4.353 50		

[a] Experimental work performed by Kiyan *et al.* [152].
[b] Calculation performed by Liu [135].
[c] Resonance not observed in present work.
[d] Weighted mean of the parameters from the three channels in the present measurement.
[e] Parameters determined with a slightly smaller data set in Ref. [153].

and widths extracted from these fits are also given in Table 9.1. Resonance *E* has previously been investigated in the K(7 ^{2}S) and K(5 ^{2}G) channels [153]; these parameters are also presented in Table 9.1. The values of the resonance parameters differ slightly between the previous and present study. Given the quoted uncertainties, however, the values are in agreement. The differences in the resonance parameters are due to differences in the fitting procedure, where, for example, resonance *F* is included in the fits in the present study. Moreover, the data in the present study were extended with the detailed data sets above 4.345 eV in Fig. 9.5, compared to [153]. For all resonance energies presented in Table 9.1, the 20 μeV uncertainty in the energy scale due to the Doppler shift was added in quadrature to the one-sigma uncertainty from the fit.

9.4 Discussion

The energy region between the K(7 ^{2}S) and K(5 ^{2}F) channel openings, as shown in Fig. 9.4, was previously investigated, both experimentally by Kiyan *et al.* [152] and theoretically by Liu [135]. Table 9.1 is a compilation of the energies and widths of the resonances determined in the present experiment and in previous studies. The cross section to the K(7 ^{2}S) channel below the K(5 ^{2}F) channel opening shows both similarities and differences with the previous two cross section determinations. First we observe that the relative magnitude of the modulations differ although the general shape of the cross sections are similar. In the present experiment we observe a 90% modulation in the K(7 ^{2}S) channel, whereas the K(5 ^2S) channel investigated by Kiyan *et al.* exhibited a modulation of 25%. The larger modulation indicates that the reaction pathways via the doubly excited states are relatively more important in the K(7 ^{2}S) channel than in the K(5 ^2S) channel. This is an advantage if the increased relative modulation does not come at the cost of reduced overall signal level. A number of absolute partial cross sections for photodetachment of K^- have been calculated in [135]. These show a general trend that modulations due to resonances decrease slower than the level of the non-resonant cross sections for higher lying final state channels. Second, a very narrow resonance, labeled *C* in Table 9.1 and Fig. 9.4, was observed by both Kiyan *et al.* and Liu, but it is not visible in the present data. Apparently, the branching ratio into the K(7 ^{2}S) channel was insufficient to produce a significant modulation in the present experiment. Third, the width of resonance *A* is more

than four times greater than the width determined by Kiyan *et al.* As a consequence, the uncertainty in the resonance energy is also larger in the current experiment. This increased uncertainty is not caused by lower statistical quality of the data, but is rather a consequence of the broader structure that is observed in the K(7 ^{2}S) channel. It is obvious from the previous calculation [135] and experiment [152] and the present data that it is difficult to make a conclusive determination of the resonance parameters for resonance A. An experimental investigation of additional photodetachment channels would be needed in order to make a definite assignment of the energy and width of the associated doubly excited state.

There are two resonances present in all the three channels in the region between K(5 ^{2}F) and K(7 ^{2}P) thresholds (see Fig. 9.5). It is interesting that the general shapes of the cross section curves in the three channels are very different, although the observed resonances are due to the same two doubly excited states. The energies and widths of the resonances should be the same in all three channels. Variations in shape are caused by different phase shifts in the interference in the different channels, which is described by the line shape parameters a_i and b_i (or q_i). The resonance positions are not obvious from inspection of the individual partial cross sections. Nevertheless, the fittings in each of the three channels produced very similar resonance parameters. The measured parameters were also in good agreement with the energies and widths calculated by Liu [135]. These results clearly show the advantage of detecting the same resonance in more than one channel. This is particularly important in cases where resonances partially overlap each other.

9.5 Conclusions

We have developed an apparatus which enables the study of partial photodetachment cross sections to highly excited states of the residual atom, even when the cross sections are very small. The apparatus was used in the study of the K(7 ^{2}S), K(5 ^{2}F) and K(5 ^{2}G) final state detachment channels in the potassium negative ion. We have shown that it is an advantage to observe a resonance structure in more than one channel, as was illustrated for the resonances below the K(7 ^{2}P) threshold. The presented experimental technique, where an IR laser is used for the resonance ionization, enables the detection of highly excited final states. This gives the possibility to select the most favorable

of an increased number of channels. The best possible signal level and modulation of the cross section as well as noise and background levels can thus be achieved. This, in turn, leads to more reliable determinations of resonance parameters. The ability to detect residual atoms in highly excited states has another advantage: It allows one to study the effect of high dipole polarizability on threshold behavior.

In the present experiment, parameters have been determined for two previously unobserved resonances between the K(5 ^{2}G) and K(7 ^{2}P) thresholds. The results are in good agreement with the previously calculated values by Liu [135]. This study, together with a recent Letter [153], constitutes the first step in an intended series of measurements with the aim of investigating photodetachment at an increasing degree of excitation. Our long term goal is to access channels where the residual atom states are approaching the double detachment limit.

Financial support from the Swedish Research Council is gratefully acknowledged. C.W.W. received support from the Wenner-Gren Foundation, the Andrew W. Mellon Foundation, and NSF Grant Nos. 757976 and 1068308. H.H. and I.Yu.K. acknowledge the support by the Deutsche Forschungsgemeinschaft, Grant No. KI 865/3-1.

CHAPTER 10

Observation of overlapping resonances below the 10 $^2P_{1/2,3/2}$ states in photodetachment of Cs^-

A. O. Lindahl[1], J. Rohlén[1], H. Hultgren[1,2], D. J. Pegg[3], C. W. Walter[4] and D. Hanstorp[1].

[1]*Department of Physics, University of Gothenburg, 412 96 Gothenburg, Sweden.*

[2]*Albert-Ludwigs-Universität, D-79104 Freiburg, Germany.*

[3]*Department of Physics, University of Tennessee, Knoxville, TN 37996, USA.*

[4]*Department of Physics and Astronomy, Denison University, Granville, Ohio 43023, USA.*

A collinear beams apparatus has been used to study photodetachment of Cs^-. Partial cross sections were measured using state selective detection based on a resonance ionisation scheme. Several resonances were observed in the Cs(10 ^2S), Cs(6 ^2F) and Cs(6 ^2G) final state channels, below the Cs(10 $^2P_{1/2,3/2}$) channel openings. The observed resonances were strongly overlapping. A simple model was developed to account for the interference of multiple resonances. The model is essentially a generalization of the Fano and Shore parametrizations for single resonances. It is based on a description of the system in which the only interaction between the resonant and continuum states is the interference created through addition of amplitudes. A tentative identification and assignment of resonance parameters was performed. However, a calculation involving both relativistic and many-body effects will be needed in order to establish the identity and understand the origin of the observed structures. In addition, the cross section behaviour just above the thresholds was investigated. The resonances observed in the region prevented a detailed analysis of the threshold behaviour, but some general observations could be made. The opening of the Cs(10 ^2S) and Cs(6 ^2F) channels, where the polarization of the atomic state is large and positive, showed a very rapid onset.

In the case of Cs(6 ^2G) channel, on the other hand, where the atomic state is expected to have a large a negative polarization, the photodetachment cross section increased very slowly with energy. This is in qualitative agreement with a recent study on threshold behaviour [153].

10.1 Introduction

The structure and dynamics of negative ions are of considerable interest in the field of atomic physics. In the case of a positive ion or an atom, the interaction of the outermost electron with the core is described by the Coulomb potential at large distances. The $1/r$ scaling of the potential gives rise to an infinite series of bound states commonly known as Rydberg states. However, in a negative ion the asymptotic interaction is described by an induced dipole potential. The induced dipole interaction has a very short range, which results in a potential that has a finite number of states. In most cases there is only one bound state in a negative ion and the binding energy is usually an order of magnitude smaller than that in the isoelectronic atom. Since the binding of the outermost electron in a negative ion is relatively weak, electron-electron correlations play a much more important role than they do in positive ions and atoms. The major influence of the electron-electron correlation require advanced many-body calculations to fully describe the structure and dynamics of a negative ion. Thus, valuable insight into electron-electron correlation can be gained by comparing atomic many-body calculations with experimental observations. Development of powerful computers, during the last couple of years, have made more complex negative ions such as Cs^- generally accessible for theoretical investigations.

There is a general lack of bound excited states in negative ions. Above the first detachment limit, however, there exists a rich spectrum of doubly excited states. These states can be viewed as a negative ion formed by the attachment of an electron to an atom in an excited state. Electron-electron correlation is even more important for these states. The most fundamental examples of doubly excited states are in the H^- ion. Several studies, both theoretical and experimental, have been performed on this system. [144–148]. While H^- is a pure two-electron system, negative ions of the alkali metals can be considered to be effective two-electron systems in the sense that two active electrons move in the field of a closed, frozen core. Doubly excited states lying just below the double detachment limit will be less influenced by effects caused

by polarization and penetration of the core. In this case, the representation of the doubly excited states by an effective two-electron model makes a very good approximation. Previous experimental studies in this field have been performed on Li^- [149, 150], Na^- [151] and K^- [152, 167].

The threshold region for the photodetachment process is of fundamental interest. In this energy region the photodetachment cross section is sensitive to the interaction between the detached electron and the residual atom. Wigner [23] describes the threshold behaviour as being determined by the interaction having the longest range. In the case of negative ions this is the effective centrifugal potential, and the resulting energy dependence of the cross section is

$$\sigma \propto E^{\ell+1/2}. \tag{10.1}$$

Here, E and ℓ represent the energy and orbital angular momentum of the detached electron. This simple model can adequately describe the cross section just above the threshold. Additional terms must be taken into account when the energy of the detached electron is higher. O'Malley has developed a model taking the polarizability of the residual atom into account [132], while the correction factor of Farley describes the effect of the finite size of the initial state wavefunction [131]. Sandström *et al.* experimentally investigated the effect of large positive polarizabilities on the threshold behaviour for several final state channels leaving the residual alkali atom in an excited states [134]. All the observed thresholds exhibited a considerable more rapid onset than predicted by the Wigner law. The observed behaviour was, however, in good agreement with the predictions of a modified effective range model developed by Watanabe and Greene [133]. In a recent study it was shown, for the first time, that a negative polarizability has an opposite effect on the photodetachment cross section above the threshold [153]. The purely repulsive potential results in a very slow onset of the photodetachment cross section above threshold. The behaviour was qualitatively described using a semi-classical model [153], which resulted in an exponential energy dependence for the cross section

$$\sigma \propto \exp\left[D\,E^{1/4}\right]. \tag{10.2}$$

Polarizabilities of excited states in cesium have been determined experimentally, for example, by Antypas and Elliott [160] and theoretically by van Wijngaarden and Li [161]. The 6 ^2F state of Cs has a polarizability of 7.77×10^6 a.u. [161], which is in the same order of magnitude as the $5\,^2F$ state in K, investigated recently by Lindahl *et*

al. [153]. There are no calculations of the polarizability of the 6 ^2G state in Cs, but it can be expected to be of the same magnitude but opposite sign as the polarizability of the 6 ^2F state. This was the case in the study of the $5\,^2F$ and $5\,^2G$ states in K reported by Lindahl *et al.*

For a long time it was thought that the Cs^- ion might be the only atomic negative ion to have a bound state with opposite parity to the ground state. Sheer *et al.* [162] proved this not to be the case when they observed the $Cs^-(6s6p\ ^3P)$ state, situated above single detachment threshold. Prior to this observation, extensive theoretical work had been done on predicting the energy of the ^3P states [163, 164]. So far, Cs^- photodetachment has been investigated up to 1.96 eV [165]. The upper limit of this photon energy range allows for an investigation of the photodetachment of Cs^- via a final state channel that leaves the residual Cs atom in the first excited state. A Feshbach resonance situated just below the $Cs(6\,^2P_{1/2})$ state suppresses the non-resonant photodetachment cross section by two orders of magnitude [164, 165]. This observation was utilized in a excess-photon detachment study by Stapelfeldt and Haugen [166].

In the present paper we report on measurements of partial cross sections for photodetachment from Cs^- to the final channels involving the 10 ^2S, 6 ^2F and 6 ^2G states of the residual atom. One of the goals of the experiment was to observe and verify the threshold behavior described in [153] in a second system. The photodetachment channels were selected because of their similarity to the $K(5\,^2F)$ and $K(5\,^2G)$ channels in K^- photodetachment. An other objective of the experiment was to investigate possible resonance structures in the energy region below the opening of the 10 ^2P state. Such structures are a manifestation of double excited states of Cs^- that decay via autodetachment. The polarizability of 10 $^2P_{1/2}$ state has been calculated to be 3.49×10^6 a.u. The attractive polarization potential resulting from such a large polarizability is expected to support several doubly excited states. The experiment was performed at GUNILLA (Göteborg University Negative Ion Laser LAboratory), where a resonance ionisation scheme was utilized in order to isolate the specific detachment channels in order to measure their partial cross sections.

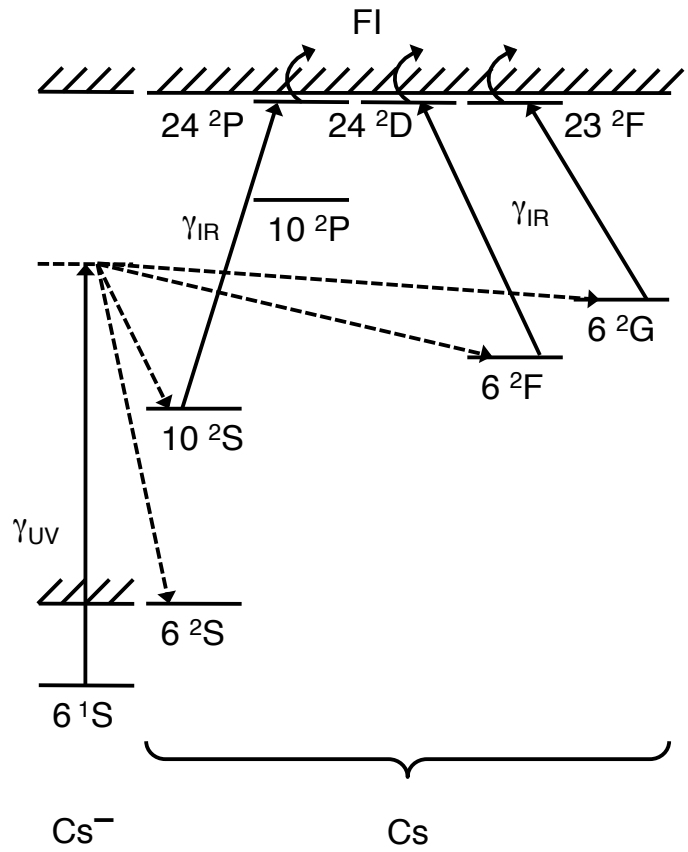

Figure 10.1: Partial energy level diagram (not to scale) of the Cs^- and Cs systems. A Cs^- ion absorbs a UV photon (γ_{UV}) and is promoted to a doubly excited state (dashed energy levels), which decay via autodetachment (dashed arrows). State selectivity in the detection is achieved by resonant excitation using an IR photon (γ_{IR}) followed by field ionization (FI).

10.2 Experiment

10.2.1 Procedure

Figure 10.1 shows the optical excitation scheme used in the present experiment. Cs^- ions were photodetached by UV photons with energies ranging from 3.977 to 4.043 eV. This is substantially larger than the electron affinity of Cs (0.471 626(25) eV [140]), and close to the energy needed for double detachment (4.365 531(25) eV [140, 168]). The residual atoms are thus left in a distribution of final states. A state selective detection scheme, based on resonance ionisation, was used to measure

the partial cross sections to specific excited states of the Cs atom. The selectivity was achieved by first resonantly exciting the residual atoms to highly excited Rydberg states and then ionizing the latter in an electric field. Infrared radiation was used in the resonance transition. The field ionization of the Rydberg atoms of interest enabled separation of the resulting positive ions from neutral atoms created by photodetachment to other excited states. In the present experiment the following photodetachment channels were investigated:

$$\mathrm{Cs}^-(6\,^1S) + \gamma_{\mathrm{UV}} \rightarrow \mathrm{Cs}(10\,^2S) + e^-, \tag{10.3}$$

$$\rightarrow \mathrm{Cs}(6\,^2F) + e^-, \tag{10.4}$$

$$\rightarrow \mathrm{Cs}(6\,^2G) + e^-. \tag{10.5}$$

The three channels have threshold energies of 3.980 407(25) eV, 3.984 025(25) eV and 3.986 881(25) eV, respectively [140, 168]. In the cases of the 6 ^2F and 6 ^2G states, the fine structure splittings are 13 μeV and 0.2 μeV, respectively, which was below the resolution of the experiment. The uncertainties in these values arise primarily from the uncertainty quoted on the measured electron affinity [140]. The energy range used in this study includes the openings of the three aforementioned channels, as well as the opening of the Cs(10 $^2P_{1/2}$) channel at 4.033 296(25) eV and the Cs(10 $^2P_{3/2}$) channel at 4.036 627(25) eV.

10.2.2 Apparatus

Photodetachment of Cs^- was studied using the collinear beams apparatus at GUNILLA. A large interaction volume defined by the overlap of collinearly superimposed ion and laser beams provided a highly sensitive measurement system. This was crucial since the partial photodetachment cross sections to highly excited state are generally very small, as shown in for example Ref. [135]. Moreover, the energy separations of adjacent excited states of the residual Cs atom are very small at high levels of excitation, which necessitates high energy resolution in the final state detection process. The state selective detection of these atoms via resonance ionization was the basis for the selectivity. The energy resolution in the experiment was enhanced by the large reduction in kinematic broadening brought about by the collinear interaction of the ion and laser beams [155]. In the present measurement, the energy resolution was determined primarily by the finite bandwidth of the laser used for photodetachment, which is approximately 25 μeV.

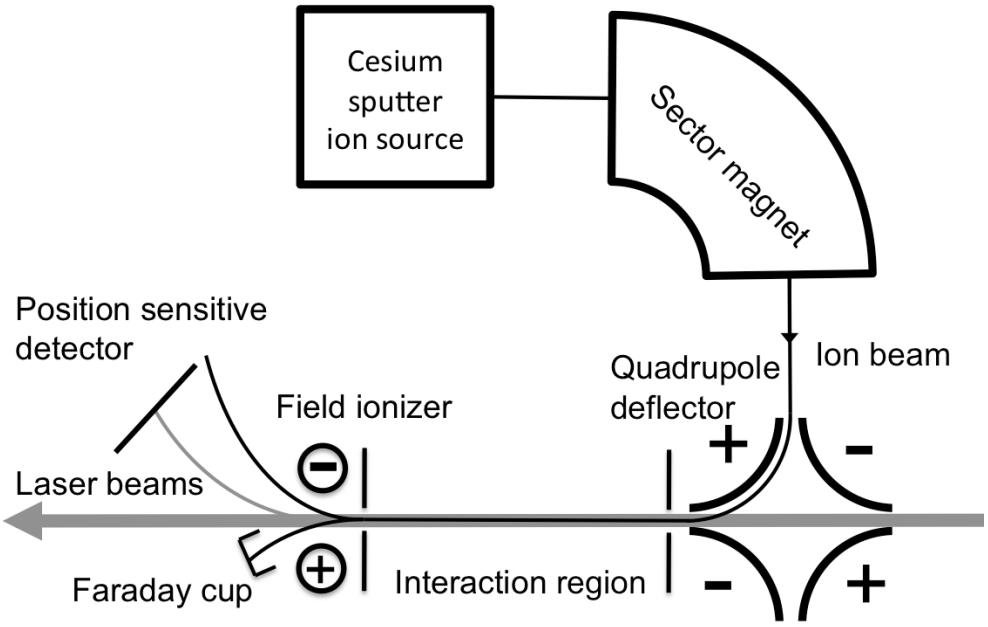

Figure 10.2: A schematic of the collinear beams apparatus. Two laser beams and an ion beam are superimposed in a collinear co-propagating geometry.

A schematic overview of the apparatus is shown in Fig. 10.2. The experimental arrangement has been described in detail in a recent publication [167]. Negative ions of cesium were produced in a cesium sputter ion source using a pre-drilled, but empty, aluminium cathode. The Cs^- ions were accelerated to 6 keV energy. The ion beam was mass selected in a magnetic sector before it was guided by an electrostatic quadrupole deflector into an interaction region defined by two 3 mm apertures placed 61 cm apart. The ion optical design of the apparatus is described in detail by Diehl *et al.* [138]. The interaction region is shielded against stray electric fields by means of a stainless steel tube centered along the path of the ions. In the interaction region, the ion beam was merged with two co-propagating laser beams, where one was used for photodetachment and the other for resonant excitation in the detection process. After the interaction region, an inhomogeneous electric field and a position sensitive detector (PSD) served as a Rydberg state analyzer. Rydberg atoms in different states were field ionized at different positions in the field so that the resulting positive ions were deflected at different angles into the detector. Information about the position where the ions hit the PSD were used to distinguish positive ions produced by field-ionization of Rydberg atoms from those created in sequential photodetachment-photoionization events induced by two UV photons.

The UV and the IR radiation were both generated by Nd:YAG-pumped OPOs delivering nanosecond pulses at repetition rates of 10 Hz. The spectral bandwidths of the lasers were 25 μeV. The pulse energy of the IR laser after the chamber was approximately 0.2 mJ, which was sufficient to saturate the resonant transitions to the Rydberg states. The UV pulse energy was approximately 0.7 mJ, far from saturating the non-resonant photodetachment process. In order to investigate the cross sections, the UV radiation was tuned from 3.977 to 4.043 eV in the ion rest frame. For the various channel studies, the IR laser was tuned to the resonant transitions $10\,^2S \rightarrow 24\,^2P$, $6\,^2F \rightarrow 24\,^2D$ or $6\,^2G \rightarrow 23\,^2F$, which, in the rest frame, correspond to 352.963, 352.552 and 346.775 meV, respectively [168]. The UV pulse arrived at the interaction region approximately 20 ns before the IR pulse. The negative ion beam was deflected into a Faraday cup by the electric field in the Rydberg analyzer. The ion current, after the passage through the interaction region, was on the order of 1 nA. For each shot of the two lasers, the data from the PSD was recorded together with the measured wavelength, the pulse energy of the UV radiation, and the ion current. The data analysis was performed using an off-line procedure. The data was binned according to the measured photon energy of the UV radiation. Each bin corresponds to a data point in the cross section curve. An estimation of the diffuse backgrounds observed in the experiment was performed by calculating the mean count density around the signal peak. The number of counts in the signal peak were then integrated and the background was subtracted. The number of counts was normalized with respect to the ion current, the pulse energy of the UV laser, and the number of laser shots in the bin. The measured laboratory-frame photon energies were converted to energies in the ion rest frame by use of the known kinetic energy of the ion beam. This Doppler shift correction introduced an uncertainty in the photon energy being less than 10 μeV, which is about half of the laser bandwidth.

10.2.3 Analysis of overlapping resonances

Figure 10.1 shows the optical excitation scheme employed in this work. A ground state Cs^- ion is excited by a UV photon to a doubly excited state. This state decays rapidly to a free electron and a neutral atom, which can be in the ground state or in an excited state. Alternatively, the same photon can detach an electron by making a direct transition to a continuum state of the same energy. The quantum interference between these resonant and non-resonant processes determines the mod-

ulation of the cross section. The phase difference between the amplitudes for the two paths determines whether the intereference is constructive or destructive. Experimentally, this is seen as a modulation of the non-resonant cross section by the presence of resonance associated with the doubly excited state. Fano [157] derived an analytical expression that describes the variation in the shape of a cross section in the presence of resonance structure. Later, Shore [158] deduced a different expression, which is an alternative parameterisation of the same shape described by the Fano profile. These parameterizations are only valid for single isolated resonances. In the present experiment it is evident that the existence of multiple overlapping resonances are needed to explain the measured cross sections. The initial and final states of the photodetachment reactions are connected via several independent paths associated with different doubly excited states. A simple model has been developed in order to account for overlapping of multiple resonances. The model is essentially a generalization of the Fano and Shore parametrizations for single resonances. It is based on a description of the system in which the only interaction between the resonant states and the continuum is the interference arising from the addition of amplitudes. This corresponds to the simplest possible view of interfering resonances. Effects that change the energies and widths of the resonances due to the direct interactions between the resonant states or the indirect interactions via the continuum couplings are ignored. A rigorous treatment of two interfering resonances in the presence of one open continuum can, for example, be found in [169].

The model is based on the presence of an arbitrary number of N doubly excited states, $\mathrm{Cs}^{-(k)}$, enumerated by $k = 1, 2, 3, ..., N$, in the single detachment continuum. For each photodetachment channel, Cs(nl), the reaction can proceed through multiple paths. The direct path is given by $\mathrm{Cs}^- + \gamma_{\mathrm{UV}} \rightarrow \mathrm{Cs}(nl) + e^-$ and is assigned an amplitude A_{nl}. The amplitude is given by the cross section for the non-resonant photodetachment process as $A_{nl} \propto \sqrt{\sigma_{nl}}$. The additional paths are given by the reactions that proceed via the resonant states $\mathrm{Cs}^- + \gamma_{\mathrm{UV}} \rightarrow \mathrm{Cs}^{-(k)} \rightarrow \mathrm{Cs}(nl) + e^-$. Each such path is assigned an amplitude A_k^{nl}, to which two different factors contribute. The first factor comes from the excitation of the negative ion to the $\mathrm{Cs}^{-(k)}$ state. The excitation probability to a state with energy E_k and a width Γ_k has a Lorentzian energy dependence

$$L_k \propto \frac{1}{\sqrt{{\epsilon_k}^2 + 1}}, \tag{10.6}$$

where the dimensionless detuning is given as $\epsilon_k = (\hbar\omega - E_k)/\frac{\Gamma_k}{2}$, with $\hbar\omega$ as the photon energy. The second factor of A_k^{nl} is the rela-

tive branching, B_k^{nl}, of the decay of $Cs^{-(k)}$ into the many Cs(nl) states. We now assume that the energy dependence of decay from $Cs^{-(k)}$ to Cs(nl) is identical to the energy dependence of the non-resonant photodetachment amplitude from Cs^- to Cs(nl), e.i., $B_{nl}^k \propto A_{nl}$. With this assumption, for the otherwise unknown energy dependence of B_{nl}^k, a well known result can be obtained for a single resonances (see below).

So far, only the energy dependencies of L_k and B_k^{nl} have been considered. The absolute magnitudes of the cross section for excitation and the amount of branching to the Cs(nl) state are instead collected in the parameter s_k^{nl}, which describes the relative amplitude of the paths via the resonant states. With these parameters the amplitude via the state $Cs^{-(k)}$ in to the final state Cs(nl) is given by

$$A_k^{nl} = s_k^{nl}\, L_k\, B_k^{nl} = \frac{s_k^{nl}\, A_{nl}}{\sqrt{{\epsilon_k}^2 + 1}}. \tag{10.7}$$

The amplitudes for the different paths can now be added since the relative phases are known. Each resonant path has an intrinsic phase shift, δ_k^{nl}, compared to the direct path. Further, the excitation to the $Cs^{-(k)}$ state introduces an energy dependent phase shift of $\delta_k = \arctan(-1/\epsilon_k)$ [169]. The total amplitude for photodetachment, including the non-resonant cross section and the resonances is thus given by

$$A_T^{nl} = A_{nl} + \sum_{k=1}^{N} A_k^{nl} \exp\left[i\left(\delta_k^{nl} + \delta_k\right)\right], \tag{10.8}$$

and from this expression the cross section is give by $\sigma_T^{nl} \propto |A_T^{nl}|^2$.

A description of overlapping resonances should, of course, reproduce the established expressions for a single isolated resonance. Therefore, the sum in Eq. (10.8) is evaluated with $N = 1$. For a single resonance, the calculation of σ_T^{nl} can be performed analytically and results in

$$\sigma_T^{nl} \propto {A_{nl}}^2 \left(1 + \frac{-\epsilon\, 2\, s^{nl}\, \cos(\delta^{nl}) + (s^{nl})^2 - 2\, s^{nl}\, \sin(\delta^{nl})}{\epsilon^2 + 1}\right), \tag{10.9}$$

where the index $k = 1$ has been dropped. By substituting $a = -2\, s^{nl}\, \cos(\delta^{nl})$ and $b = (s^{nl})^2 - 2\, s^{nl}\, \sin(\delta^{nl})$ into Eq. (10.9) the well known expression

$$\sigma_T^{nl} \propto {A_{nl}}^2 \left(1 + \frac{\epsilon\, a + b}{\epsilon^2 + 1}\right) \tag{10.10}$$

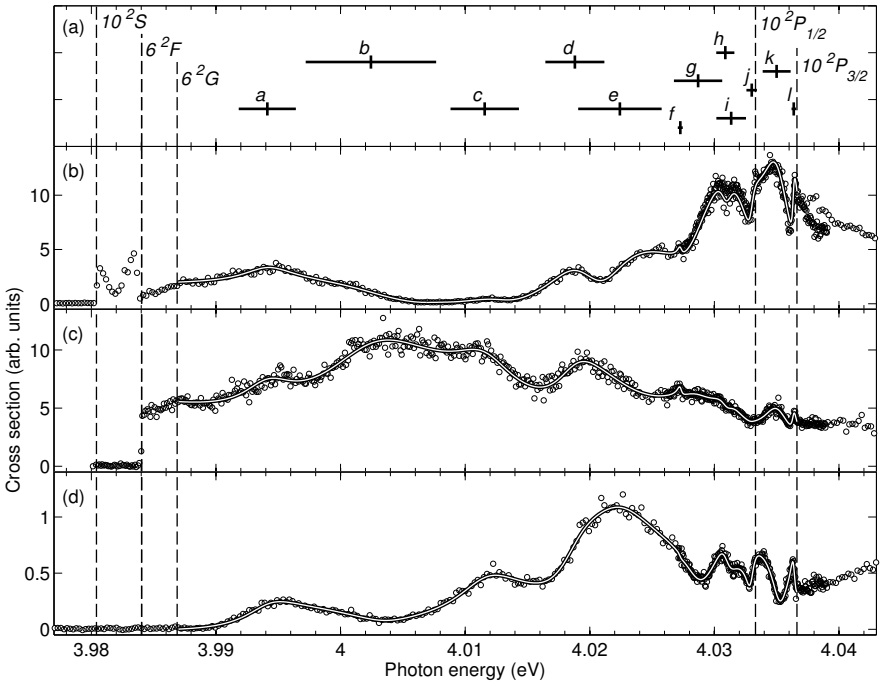

Figure 10.3: Partial cross section in the 10 ^2S, 6 ^2F and 6 ^2G channels in panels (b), (c) and (d), respectively. Dashed vertical lines mark threshold energies. Resonance energies and widths extracted from the fit discussed in section 10.4 are shown in panel (a).

is obtained, which for example was used in [141]. The expression in Eq. (10.9) thus represents an alternative parametrization with the same result as the Shore [158] and Fano [157] profiles. Here the s^{nl} parameter corresponds to the relative amplitude of the path via the resonance compared to the direct path when $\epsilon = 0$, i.e. at resonance. The angle δ^{nl} can be interpreted as the phase shift acquired by the wavefunction due to the finite lifetime of the doubly excited state.

A simple analytical form cannot be obtained for more than one resonance. It is, however, straight forward to implement the calculation of σ_T^{nl} numerically by explicitly evaluating the terms of the sum in Eq. (10.8). The numerical expression can then be fitted to experimental cross sections using a standard fitting routine.

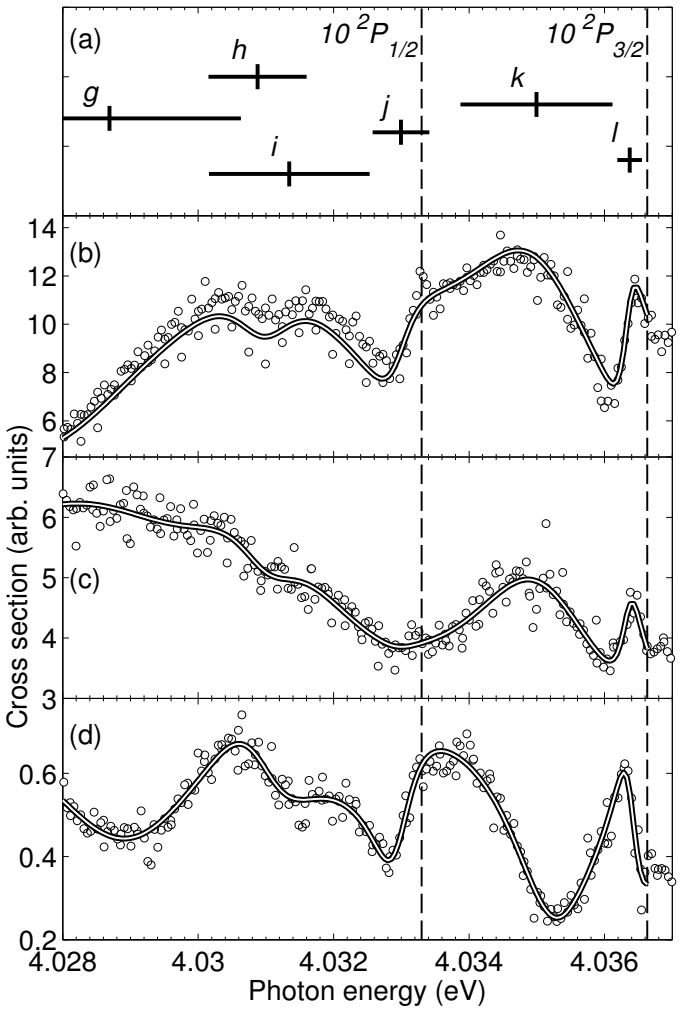

Figure 10.4: Detailed view of the region of the Cs(10 $^2P_{1/2,3/2}$) channel openings from Fig. 10.3.

10.3 Results

Partial photodetachment cross sections for the Cs(10 ^2S), Cs(6 ^2F) and Cs(6 ^2G) channels are shown in Figs. 10.3b, 10.3c and 10.3d, respectively. Two data sets are shown for each channel. One set extends over the whole range (3.978–4.040 eV) and has a bin size of 2 cm^{-1} (≈ 248 μeV). The second set was designed to capture the rapid cross section modulations in the region encompassing the Cs(10 $^2P_{1/2,3/2}$) channel openings (4.027–4.039 eV). It has a bin size of 0.4 cm^{-1} (≈ 49.6 μeV). This region is shown in greater detail in Fig. 10.4. The threshold region of the Cs(10 ^2S) channel exhibits some rapid cross section modulations,

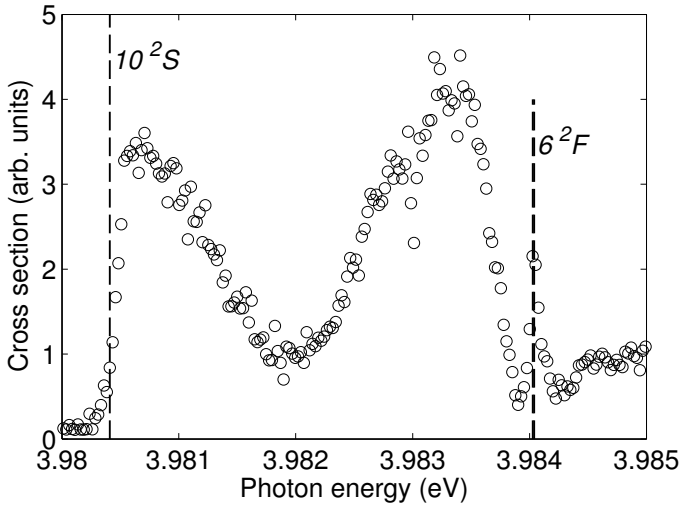

Figure 10.5: Partial cross section in the Cs(10 ^2S) channel. Dashed vertical lines mark the threshold energies. Bin size is 0.2 cm^{-1}.

which are shown in detail in Fig. 10.4. This figure shows the cross section from threshold to above the Cs(6 ^2F) channel opening (3.98–3.983 eV), with a bin size of 0.2 cm^{-1} ($\approx$ 24.8 μeV). In this case, the cross section is seen to rise sharply at threshold. It is then strongly modulated before it is reduced by 85% over a range of 0.5 meV, just below the opening of the Cs(6 ^2F) channel. The cross section then increases slowly up to an energy of 3.994 eV. Right at the opening of the Cs(6 ^2F) channel, a very narrow structure is observed. The threshold for the Cs(6 ^2F) channel (Fig. 10.3c) has a very sharp onset, while the cross section for the Cs(6 ^2G) channel (Fig. 10.3d) is rising much more slowly above threshold. All three partial cross sections show large modulations, indicating the presence of a number of resonances.

The large modulations of the cross section in the Cs(10 ^2S) channel below the Cs(6 ^2F) channels opening (Fig. 10.5) cannot be reproduced by any reasonable combinations of resonances and curves representing the non-resonant cross section. The resonance structures in Fig. 10.3 show a number of overlapping resonances. This means that there is no unambiguous method to extract resonance parameters from the data.

10.4 Discussion

The cross sections just above the thresholds in the Cs(10 ^2S) and Cs(6 ^2F) channels are steeply rising (Figs. 10.5 and 10.3c). This is in good agreement with previously measured photodetachment channels in which the residual atoms state has a large positive polarizability [134, 153]. The calculated polarizabilities of the 10 ^2S and 6 ^2F states are indeed very high, 4.75×10^5 a.u. and 7.77×10^6 a.u. respectively [161]. The polarizability of the Cs(6 ^2G) state is unknown. However, it is expected to be of similar size but opposite sign as compared with the closely spaced Cs(6 ^2F) state. The onset of the Cs(6 ^2G) channel, in contrast to the Cs(10 ^2S) and Cs(6 ^2F) channels, show a very slow onset of the cross section. This agrees well qualitatively with the threshold behaviour observed in photodetachment into the K($5\,^2G$) state in K.

The shape of the Cs(10 ^2S) cross section shows very large modulations in the 4 meV region between its threshold and the opening of the C(6 ^2F) channel (see Fig. 10.5). We have so far been unable to model the observed cross section using different functional forms of the non-resonant cross section and different numbers of resonances. A single Shore profile can, however, be fitted to the sharp structure at the Cs(6 ^2F) channel opening. This resulted in an energy of 3.984 040(11) eV and a width of 95(11) μeV. The main contribution to the uncertainty in the position arises from the uncertainty in the Doppler shift correction. It has not been possible to determine if the measured energy of the resonance is below or above the threshold of the Cs(6 ^2F) channel, which is given as 3.984 025(25) eV in the literature [140, 168]. The most likely origin of this structure is, however, a doubly excited state of Cs^- that is bound with respect to the parent Cs(6 ^2F) state.

In the region between the openings of the Cs(6 ^2G) and Cs(10 $^2P_{3/2}$) channels, modulations are seen that must be associated with the presences of many different resonances. Only a few of the structures can easily be identified in more than one partial cross section. Just below the Cs(10 $^2P_{3/2}$) channel opening, for example, a large and narrow modulation is observed in all three channels. Below the Cs(10 $^2P_{1/2}$) channel opening, an equally narrow structure is observed in both the 10 ^2S and the 6 ^2G channels. These two structures are most likely the result of two doubly excited states bound with respect to the 10 $^2P_{1/2}$ and 10 $^2P_{3/2}$ states, respectively.

The data shown in Fig. 10.3 clearly contains a number of overlapping resonances. Therefore, the numerical model described in section 10.2.3

were fitted to the data. Linear functions were used to describe the non-resonant cross sections in the Cs(10 ^2S) and Cs(6 ^2F) channels. In the Cs(6 ^2G) channel, on the other hand, the threshold model in Eq. (10.2) was used for this purpose. The model from [153] is expected to be a better description of the non-resonant cross section than a linear function in this case due to the expected large and negative polarizability. Fits with different number of resonances were attempted. The region seems to encompass at least 11 different overlapping resonance structures. All of these resonances are, however, not visible in all three channels due to different branching of the resonant states to the final states. Attempts to fit an expression with 11 resonances to the cross section in a single channel resulted in unstable fitting conditions. To solve this, the fits were performed in the three channels at the same time. The energy, E_k, and width, Γ_k, of each resonance was constrained to have the same value in all three channels, while the relative amplitude, s_k^{nl}, and the phase shift, δ_k^{nl}, were allowed to vary. The result of such a fit are shown as hollow lines in Figs. 10.3 and 10.4. The extracted resonance parameters are indicated in panel (a) of these figures and are tabulated in Table 10.1.

Table 10.1: Tentative assignment of resonance parameters between the Cs(6 ^2G) and Cs(10 $^2P_{3/2}$) channel openings. Uncertainties represent one sigma confidence interval in the fit.

label	E_r (eV)	Γ (meV)	label	E_r (eV)	Γ (meV)
a	3.093 6(4)	6.3(7)	*g*	4.027 6(18)	6.0(40)
b	4.003 2(6)	11.0(12)	*h*	4.029 89(22)	1.9(5)
c	4.012 9(6)	6.8(12)	*i*	4.032 96(5)	0.61(9)
d	4.019 6(5)	4.6(10)	*j*	4.034 40(14)	1.8(3)
e	4.022 9(14)	5.3(2.6)	*k*	4.036 22(4)	0.65(1)
f	4.027(5)				

The identification of resonances made with this fit are only tentative. Some of the assignment of resonances are, however, more plausible than others. The resonances *i*, *j* and *k* can clearly be seen in all three channels. The parameters extracted for these resonances can thus be considered to be somewhat reliable. In the region of resonances *a* and *b*, below 4.01 eV, at least two resonances were found to be necessary to reproduce the observed structure. Between 4.01 eV and the Cs(10 $^2P_{1/2}$) channel opening, it is clear that many resonances are needed to reproduce the modulations in the three channels. The assignment of resonance parameters might, however, have many different solutions depending on the resonance model and the functional form used for

the non-resonant cross section. Apart form the identification of resonance *i*, the assignment of resonances in the region, *c* to *h*, is highly uncertain. It is not even clear how many resonances are responsible for the observed structure in this energy range.

10.5 Conclusions

We have performed a high-resolution measurement of three partial cross sections for the photodetachment of the Cs^- ion into final state channels that involve highly excited states of the residual Cs atom. In the case of states having a positive polarizability, the cross section exhibits a very sharp increase at the channel openings. This is in agreement with what has been previously observed in the photodetachment of other negative ions of the alkali metals under similar conditions [134, 153]. However, the Cs(6 ^2G) channel, which is expected to have a negative polarizability, shows a slow onset of the cross section. The cross section at this threshold exhibits the same general behaviour as previously observed at the opening of the K(5 ^2G) channel in K^- photodetachment [153]. The cross sections in the Cs(10 ^2S), Cs(6 ^2F) and Cs(6 ^2G) channels were modulated by the presence of many resonances below the Cs(10 $^2P_{1/2,3/2}$) channel openings. A tentative identification and assignment of the parameters of these resonances was made. A total of eleven resonances were fitted in the data analysis. However, only three identifications can be considered to be reliable (resonances *i*, *j* and *k* in Table 10.1). These resonances have energies of 4.032 96(5) eV, 4.034 40(14) eV and 4.036 22(4) eV and widths of 0.61(9) meV, 1.8(3) meV and 0.65(1) meV, respectively. Our inability to identify some of the resonances was primarily due to the fact that many resonances were overlapping. A structure with a width of 0.095(11) meV were identified in the Cs(10 ^2S) cross section at a photon energy of 3.984 040(11) eV. Due the large uncertainty in the electron affinity of the Cs atom, it was not possible to determine if this structure was situated above or below the Cs(6 ^2F) channel opening.

The simple parametrization of resonance profiles used in the analysis of the data does not allow us to definitively identify the series of double excited states that are responsible for the modulations seen in the measured cross sections. Clearly, such a process would require *ab initio* calculations that are not available at this time. Such calculations would present a formidable challenge since the Cs^- ion and the Cs atom are both heavy, many electron systems. Many-body and relativistic effects

would have to be incorporated in these calculations in order to give a proper description of the systems.

Financial support from the Swedish Research Council is gratefully acknowledged. CWW received support from the Wenner-Gren Foundation, the Andrew W. Mellon Foundation, and NSF Grant Nos. 0757976 and 1068308. HH acknowledge the support by the Deutsche Forschungsgemeinshaft, Grant No KI 865/3-1.

CHAPTER 11

Main Scientific Results and Discussion

"The most exciting phrase to hear in science, the one that heralds new discoveries, is not 'Eureka!' but 'That's funny ..."

—Isaac Asimov

11.1 Electron rescattering in strong field photodetachment of negative ions

In chapter 4 we investigate the process of rescattering, described in section 2.2. Our motivation for the study is that the rescattering effect has not previously been observed in negative ions and recent predictions that the ratio of rescattered electrons to the direct electrons is larger in the heavier halogens, Br^- and I^- compared to F^- [90, 91]. The experimental setup described in section 3.1 is used. However, only one laser beam is present in the interaction region. The idler beam is blocked and the signal beam is used. Instead of a cesium sputter ion source a gas discharge source is used to produce Br^- and F^- ions from a gas mixture. Br^- are produced from a mixture of 10% of methyl bromide and 90% of Krypton. F^- ions are produced from a mixture of 10% NF_3 and 90% Krypton. The signal output of TOPAS is set to 1300nm. A pulse length of 100 fs, a focus size of 40 μm and a peak intensity in the focus of 6.5×10^{13} W/cm^2 are achieved. The detached electrons are detected by our EIS.

The upper part of Fig. 11.1 presents the angle resolved momentum distribution of the detected photoelectrons. The angle θ represents the

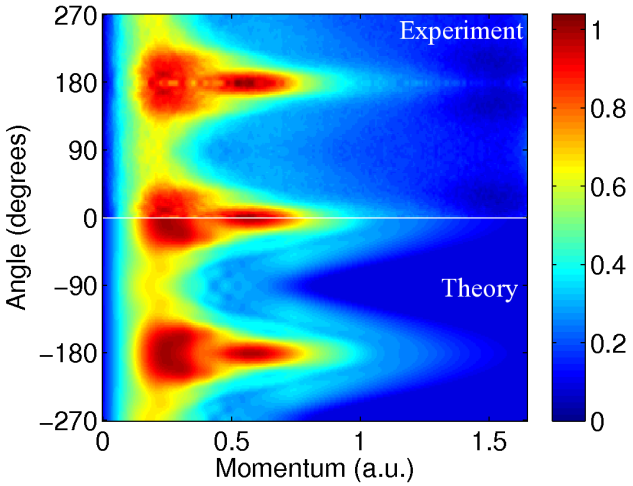

Figure 11.1: *Angle-resolved momentum distribution of photoelectrons detached from Br^- exposed to a 100 fs laser pulse with a wavelength of 1300 nm and peak intensity of 6.5×10^{13} W/cm^2. Upper part $(0° \leq \theta \leq 270°)$ presents experimental results while the lower part $(-270° \leq \theta \leq 0°)$ are predictions by the rescattering theory.*

emission angle relative to the laser polarization. Two jets of high energy electrons emitted along the laser polarization at 0° and 180°. The lower part of Fig. 11.1 presents the result of a simulation using the modified SFA, Eq. 2.10. In the simulation the spatiotemporal intensity distribution of the laser focus is taken into account as described in [83]. Furthermore, due to the high laser intensity the detachment process is saturated. Therefore depletion of negative ions are taken into account in the simulation [83]. There is an excellent agreement between theory and experiment. Fig. 11.2 shows a cut in the electrons energy distribution along laser polarization direction. The amount of high energy electrons are well described by the modified SFA. The rescattering term in Eq. 2.10 becomes dominant above 15 eV. In atoms the rescattering process is observed as a high energy plateau extending along the laser polarization direction. The plateau reaches up to and has a cutoff at 10 U_p [170], where U_p is the ponderomotive energy given by Eq. 2.4. In our experiment U_p for Br^- and F^- are 10 eV and 5 eV respectively. The observed plateau in the present experiments is rather an inclined plane instead and it does not extend up to 10 U_p, this interpreted as an effect of the strong saturation of the photodetachment process. Only 1% of the ions in the laser focus survives the leading edge of the pulse to be detached at the peak intensity. Integrating the product of the detachment rate and the population in the focus gives rise to the ob-

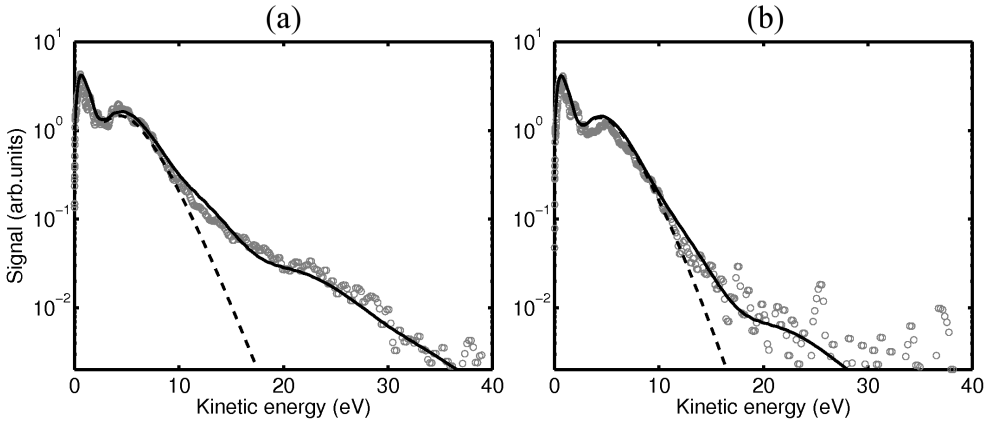

Figure 11.2: *Kinetik energy dirtribution of observed photoelectrons from detachment of Br^-* ***(a)*** *and F^-* ***(b)****. Circles: experiment; Dashed line: Standard SFA; Solid Line: SFA with rescattering taken in to account.*

served inclined plane. In such case the observed rescattering signal should be less sensitive to the peak intensity used in the simulations, and indeed no significant difference in the rescattering signal is observed when varying the peak intensity as much as 30%. The atomic core is smaller in F than in Br. This is reflected in the Z-parameter (Eq. 2.11) being lower (smaller potential depth) as well as the smaller D parameter (steeper decrease of the potential). The rescattering signal is less pronounced in F^- compared to Br^-. This is in agreement with decreased probability for the electron to rescatter of the parent core due to the smaller size of the fluorine atom.

11.2 Strong field detachment of molecular negative ions.

In chapter 5 strong field photodetachment of F^- and F_2^- are compared. The same experimental setup is used as in section 11.1. Recently the SFA has been extended to include diatomic molecular anions [171–173]. In the molecular SFA the orientation of the molecular axis relative to the laser polarization is of importance as well as the symmetry of the initial electronic state. The emission of photoelectrons from two centers is expected to give rise to quantum interference patterns in the photoelectron spectra. The aim of this experiment was to test the theory described in [173], where two versions are described. In the first version the initial state is described solely as the ground state of the

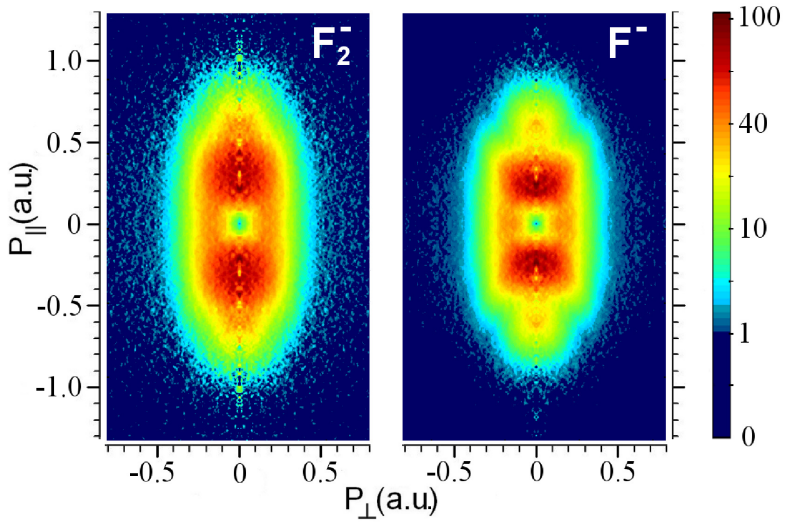

Figure 11.3: *Momentum distribution of electrons detached from F_2^- (left) and F^- (right). $P_\perp$ and $P_\parallel$ represent the momentum components perpendicular and parallel to the laser polarization axis, respectively. The laser wavelength is 1300nm. The pulse length is 130 fs, focus size is 46 μm and the peak intensity is 3.4×10^{13} W/cm^2. The laser polarization direction is vertical in the images.*

molecular anion. In the second version the initial state includes the laser field. The two versions are referred to as undressed and dressed, respectively. In the dressed version of the molecular SFA the external electric field from the laser gives rise to a potential difference between the two atomic centers of the molecule. In simulations this gives rise to significantly different energy and angular distributions of the emitted photoelectrons.

Negative ions of F and F_2 were exposed to a 1300 nm linearly polarized laser field. The pulse length was 130 fs, the focus size was 46 μm and the peak intensity 3.4×10^{13} W/cm^2. In the ion source F^- and F_2^- are produced simultaneously. By tuning the Wien filter either of the two species is guided through to the interaction region. The data acquisition was broken in to shorter segments, alternating between F^- and F_2^-, in order to eliminated long term drifts of the laser parameters. The recorded, abel inverted, images of F^- and F_2^- are presented in Fig. 11.3.

The two images exhibit some clear differences. The F_2^- spectra is broader along the laser polarization direction (vertical in the images). The non-monotonic structure in the F^- spectra at $P_\parallel = \pm0.6$ a.u. is due to the quantum interference discussed in section 2.2 and is not visible in the

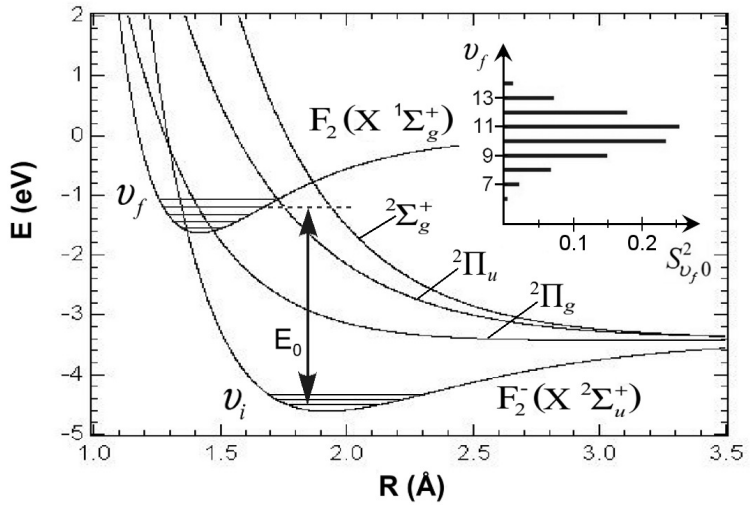

Figure 11.4: *Potential energy curves of electronic states of F_2^- and the ground electronic state of F_2. ν_i and ν_f are the vibrational quantum numbers of F_2^- and F_2 vibrational states, respectively, E_0 denotes the threshold energy for a given $\nu_i \rightarrow \nu_f$ transition. The insert shows the squared overlap of nuclear wave functions, $S^2_{\nu_f \nu_i}$, for $\nu_i = 0$ and different ν_f values.*

F_2^- spectra. To simulate the photodetachment of F_2^- we need to specify the electron affinity of the molecule. The potential curves for F_2^- and F_2 are presented, together with three dissociative states in F_2^-, in Fig. 11.4 the curves are obtained from reference [174]. We assume that the molecules are created in their lowest vibrational state, $\nu_i = 0$. The molecular potential is approximated by the morse potential. The core overlap between the initial vibrational state, ν_i, and a series of vibrationally excited states ν_f in the F_2 molecule has been calculated, for more details see [84]. The results is presented in the inset of Fig. 11.4. The largest transition probability is found to be $\nu_i = 0 \rightarrow \nu_f = 11$. Only this transition is considered. The electron affinity in the transition is defined as the energy difference between $F_2^-(\nu = 0)$ and $F_2(\nu = 11)$. The electron affinity is 3.965 eV. The molecular version of the SFA used is described in shortly in chapter 5 and in more detail in [173]. Fig. 11.5 (a) presents simulations assuming a dressed (dashed line) and undressed (solid line) initial state, circles prepresent experimental data. Neither of the two versions reproduce the observed energy spectrum of photoelectrons. An uncertainty in the experiment is dissociation of F_2^- followed by detachment of F^-. The energy needed to dissociate F_2^- in to F^- and F is lower than the electron affinity, see Fig. 11.4. The timescale of molecular dissociation is on the order of 10 fs and can thus occur in the leading edge of the laser pulse. The F^- orig-

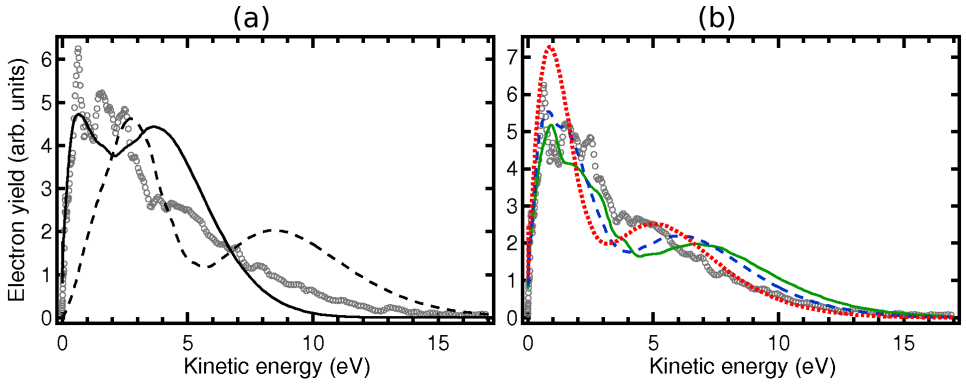

Figure 11.5: *Energy distribution of photoelectrons emitted from F_2^- along the laser polarization axis.* ***(a)*** *shows predictions by the undressed (solid line) and dressed (dashed line) versions of the molecular SFA. Circles represent experiment. The curves are normalized according to the integrated yield.* ***(b)*** *Comparison of the experimental energy distribution with predictions by the model that assumes strong-field dissociation of F_2^- followed by photodetachment of F^-. Calculations are performed for different initial times (see text): $-\sigma_t$ (dotted line), $-\sigma_t/2$ (dashed line), and 0 (solid line). The curves are normalized according to the integrated yield.*

inating from the dissociation process will be created closer to the peak intensity in the time envelope of the laser pulse, and thus resemble an energy spectrum of F^- recorded at a higher laser intensity.

Fig. 11.5 (b) presents simulations where the initial time, t_0, is varied. The parameter t_0 is the time when the negative ions are exposed to the laser field. Photoelectron distributions for $t_0 = -\sigma_t, -\sigma_{t/2}, 0$ are simulated. Here $\sigma_t = 79$ fs is the measured Gaussian width of the temporal intensity profile $I(t) = I\exp(-t^2/\sigma_t^2)$, and the peak of the pulse is at $t = 0$. The simulated energy distribution of photoelectrons is broader when t_0 is chosen close to the center of the laser pulse. This is explained by the fact that the population of negative ions is then less depleted when exposed to the high intensities in the middle of the pulse, giving rise to the most energetic photoelectrons. However, even for $t_0 = 0$, the simulated spectra is narrower than the measured one for low energy electrons ($\leq$3.5 eV), while the high energy electrons are overestimated. The high energy part of the spectrum can be reproduced by averaging over simulations stretching form $t_0 = -\infty$ to $t_0 = 0$. However, to explain the low energy part of the spectrum a more sophisticated model of the detachment process of F_2^- is needed. Furthermore, a coincidence technique being able to separate photoelectrons from detachment of F_2^- and F^- is needed to unambiguously being able to test wether the initial state should be dressed or undressed in the

molecular SFA.

11.3 Motion of an electronic wave packet in carbon and silicon atoms

In chapter 6 and 7 we did time resolved pump-probe experiments on electron dynamics in the valence shell of carbon, silicon and germanium atoms. The pump-probe setup described in section 3.1 was used. The linearly polarized pump pulse initiates a three photon detachment process of the carbon negative ion ground state, $^4S_{3/2}$ to the ^3P ground state of the carbon atom. See Fig: 11.6. The total electron configuration of the carbon negative ion is $1s^2 2s^2 2p^3\ ^4S_{3/2}$. The valence shell holds three p electrons in a spherical symmetric configuration. The linearly polarized pump pulse defines a quantization axis for the angular momentum of the electrons. A p-electrons has an angular momentum of l=1, hence m_l=0 and m_l=$\pm$1 are possible. The detachment rate via tunneling is greatly dependent on the m_l quantum number. m_l=0 states shows detachment rates typically one order of magnitude larger than $m_l \neq 0$ states [74,112]. Hence, one can expect the substates having m_l=0 to detach first in the laser pulse, leaving the atom in an aligned state consisting of m_l=$\pm$1. The linearly polarized probe pulse ionizes the atom after a controlled time delay and the ionized electrons are detected in our EIS. The amount of high energy electrons in the image is strongly dependent on the orbital alignment in the atom.

The alignment effect in the probe step is visualized through the recording of four images for each pump-probe time delay. First, an image was recorded with the pump and probe beams polarizations aligned perpendicular with respect to each other (Fig. 11.7(a)). Second, a background image with only the pump laser present was recorded (Fig. 11.7(b)). The third image was obtained with the pump and probe beams aligned parallel (Fig. 11.7(c)). Finally, a background image with only the pump laser present was recorded (Fig. 11.7(d)). The effect of the probe beam is isolated by subtracting (b) from (a) and (d) from (c). The alignment effect in the carbon atom is visualized by comparing the probe yields obtained with the perpendicular and parallel polarization geometries. The method is graphically depicted in Fig. 11.7. A clear difference in signal is observed when the two laser pulses have parallel polarizations to the image where they have perpendicular polarizations.

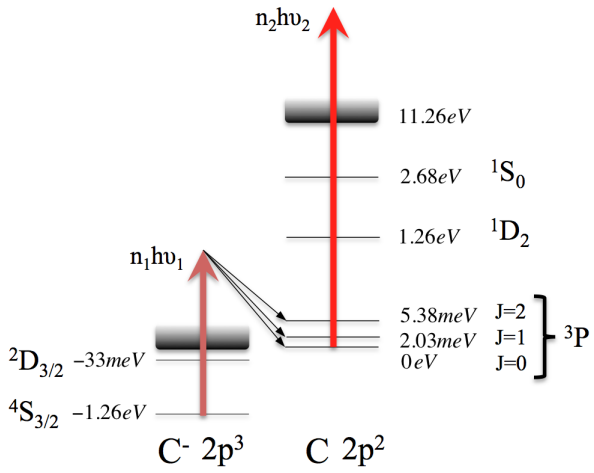

Figure 11.6: *Energy level diagram of the negative carbon ion and the carbon atom. [85]*

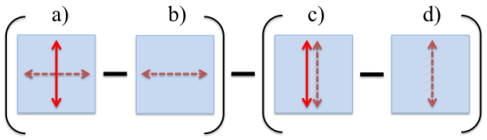

Figure 11.7: *Dashed and solid arrows represent the polarization direction of the pump pulse and the probe pulse respectively.*

In Fig. 11.7(b) the electric field from the laser is parallel to the detector, hence, the electrons are emitted parallel to the detector and spread over a large are. In (d) the electric field from the laser is pointing into the detector meaning that most electrons are emitted into the center of the detector. The total signal in (b) and (d) were summed over the whole detector area and the integrated signal is smaller in (d), indicating saturation of the central parts of the detector. However, we put our interest in the high energy electrons detected far from the center of the detector.

In Fig. 11.8 the three images are recorded with three different time delays between the pump and probe pulses. The polarization direction of the probe pulse is vertical, indicated by the red arrow in Fig. 11.8 (d). In Fig. 11.8 (a) no high energy electrons are emitted along the laser polarization. In (b), recorded 300 fs later, some high energy electrons in the shape of two jets are emitted along the laser polarization. In (c), recorded another 300 fs later, a large amount of high energy electrons is detected. A clear time dependence of the amount of strong field ionized electrons is observed. A series of images at time delays between 600fs and 5000fs have been recorded. In Fig. 11.9 the signal in the jets of each figure is summed and plotted as a function of the time delay

between the pump and probe pulse. The areas over which the signal is summed are indicated by the two rectangles in Fig. 11.8 (d). A strong modulation in the ionization signal is visible. The modulation is interpreted as a change in the electron density in the m_l=0 orbital, aligned along the probe pulse polarization.

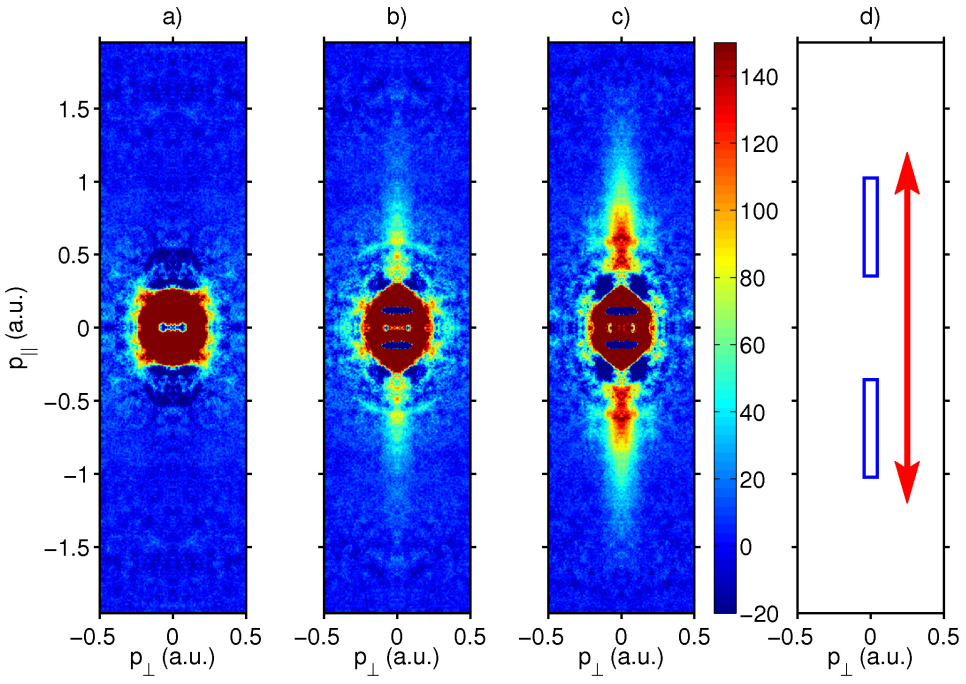

Figure 11.8: *Images recorded at time delays between pump and probe pulses of 2000 fs (a), 2300 fs (b) and 2600 fs (c). $P_{||}$ and $P_{\perp}$ represent the momentum of the electrons emitted parallel and perpendicular with respect to the laser polarization of the probe beam, shown as the arrow in (d). A strong modulation in the amount of high-energy electrons is observed. The two rectangles shown in d) represent the area over which the electron yield was integrated in the data shown in Fig. 11.9.*

Since we remove one out of three electrons from an initially spherical symmetric electronic state I find it more expressive to show the spatial probability distribution of the created hole (Fig. 11.10 (a)) rather than that of the remaining electrons. The oscillation can quantitatively be understood by inspecting the spatial hole density distributions in the carbon atom shown in Fig. 11.10. In Fig. 11.10 (a), a hole has been burnt along the polarization axis (vertical). The photoionization yield at this instance is very low since the electron density along the polarization axis is depleted, this corresponds to Fig. 11.8 (a). 600 fs later, shown in figure 11.10 (c), the different time evolutions of the substates (J=0,1,2) have changed the electron distribution completely. The hole

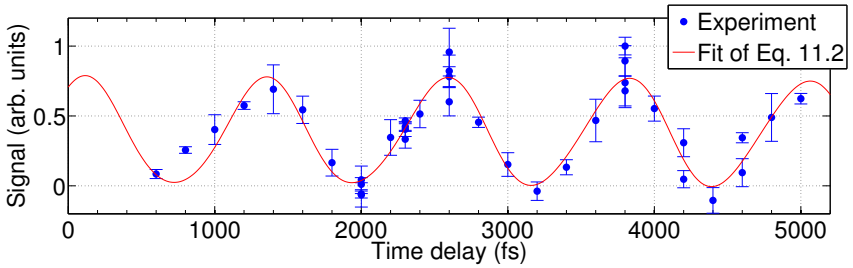

Figure 11.9: *Pump probe experiment on the carbon atom. The number of high energy electrons created in the ionization step plotted as a function of the time delay between the pump and probe pulses.*

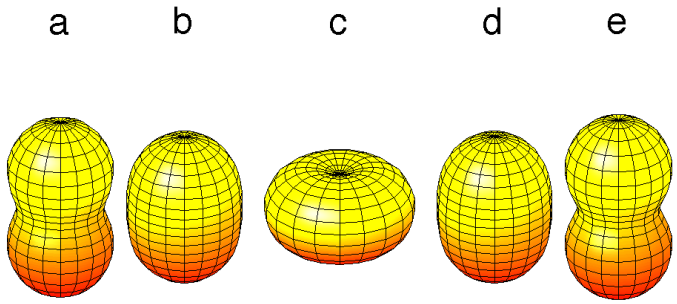

Figure 11.10: *Spatial hole density distributions in the carbon atom. (a) The distribution after exposure to a strong laser field where a hole has been burnt along the axis of polarization (vertical in the figure). (b) The hole distribution after 300 fs. (c) The probability distribution after 600 fs, where the wave packet movement has filled the hole along the laser polarization. (e) The probability distribution after 900 fs. Revival of the initial hole distribution takes place 1200 fs after the wave packet is created. The theory section of chapter 7 contains a detailed description on how SFA theory in combination with a density matrix formalism is used to simulate the creation and time evolution of the hole in the electron density in the atom.*

in 11.10 (a) is now filled and the ionization yield along the laser polarization is enhanced, corresponding to Fig. 11.8 (c). The hole is revived after 1200 fs (Fig. 11.10 (e)). For a more thorough discussion see the theory section in chapter 7, where we use the SFA theory in combination with a density matrix formalism to simulate the creation and time evolution of the hole in the electron density in the atom. The hole is described as a wave packet moving in the valence shell of the atom. The same experiment has been performed on the silicon atom. The electron configuration in silicon is identical to carbon but the fine structure splitting of the ground state is larger. A similar oscillatory behavior of the ionization signal is observed but with a shorter time period. In Fig. 11.11 the results from a pump probe experiment on silicon is presented. A third experiment was performed on the germanium atom. However, the oscillation period was to short to be resolved with a laser pulse of 100 femtoseconds duration.

The modulation of the amount of ionized electrons in the probe step is a manifestation of a spatial change of the electron density in the carbon atom. The population in the atom along the laser polarization direction is directly projected on to the detector. For the very first time the electron dynamics in the ground state of an atom has been recorded. The pump pulse creates a wave packet in the carbon atom. The motion of the wave packet produces an oscillation in the electron probability density along the laser polarization direction. The method used to detect the probability density as a function of time shows a direct visualization of the oscillating wave packet. A near complete modulation of the ionization signal is observed over a full oscillation period in the case of carbon, see Fig. 11.9. The oscillations period in the silicon atom is only twice the probe pulse duration and a smearing of the signal occurs and only a 25% modulation is seen. (Fig. 11.11). No sign of decoherence is visible within four full oscillations in carbon and six oscillations in silicon.

The coherently created wave packet can be described by a sum of three wave functions. One wave function for each fine structure level J_i, having its own phase velocity. The phase velocity is proportional to the energy of the state. The wave packet can be expressed as

$$\Psi = \psi(J_0)e^{\frac{-iE_0}{\hbar}t} + \psi(J_1)e^{\frac{-iE_1}{\hbar}t} + \psi(J_2)e^{\frac{-iE_2}{\hbar}t}, \qquad (11.1)$$

where $\psi(J_i)$ represent some time independent spatial probability density distribution. A beat between these three wave functions occurs since they interfere constructively and destructively as they evolve

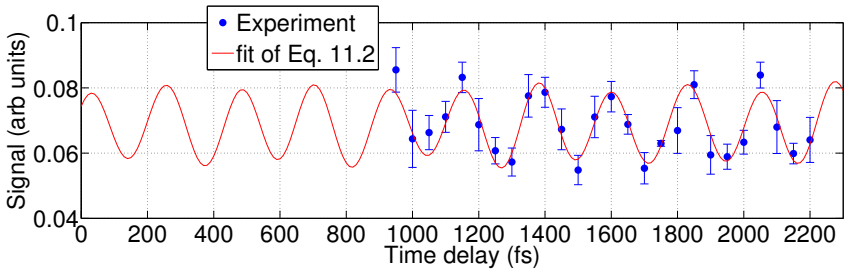

Figure 11.11: *Pump probe experiment on the silicon atom. The amount of high energy electrons created in the ionization step plotted as a function of the time delay between the pump and probe pulses.*

with their individual phase velocities $-\hbar E_i$. The ground state consists of three fine structure levels therefore three different beat frequencies are possible, corresponding to the energy difference between the fine structure levels; $J_{1\leftrightarrow 0}$, $J_{2\leftrightarrow 0}$ and $J_{2\leftrightarrow 1}$. The curve in Fig. 11.9 is a fit of three cosine functions each having its own time period, see Eq. 11.2. The time period of the beat is given by $\tau = h/\Delta E$, where ΔE is the energy spacing between two states.

$$f(t) = \alpha + \beta cos(\frac{2\pi}{\tau_1}(t+\Delta)) + \gamma cos(\frac{2\pi}{\tau_2}(t+\Delta)) + \epsilon cos(\frac{2\pi}{\tau_3}(t+\Delta)) \quad (11.2)$$

In table 11.1 the theoretical beat periods are presented together with the experimental results acquired from the fit of Eq. 11.2.

Table 11.1: Carbon and Silicon

Carbon	ΔE (meV)	$\tau_{cal} \pm \sigma$ (fs)	$\tau_{exp} \pm \sigma$ (fs)	Exp. Beat Amp.
$J_{0\leftrightarrow 1}$	2.03	2034	1931 ± 1456	0.01 ± 0.075
$J_{0\leftrightarrow 2}$	5.38	769	637 ± 23	0.081 ± 0.070
$J_{1\leftrightarrow 2}$	3.35	1235	1229 ± 16.5	1 ± 0.056
Silicon				
$J_{0\leftrightarrow 1}$	2.03	433	408 ± 13.2	0.139 ± 0.12
$J_{0\leftrightarrow 2}$	5.38	149	175 ± 6.7	0.049 ± 0.12
$J_{1\leftrightarrow 2}$	3.35	228	225 ± 2.7	1 ± 0.12

In both carbon and silicon $J_{1\leftrightarrow 2}$ is the main beat frequency observed. $J_{0\leftrightarrow 1}$ and $J_{0\leftrightarrow 2}$ are comparably weak. In the case of carbon and silicon the J=2,1,0 states are populated as 5,3,1 respectively. Regarding the beat periods, the agreement between theory and experiment is found to be excellent for the $J_{1\leftrightarrow 2}$ case in both carbon and silicon.

11.4 Structure of negative ions

When investigating doubly excited states and thresholds in photodetachment of K^- and Cs^- we use the resonant ionization scheme and experimental setup described in section 3.2. K^- ions are produced from a cathode packed with potassium carbonate powder, K_2CO_3. When producing Cs^- ions, a blank aluminum cathode was used and cesium deposited from the oven was sputtered and formed negative ions. The ions where accelerated to 6 keV and mass selected in the sector magnet before entering the interaction region in a collinear manner with the γ_{UV} and γ_{IR} laser beams as depicted in Fig. 3.8.

11.4.1 Potassium

We have investigated the photodetachment process of K^- leading to the excited 7 ^{2}S, 5 ^{2}F and 5 ^{2}G states in the neutral potassium atom. The γ_{UV} energy range is from 4.250 eV to 4.360 eV, covering the range from below K(7 ^{2}S) up to and including the K(7 ^{2}P) threshold. The results are presented in chapter 8 and 9. Previous experiments at GUNILLA on K^- investigating photodetachment from the negative ion to K(5 ^{2}S) comprises the energy range 4.193-4.298 eV reaching just above the K(5 ^{2}G) threshold [152]. Theoretical predictions, on cross section curves and resonances, extending up to 4.360 eV were subsequently published in [135].

A measurement where the γ_{UV} laser was scanned over in the perviously investigated region below the K(5 ^{2}F) threshold was conducted and the result is presented in Fig. 11.12. Three resonances represented by thick vertical lines were seen, their widths are indicated by the thick horizontal lines. To compare the experimental results with theory a shore profile [158] together with a linear background as in [141] is fitted to the data set. The Shore profile is given by

$$S = \frac{a\epsilon + b}{\epsilon^2 + 1} \tag{11.3}$$

where a and b are fit parameters. The energy parameter $\epsilon = (\hbar\omega - E_r)/\frac{\Gamma}{2}$ contains the resonance energy, E_r and the resonance width, Γ. While $\hbar\omega$ is the photon energy. As mentioned before we observe three resonances and we fit sum of three Shore profiles together with a linear

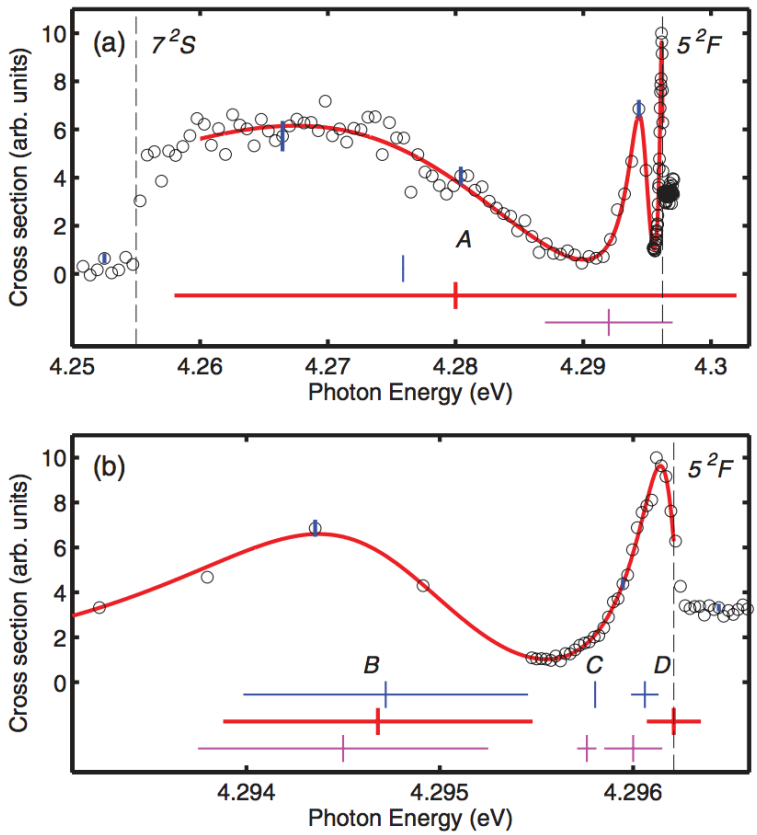

Figure 11.12: *Partial cross section for photodetachment of K^- into the K(7 ^2S) channel. Vertical dashed lines indicates channel openings. Resonance positions and widths are represented by the vertical and horizontal lines, respectively. The resonance parameters obtained from the current investigation are indicated by thick lines, thin lines above the thick lines represent theoretical values from [135] while the thin lines below represent the previous experiment [152]. In reference [135] there is no width specified for the resonance at 4.28 eV.*

background

$$\sigma = (c + \hbar\omega\, d)\left(1 + \sum_{i=1}^{3} \frac{a_i \epsilon_i + b_i}{\epsilon_i^2 + 1}\right) \tag{11.4}$$

where c and d are fit parameters describing the non-resonant cross section. The numerical values of the positions and widths of the resonances obtained in present measurement are listed as A, B, C and D in Table 11.2 together with predictions and previous measurement.

Subsequently the photodetachment cross section in the range between 5 ^{2}F and 7 ^{2}P channel openings were measured. No previous experimental results are available in this energy range. There are theoretical

Table 11.2: *Resonance parameters obtained from the present cross section measurements on K^- as well as theoretical predictions [135] and previous measurements [152].*

Label	Channel / source	E_r (eV)	Γ (meV)
A	K(7 ^{2}S)	4.28(2)	44(20)
	K(5 ^{2}S)[a]	4.292(2)	10(2)
	Calculation[b]	4.275 90	
B	K(7 ^{2}S)	4.294 68(9)	1.6(3)
	K(5 ^{2}S)[a]	4.2945(1)	1.5(2)
	Calculation[b]	4.294 72	1.472 2
C	K(7 ^{2}S)[c]		
	K(5 ^{2}S)[a]	4.295 76(4)	0.10 (8)
	Calculation[b]	4.295 803 1	0.002
D	K(7 ^{2}S)	4.296 21(5)	0.28 (5)
	K(5 ^{2}S)[a]	4.2960(2)	0.30 (3)
	Calculation[b]	4.296 06	
E	K(7 ^{2}S)	4.321(5)	19 (6)
	K(5 ^{2}F)	4.327(7)	26 (9)
	K(5 ^{2}G)	4.325(4)	25 (8)
	Mean[d]	4.324(3)	22 (5)
	Calculation[b]	4.32339	27.718 3
	K(7 ^{2}S)	4.320(3)	25 (9)
	K(5 ^{2}G)	4.319(4)	27 (4)
	Mean[d]	4.320(3)	27 (4)
F	K(7 ^{2}S)	4.353 2(6)	2.2 (5)
	K(5 ^{2}F)	4.353 2(5)	2.2 (4)
	K(5 ^{2}G)	4.353 00(13)	1.66 (12)
	Mean[d]	4.353 02(13)	1.72 (12)
	Calculation[b]	4.353 50	

[a] Previous experimental results from [152].
[b] Theoretical predictions from [135]
[c] Not observed in the present measurement.
[d] Weighted mean of the obtained parameters from all three channels.
[e] Parameters obtained from data set in chapter 8.

predictions on two resonances between 4.3 eV and 4.36 eV [135]. The cross section leading to the 7 ^{2}S, 5 ^{2}F and 5 ^{2}G states were recorded. The result is presented in Fig. 11.13. Numerical values of the resonance positions and widths are labeled as E and F in Table 11.2. Two resonances are observed being in good agreement with theoretical predictions [135]. However, the most interesting observation is the fundamentally different threshold behavior in the 5 ^{2}F and 5 ^{2}G channels, visible in 11.13 (c) and (d). The 5 ^{2}F channel opening is sharp, like a step function while the 5 ^{2}G channel exhibits a slow onset. The cross section is suppressed over several tenths of eV. A close up of the region containing the two channel openings is presented in Fig. 11.14.

The step like threshold behavior of the 5 ^{2}F channel opening has been observed previously [134]. The Wigner law neglects the polarizability part of the binding potential when describing the threshold behavior. See Eq. 2.1 and Eq. 2.2. Hence, for states having a large polarizability the Wigner law is not expected to reproduce the observed threshold behavior. The polarizability of the 5 ^{2}F and 5 ^{2}G states has been calculated to be 3.9×10^6 a.u. and -3.1×10^6 a.u., respectively [135]. Negative polarizabilities are counterintuitive. When an electron approaches a neutral atom the electron cloud is shifted towards the electron in contrast to ordinary polarizability where the electron cloud is repelled. This phenomena can not be explained by classical electromagnetism. The increase of negative charge in the direction of the incoming electron can be understood by considering constructive interference between the incoming electron's wave function and the collective wave function of the electrons in the atom. The step like threshold of the 5 ^{2}F state can be explained using Eq. 2.1. For a state having ℓ=2 and α= 3.9×10^6 a.u. the maximum of the potential is at r=1145 a.u. and the height of the centrifugal barrier is a mere 31 μeV. The probability of detachment is zero when the photon energy is less than depth of the potential. When the photon energy is larger than the potential depth the bound electron has a probability of tunneling through the centrifugal potential barrier in to the continuum. However, when the photon energy is larger than the barrier there is still a probability that the electron is reflected on the barrier. Thus, the centrifugal barrier is expected to influence the cross section up to a few times the barrier hight. The cross section observed in the 5 ^{2}F state reaches its maximum value already after 100-200 μeV.

The data shown in lower the spectrum in Fig. 11.14 represents the first observations of photodetachment where the negative polarizability of the final state is the dominant interaction. The cross section is sup-

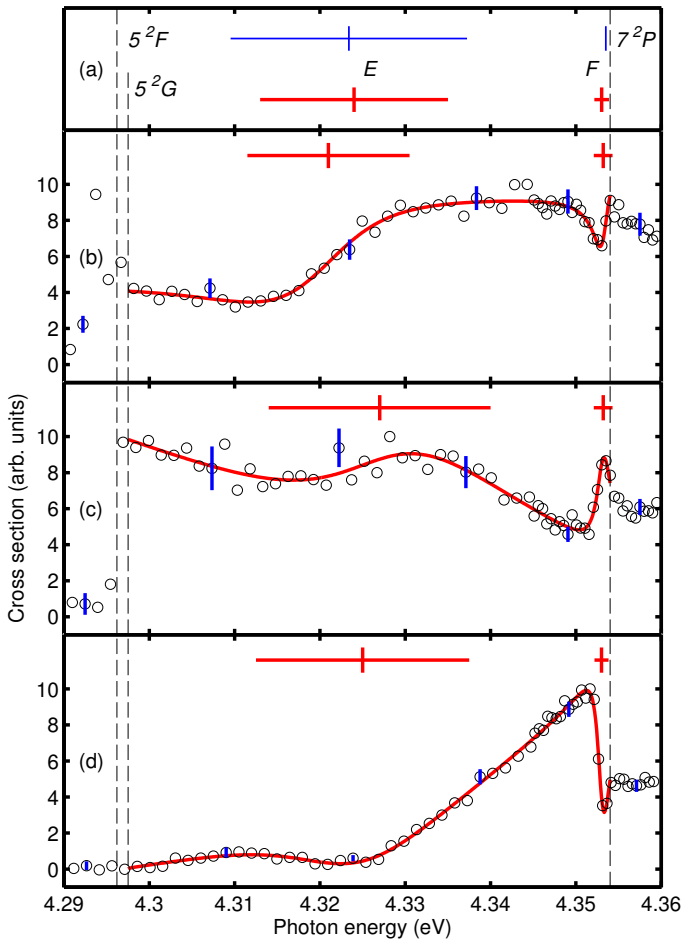

Figure 11.13: *Partial photodetachment cross sections for K^-. (b), (c) and (d) show the K(7 ^2S), K(5 ^2F) and K(5 ^2G) channels, respectively. Solid curves are Fits of Eq. 11.4. Thick vertical and horizontal lines indicates the resonances parameters. Weighted means of the resonance parameters are presented as thick lines in (a). The resonance parameters calculated by Liu [135] are indicated by thin lines in (a). Dashed vertical lines indicate channel openings.*

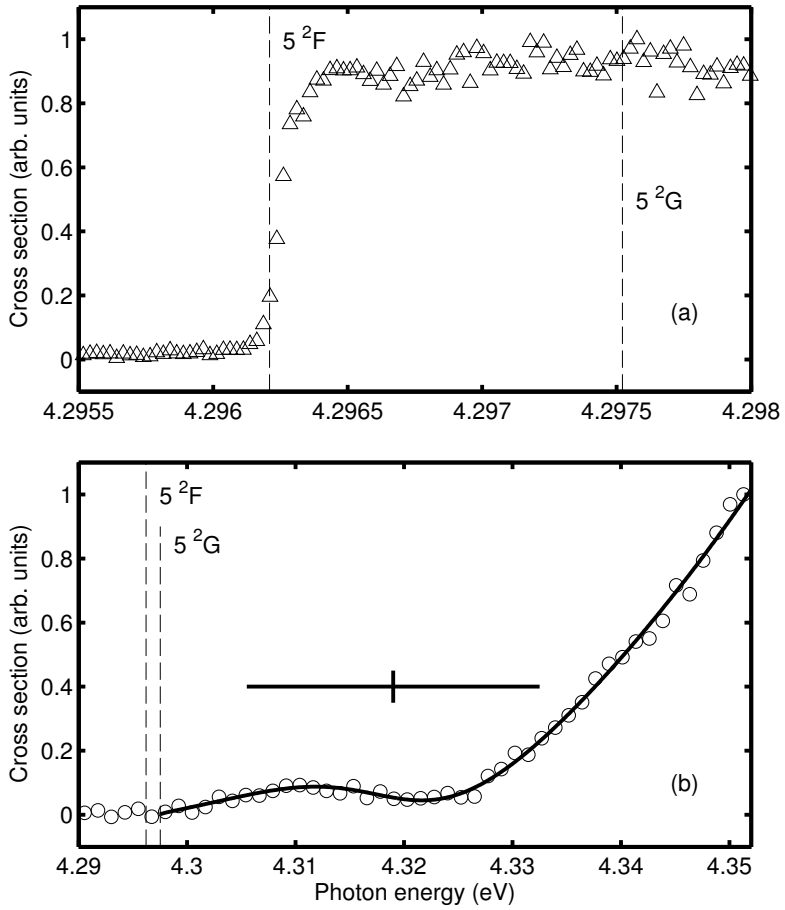

Figure 11.14: *The threshold behavior in the K(5 ^{2}F) and K(5 ^{2}G) channels is shown in (a)and (b), respectively. The solid line in (b) is a fit of the new threshold law described by Eq. 11.9.*

pressed over a large energy range. A new model has been developed to describe the behavior of the 5 ^{2}G threshold. At 508 a.u. the two parts of Eq. 2.1 are of equal magnitude (Fig. 11.15). The total potential at this point is 1.3 meV. Hence, the polarizability is expected to dominate for energies large than 1.3 meV over the threshold, which is most of the observed spectrum. The negative polarizability induces a repulsive potential for the electron being detached. For the energy range in our experiment the classical turning point for a free electron is at a radius of 160 a.u. The classical turning point is where the wave function of the final state is no longer an decaying exponential function, but a free electron described by a plane wave. Therefore the overlap between the initial state and final state is occurring in the tunneling region. The part of the free electron's wave function tunneling in to the repulsive potential is given in [175]

$$\psi_k(r) = \frac{C(E_e)}{r\sqrt{p(r)}} exp\left(-\int_r^{r_0} p(x)dx\right), \tag{11.5}$$

where $k = \sqrt{2E_e}$ is the momentum of the outgoing electron, $p(r) = \sqrt{|\alpha|/r^4 - 2E_e}$, r_0 is the classical turning point and $C(E) \sim E^{-1/4}$ is a normalization coefficient. The integral in Eq. 11.5 has an analytical solution yielding the following expression

$$\psi_k(r) = \frac{C(E_e)}{r\sqrt{p(r)}} \times exp\left(B(2E_e|\alpha|)^{1/4} - \frac{\sqrt{|\alpha|}}{r}{}_2F_1\left[-\frac{1}{2}, -\frac{1}{4}; \frac{3}{4}; \frac{r^4}{r_0^4}\right]\right) \tag{11.6}$$

where ${}_2F_1$ is a hypergeometric function while $B = (2\pi)^{3/2}/\Gamma(1/4)$=1.198 is a constant. Assuming that the main contribution to the overlap is given at small radius Eq. 11.6 is expanded in $(r/r_0)^4$ around r=0. Considering only the leading term of the expansion the wave function takes the following form

$$\psi_k(r) = E_e^{-1/4} exp[B(2E_e|\alpha|)^{1/4}]\chi(r)]. \tag{11.7}$$

The dependency on r is separated from the energy dependency by doing this expansion. The transition matrix element is given by $\langle\psi_f|\hat{V}|\psi_0\rangle$. ψ_f is the product of the residual atom wave function and the outgoing electron wave function ψ_k. The sole energy dependency in the matrix element is in ψ_k. The cross section for photodetachment is given by

$$\sigma_t h \sim \int_k |\langle\psi_f|\hat{V}|\psi_0\rangle|^2 \delta(\hbar\omega - EA_K - E_{5\ {}^2G} - E_e)\frac{d^3\mathbf{k}}{(2\pi)^3} \tag{11.8}$$

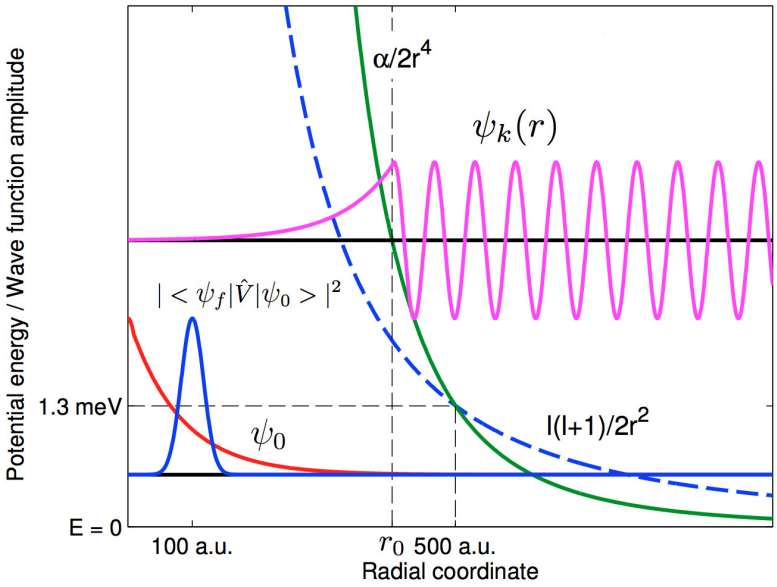

Figure 11.15: *Sketch presenting the wave functions of the initial state, ψ_0, and the outgoing electron, ψ_k as well as the potential curves of Eq. 2.1. ψ_f is the product of the residual atom wave function and the outgoing electron wave function ψ_k. The blue solid curve represents the overlap of initial and final state wave functions. Picture by A. O. Lindahl.*

The delta function represents the conservation of energy. The energy dependency of the resulting cross section law is

$$\sigma_{th} \propto exp(DE_e^{1/4}), \tag{11.9}$$

where $D = 2B(2|\alpha|)^{1/4}$. The threshold behavior of the 5 ^{2}G state is well reproduced by Eq. 11.9 (Fig. 11.14). Eq. 11.9 describes photodetachment cross sections to states having large negative polarizability. The fit of the equation to the data set in Fig. 11.14 can be used to extract the polarizability of the state investigated. Our experiment suggests a polarizability, α, two orders of magnitude smaller than the polarizability calculated in [135]. Since the model described contains several simplifications it can not reproduce the absolute value of the polarizability, but still it provides a good understanding of the process of photodetachment to states where the negative polarizability is the dominating term of the potential in Eq. 2.1.

11.4.2 Cesium

In chapter 10 we have investigated photodetachment of Cs^- in to the Cs(10 ^{2}S), Cs(6 ^{2}F), Cs(6 ^{2}G) and Cs(6 ^{2}H) states. The partial cross sec-

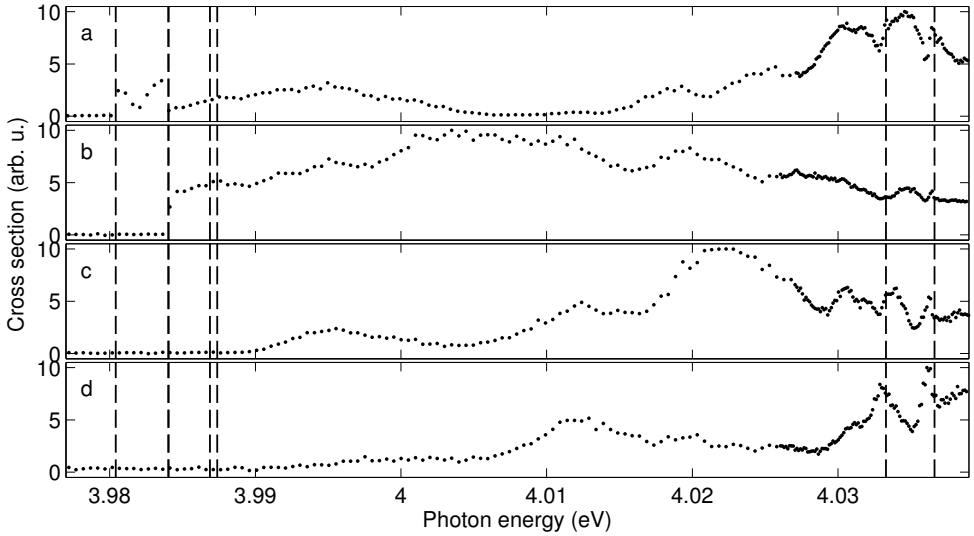

Figure 11.16: *Partial photodetachment cross section in Cs^-. Channels listed from the top: Cs(10 ^{2}S), Cs(6 ^{2}F), Cs(6 ^{2}G) and Cs(6 ^{2}H). Multiple overlapping resonances prevent us from fitting our threshold law to the Cs(6 ^{2}G) and Cs(6 ^{2}H) thresholds. Vertical dashed lines indicates channel openings. Note that this figure contains one additional channel compared to the corresponding figure in chapter 10.*

tions are presented in Fig. 11.16. The experiment covers the energy range from each channel opening up to and above the Cs(10 $^2P_{3/2}$) threshold. The polarizability of the Cs(6 ^{2}F) states is calculated to be large and positive, 7.7×10^6 a.u. [161]. In accordance to theory the threshold behavior is a sharp step function see Fig. 11.16(b). There are no theoretical predictions for the polarizability of the Cs(6 ^{2}G) and Cs(6 ^{2}H) states. Both channel openings exhibit a suppressed character, see Fig. 11.16(c) and (d). The Cs(6 ^{2}H) state seems to have a large negative polarizability. The presence of multiple resonances in the spectra is hindering us from fitting our newly developed threshold law to the data set in a satisfactory way. The resonances also make it impossible to determine wether the suppressed channel opening of the Cs(6 ^{2}G) state is due to a large negative polarizability, yielding an energy dependency according to our threshold law or a low polarizability yielding a Wigner law dependency with a large ℓ. The outgoing electron can, after absorbing a photon, leave the system as a d-wave (ℓ=3) or as a h-wave (ℓ=5). According to the Wigner law, the shape of the threshold is given by $\sigma_{th} = a \times E^{3+1/2} + b \times E^{5+1/2}$. Where a and b are parameters determined by the probability for d-wave and h-wave detachment, respectively.

CHAPTER 12

Conclusion and Outlook

"If we knew what it was we were doing, it would not be called research, would it?"

– Albert Einstein

In my thesis I have studied the dynamics and structure of negative ions, atoms and molecules. The experiments on time dynamics has been conducted in the ultra short laser pulse lab at Albert Ludwig's University in Freiburg, Germany. The structure of negative ions and electron-electron correlations have been investigated at the Göteborg University Negative Ion Laser LAboratory (GUNILLA) in Gothenburg, Sweden.

The most important scientific outcome of my research is the very first direct observations of an spatially moving electronic wave packet in the ground state of an atom. In chapter 6 and 7 we report on how we create such a wave packet in carbon as well as in silicon atoms, and probe their time evolution over a long time interval. The method I have developed can project the electronic wave function directly onto a detector and we achieve a direct visualization of the dynamics without the use of extensive offline data analysis. Future experiments will focus on creating and detecting electronic wave packets in diatomic molecules, such as C_2 and Ag_2. In chapter 4 we report on the first observations on the rescattering effect in strong field detachment of negative ions. The rescattering phenomena occur when the detached electron travels back to, and rescatters on the parent core in the oscillating laser field. The electron picks up substantially more energy, from the laser field, than needed to be detached. These high energy electrons are detected in the experiments in chapter 4. We also present a modified Strong Field Approximation (SFA) theory, including the

rescattering effect providing a very good agreement with experiments. In chapter 5 we investigate the difference between strong field detachment of atomic negative ions (F^-) and molecular negative ions (F_2^-). We observe a broader energy distribution, extending up to higher energies, when detaching molecular ions. The observed effect can be understood by considering photodissociation followed by photodetachment. The dissociation time of a diatomic molecule is shorter than the used laser pulse. Hence, molecules can dissociate at the leading edge of the pulse and the created negative ion will have survived longer in the laser pulse and is thus exposed to a higher laser intensity when detached.

In chapter 8, 9 and 10 we investigate doubly excited states in negative ions. In the same sense as an atom can bind an extra electron and form a negative ion, an excited atom can also bind an extra electron. In these ions, two electrons are in an excited state comparably far from the parent core and therefore electron-electron correlation become pronounced. The shape of the threshold for single photon detachment is dependent on the sign and magnitude of the atom's polarizability. We present the first observations of the threshold behavior in photodetachment to final states having large negative polarizability. The cross section has a slow onset and is not fully developed until the photon energy is far above the threshold. The shape of the threshold is fundamentally different from the step like threshold for previously observed states having large positive polarizability. To explain the observed spectra we have developed a new threshold law able to describe the slow onset and it provides a good fit to experimental spectra. The experiments in chapter 8, 9 and 10 are performed on K^- and Cs^- where resonances from doubly excited states obscures the threshold. We plan to investigate Li^- where the density of doubly excited states is expected to be lower allowing us to observe a threshold where we hope no resonances are interfering.

Acknowledgements

Ever since my school years I have had a fairly clear picture of myself becoming a scientist, I never really considered any other profession. How I ended up in physics is not at all that clear to me though. But what I do know is that science is teamwork. This thesis marks the culmination of my work so far as a researcher and I have a lot of people to thank for getting to this point.

First of all I thank my supervisor in Freiburg, Prof. Hanspeter Helm for letting me into his research group and for hiring me as a PhD student in the beautiful city of Freiburg. Our discussions on the group meetings have been very enlightening. I thank Prof. Dag Hanstorp, my supervisor at the University of Gothenburg. When I first met him and told him that I wanted to go abroad to do a PhD, he was full of enthusiasm and he is the one who really made all this possible in the first place. I truly appreciate his will to teach me physics and for always having time for discussions and to give encouragement. I thank Igor Kiyan, the principal investigator, with whom I have done most of the work in the lab. He has taught me so much on how to conduct a scientific experiment. It is because of him the quality of the data is so good.

I would like to thank Marion for always helping me out. I am very grateful to Fränk at the mechanical workshop in Freiburg. Thank you for your patience all those times when I realized that I needed something done *"already yesterday"*. Timo, Isabella, Uwe and Jan-Åke, Mats, thank you for all the help! I thank Anton for teaching me all that is known on doubly excited states and on the GUNILLA setup that he has built in Gothenburg. I have really enjoyed taking part in the experiments in your project. I am grateful to Sten Salomonson for helping me out when I got into trouble describing our findings theoretically.

A special thank you to Mikael, who is not only the best friend but also the best colleague anyone could have. Lots of thanks to all my friends from the undergraduate studies, I had a great time with you! To all my new friends in Freiburg, from all over the world, thanks a lot! I love Freiburg because of you.

I have the best brothers, Simon and Jakob. We are a team, and that means so much to me. I am happy and grateful to have parents who always support and encourage me. You have raised me in such a way that I believe I can achieve whatever I want.

To Malvika, the most amazing person I have ever met, I love you! Without your love and encouragement I would never have managed to finish this thesis. Thank You.

BIBLIOGRAPHY

[1] M. Planck, First presented at Deutsche Physikalische Gesellschaft e.V in 1900. Published in *Annalen der Physik* **4** 553 (1901).

[2] A. Einstein, *Annalen der Physik*. **322**, 132 (1905).

[3] J. C. Maxwell, *Philosophical Magazine*, **21** & **23** Series 4 (1861).

[4] R. P. Feynman, *The Feynman Lectures on Physics* **2** chap. 18. Addison - Wesley, the definitive edition (2006).

[5] L. de Broglie, Recherches sür la théorie des quanta, Thesis, (1924); L. de Broglie, *Annalen der Phsyik* **3**, 22 (1925).

[6] G. P. Thomson and A. Reid, *Nature* **119** 890 (1927).

[7] C. J. Davisson and L. H. Germer, *Nature* **119** 558 (1927).

[8] C. J. Davisson and L. H. Germer, *Phys. Rev.* **30** 705 (1927).

[9] E. O. Wollan, C. G. Shull and M. C. Marney *Phys. Rev.* **73** 527-528 (1948).

[10] E. Schrödinger, Quantisierung als Eigenwertproblem. *Annalen der Physik*, (4) **79**, 361-376 (1926).

[11] W. Heisenberg, *Zeitschrift für Physik A*, **43**, 3-4, 172-198 (1927).

[12] A. L. Schawlow and C. H. Townes, *Phys. Rev.* **112**, 1940-1949 (1958).

[13] T. H. Maiman, *Nature* **187** 493 (1960).

[14] P. P. Sorokin et al. *IBM Journal of Research and Development* **11** 2, 130 (1967).

[15] F. P. Schäffer et al. *Applied Physics Letters* **9** 8, 306 (1966).

[16] W. E. Lamb Jr., *Phys. Rev.* **134** (6A), A1429 (1964).

[17] E. P. Ippen, C. V. Shank, and A. Dienes, *Appl. Phys. Lett.* **21**, 348 (1972).

[18] J. G. Fujimoto, A. M. Weiner, and E. P. Ippen, *Appl. Phys. Lett.* **44**, 832 (1984).

[19] R. L. Fork et al., *Opt. Lett.* **12** (7), 483 (1987).

[20] M. Drescher et al. *Science* **291**, 1923 (2001).

[21] M. Hentschel et al. *Nature* **414**, 509 (2001).

[22] T. W. Körner. Fourier Analysis, Cambridge University Press (1989).

[23] E. P. Wigner. Phys. Rev. **73**, 1002 (1948).

[24] L. M. Branscomb and W. L. Fite, Phys. Rev. **93**, 651-651 (1954).

[25] L. M. Branscomb and S. J. Smith, Phys. Rev. **98**, 1028-1034 (1955).

[26] L. M. Branscomb and S. J. Smith, Phys. Rev. **98**(4), 1127-1128 (1955).

[27] W. C. Lineberger and B. W. Woodward, Phys. Rev. Lett. **25** (7), 424-427 (1970).

[28] H. Hotop, T. A. Patterson, and W. C. Lineberger, *Bulletin of The American Physical Society* **17**(1), 150 (1972).

[29] T. A. Patterson, H. Hotop, and W. C. Lineberger, *Bulletin of The American Physical Society* **17**(11), 1128 (1972).

[30] H. Hotop, R. A. Bennet and W. C. Lineberger, *Journal Of Chemical Physics* **58**(6), 2373-2378 (1973).

[31] H. Hotop and W. C. Lineberger, *Journal Of Physical and Chemical Reference Data* **4**(3), 539-576 (1975).

[32] M. K. Raarup et al. *Phys. Rev. Lett.* **85** 4028 (2000).

[33] S. J. Buckman and C. W. Clarck, *Rev. o. Mod. Phys.* **66**, 535-655 (1994).

[34] M. Allan, O. Zatsarinny, and K. Bartschat, *J. Phys. B: At. Mol. Opt. Phys.* **44** 065201 (2011).

[35] L. Vejby-Christensen, D. Kella, D. Mathur, H. B. Pedersen, H. T. Schmidt, and L. H. Andersen *Phys. Rev. A* **53** 2371 (1996).

[36] K. Fritioff, J. Sandström, P. Andersson, D. Hanstorp, F. Hellberg et al. *Phys. Rev. A* **69** 042707 (2004).

[37] K. Fritioff, J. Sandström, P. Andersson, D. Hanstorp, F. Hellberg et al. *J. Phys. B: At. Mol. Opt. Phys.* **37** 2241 (2004).

[38] H. B. Pedersen, N. Djurić, M. J. Jensen, D. Kella, C. P. Safvan et al. *Phys. Rev. A* **60** 2882 (1999).

[39] M. C. McCarthy, C. A. Gottlieb, H. Gupta and P. Thaddeus *Asrophys. J. Lett.* **652** L141 (2006).

[40] E. Roueff and E. Herbst, *J. Phys. Conf. Ser.* **192** 012008 (2009).

[41] T. Best, *Astrophysical Journal* **742** 2:63 (2011).

[42] J. Deiglmayr, *European Physical Journal D* **65** 1-2, 99-104 (2011).

[43] S. Trippel, *Journal of Chemical Physics* **134** 10 (2011).

[44] M. Goeppert-Mayer, *Ann. Phys.* **9**, 273-94 (1931).

[45] V. Hughes and L. Grabner, *Phys. Rev.* **79**, 314-22 (1950).

[46] J. Brosel, B. Cagnac and A. Kastler, *C. R. Acad. Sci. Paris.***237**, 984-6 (1953).

[47] J. Winter, *Ann. Phys.* **4**, 745-811 (1959).

[48] P. Kusch, *Phys. Rev.* **93**, 1022-5 (1954).

[49] W. Kaiser and C. Garret, *Phys. Rev. Lett.* **7**, 229-31 (1961).

[50] I. Abella *Phys. Rev. Lett.* **9**, 453-5 (1962).

[51] J. Hall, E. Robinson and L. Branscomb, *Phys. Rev. Lett.* **14**, 1013-6 (1965).

[52] G. Voronov and N. Delone, *JETP Lett.* **1** 66-8 (1965).

[53] P. Agostini, G. Barjot, J. F. Bonnal, G. Mainfray, and C. Manus, *IEEE J. Quantum. Electron.* **QE-4** 667-9 (1968).

[54] P. Agostini et al. *Phys. Rev. Lett.* **42**, 1127 (1979).

[55] E. Jr. Martin and L. Mandel *Appl. Opt.* **15** 2378-80 (1976).

[56] Y. Gontier and M. Trahin *J. Phys. B: At. Mol. Opt. Phys.* **13**, 259-72 (1980).

[57] C. Blondel et al. *J. Phys. B: At. Mol. Opt. Phys.* **24** 3575 (1991).

[58] H. Stapelfeldt, P. Balling, C. Brink, H. K. Haugen *Phys. Rev. Lett.* **67** 13, 1731-1734 (1991).

[59] MD. Davidson et al. *Phys. Rev. Lett.* **67** 13, 1712-1715 (1991).

[60] A. McPherson, G. Gibson, H. Jarah, U. Johann, T. S. Luk, I. McIntyre, K. Boyer, and C. Rhodes *J. Opt. Soc. Am. B* **4** 595-601 (1987).

[61] M. Ferray, A L' Huillier, X. F. Li, L. A. Lompré, G. Mainfray and C. Manus *J. Phys. B: At. Mol. Opt. Phys.* **21** L31-5 (1988).

[62] X. F. Li, A. L' Huillier, M. Ferray, L. A. Lompré and G. Mainfray, *Phys. Rev. A* **39** 5751-61 (1989).

[63] A. Lompré, M. Ferray and G. Mainfray *AIP Conf. Proc. No. 205* New York: AIP, pp 505-12 (1989).

[64] I. Yu. Kiyan and H. Helm, *Phys. Rev. Lett.* **90**, 183001 (2003).

[65] L. V. Keldysh, *Sov. Phys. JETP* **20**, 1307 (1964).

[66] D. M. Volkov, *Z. Phys.* **94**, 250 (1935).

[67] F. H. M. Faisal, *J. Phys. B.* **6** L89 (1973).

[68] H. R. Reiss, *Phys. Rev. A* **22**, 1786 (1980).

[69] G. F. Gribakin and M. Yu. Kuchiev, *Phys. Rev. A* **55**, 3760-3771 (1997).

[70] R. Kopold, W. Becker and M. Kleber, *Opt. Commun.* **179**, 39 (2000).

[71] B. Bergues, Z. Ansari, D. Hanstorp and I. Yu. Kiyan, *Phys. Rev. A* **75**, 063415 (2007).

[72] B. Bergues and I. Yu. Kiyan. *Phys. Rev. Lett.* **100**, 143004 (2008).

[73] A. E. S. Green, D. E. Rio, and T. Ueda, *Phys. Rev. A* **24**, 3010 (1981).

[74] M. V. Ammosov, N. B. Delone, and V. P. Krainov, *Sov. Phys. JETP* **64**, 1191 (1986).

[75] R. Reichle, H. Helm, and I. Yu. Kiyan, *Phys. Rev. Lett.* **87**, 243001 (2001);

[76] R. Reichle, H. Helm and I. Yu. Kiyan, *Phys. Rev. A* **68**, 063404 (2003).

[77] R. Reichle, *Exotic Species of Hydrogen.* Ph.D. Thesis. Department of Physics, Albert Ludwig's University (2001).

[78] Model PS-120 from Peabody Scientific. Massachusetts, USA.

[79] A.T.J.B. Eppink and D.H. Parker, *Rev. Sci. Instrum.* **68**, 3477 (1997).

[80] Photon Engineering, LLC 440 S Williams Blvd. #106, Tucson, AZ 85711. www.photonengr.com

[81] C. Bordas, F. Pauling, H. Helm and D. L. Huestis, *Rev. Sci. Instrum.* **67**, 2257 (1996).

[82] Halliday, Resnick and Walker *Fundamentals of Physics* 6th edition, Chapter 35-7, Eq. 37-14. Wiley & sons, Inc (2001).

[83] B. Bergues, *On the Photodetachment Dynamics of Negative Ions in Strong Laser Fields.* Ph.D. Thesis. Department of Physics, Albert Ludwig's University (2008).

[84] T. Wilbois, *Single Ionization of Molecular Hydrogen in Strong Laser Fields.* Ph.D. Thesis. Department of Physics, Albert Ludwig's University (2011).

[85] C. E. Moore, Tables of Spectra of Hydrogen, Carbon, Nitrogen, and Oxygen Atoms and Ions, in CRC Series in Evaluated Data in Atomic Physics, 339 pp. (Edited by J. W. Gallagher, CRC Press, Boca Raton, FL, 1993).

[86] A. O. Lindahl, *Two-Electron Excitations in Negative Ions.* Ph. D. thesis. University of Gothenburg, Sweden (2011).

[87] 3D-viz by Arvid Forsberg, Intelligent Light Studios. www.intelligent-light.com

[88] S.E. Sobottka and M.B. Williams, *IEEE Trans. Nucl. Sci.* **35**, 348 (1988).

[89] O. Jagutzki et al., *Proc. SPIE* **3438**, 322 (1998).

[90] D. B. Milošević, A. Gazibegović-Busuladžić, and W. Becker, *Phys. Rev. A* **68**, 050702(R) (2003)

[91] A. Gazibegović-Busuladžić, D. B. Milošević, and W. Becker, *ibid.* **70**, 053403 (2004).

[92] L. F. DiMauro and P. Agostini, Adv. At., Mol., Opt. Phys. **35**, 79 (1995).

[93] W. Becker, F. Grasbon, R. Kopold, D. B. Milošević, G. G. Paulus, and H. Walther, Adv. At., Mol., Opt. Phys. **48**, 35 (2002).

[94] G. G. Paulus, W. Becker, W. Nicklich, and H. Walther, J. Phys. B **27**, L703 (1994).

[95] D. B. Milošević, G. G. Paulus, D. Bauer, and W. Becker, J. Phys. B **39**, R203 (2006); F. Krausz and M. Ivanov, Rev. Mod. Phys. **81**, 163 (2009).

[96] G. G. Paulus *et al.*, Phys. Rev. Lett. **91**, 253004 (2003); T. Wittmann *et al.*, Nature Phys. **5**, 357 (2009).

[97] M. Okunishi *et al.*, Phys. Rev. Lett. **100**, 143001 (2008); D. Ray *et al.*, Phys. Rev. Lett. **100**, 143002 (2008).

[98] To our knowledge, only J. Pedregosa-Gutierrez *et al.*, Phys. Rev. Lett. **93**, 223001 (2004), consider rescattering to explain a "knee" structure in the yield curve of positively charged fluorine ions produced by double detachment of F^-.

[99] V. R. Bhardwaj *et al.*, Phys. Rev. Lett. **86**, 3522 (2001).

[100] B. Borca, M. V. Frolov, N. L. Manakov, and A. F. Starace, Phys. Rev. Lett. **87**, 133001 (2001).

[101] M. V. Frolov, N. L. Manakov, E. A. Pronin, and A. F. Starace, J. Phys. B **36**, L419 (2003).

[102] A. E. S. Green, D. L. Sellin, and A. S. Zachor, Phys. Rev. **184**, 1 (1969).

[103] R. Kopold, W. Becker, and M. Kleber, Phys. Rev. A **58**, (1998).

[104] K. A. Hanold *et al.*, Rev. Sci. Instrum. **70**, 2268 (1999)

[105] E. Goulielmakis, et al., Nature **466**, 739 (2010).

[106] J. A. Yeazell et al., Phys. Rev. Lett. **60**, 1494 (1988).

[107] S. Zamith, et al., Eur. Phys. J. D **12**, 255 (2000).

[108] Q. Zhang et al., Optics Letters **33**, 1893 (2008).

[109] A. ten Wolde, et al., Phys. Rev. Lett. **61**, 2099 (1988).

[110] S. Gilb, et al., Journal of Physics B: Atomic, Molecular and Optical Physics **39**, 4231 (2006).

[111] A. Fleischer, et al., Phys. Rev. Lett. **107**, 113003 (2011).

[112] M. V. Frolov, et al., Phys. Rev. Lett. **91**, 053003 (2003).

[113] L. Young, et al., Phys. Rev. Lett. **97**, 083601 (2006).

[114] R. Santra, et al., Phys. Rev. A **74**, 043403 (2006).

[115] C. Höhr, et al., Phys. Rev. A **75**, 011403 (2007).

[116] Z.-H. Loh, et al., Phys. Rev. Lett. **98**, 143601 (2007).

[117] P. Andersson et al. NIMB **266**, 3667-3673 (2008).

[118] N. Rohringer and R. Santra. *Phys. Rev. A.* **79**, 053402 (2009).

[119] Camera model "Imager" form LaVision GmbH, Anna-Vandenhoeck-Ring 19, D-37081 Göttingen

[120] TOPAS model 8041, Light Conversion Ltd. Vilnius, LT-10223, Lithuania.

[121] J. Sugar and A. Musgrove, *J. Phys. Chem. Ref. Data* **22**, 1213Ð1278 (1993).

[122] H. R. Sadeghpour, J. L. Bohn, M. J. Cavagnero, B. D. Esry, I. I. Fabrikant, J. H. Macek, and A. R. P. Rau, J. Phys. B: At. Mol. Opt. Phys. 33, R93 (2000).

[123] B. Jonson, Phys. Rep. 389, 1 (2004).

[124] B. DeMarco, J. L. Bohn, J. P. Burke, M. Holland, and D. S. Jin, Phys. Rev. Lett. 82, 4208 (1999).

[125] Y. P. Zhang, C. H. Cheng, J. T. Kim, J. Stanojevic, and E. E. Eyler, Phys. Rev. Lett. 92, 203003 (2004).

[126] G. Rupak and R. Higa, Phys. Rev. Lett. 106, 222501 (2011).

[127] R. C. Bilodeau, M. Scheer, H. K. Haugen, and R. L. Brooks, Phys. Rev. A 61, 012505 (1999).

[128] H. Hotop, T. A. Patterson, and W. C. Lineberger, Phys. Rev. A 8, 762 (1973).

[129] H. Hotop and W. C. Lineberger, J Chem. Phys. 58, 2379 (1973).

[130] R. C. Bilodeau, J. D. Bozek, N. D. Gibson, C. W. Walter, G. D. Ackerman, I. Dumitriu, and N. Berrah, Phys. Rev. Lett. 95, 083001 (2005).

[131] J. W. Farley, Phys. Rev. A 40, 6286 (1989).

[132] T. F. O'Malley, Phys. Rev. 137, A1668 (1965), Note the error in the sign of the correction factor, see for example ref [128].

[133] S. Watanabe and C. H. Greene, Phys. Rev. A 22, 158 (1980).

[134] J. Sandstroöm, G. Haeffler, I. Kiyan, U. Berzinsh, D. Hanstorp, D. J. Pegg, J. C. Hunnell, and S. J. Ward, Phys. Rev. A 70, 052707 (2004).

[135] C.-N. Liu, Phys. Rev. A 64, 052715 (2001).

[136] J. E. Sansonetti, J. Phys. Chem. Ref. Data 37, 7 (2008).

[137] J. M. Blatt and V. F. Weisskopf, Theoretical Nuclear Physics (Springer-Verlag, New York, 1979).

[138] C. Diehl, K. Wendt, A. O. Lindahl, P. Andersson, and D. Hanstorp, Rev. Sci. Instrum. 82, 053302 (2011).

[139] D. A. Dahl, Int. J. Mass Spectrom. 200, 3 (2000).

[140] T. Andersen, H. K. Haugen, and H. Hotop, J. Phys. Chem. Ref. Data 28, 1511 (1999).

[141] C.-N. Liu and A. F. Starace, Phys. Rev. A 60, 4647 (1999).

[142] W. Klopper, R. A. Bachorz, D. P. Tew, and C. Hättig, Phys. Rev. A 81, 022503 (2010).

[143] K. R. Lykke, K. K. Murray, and W. C. Lineberger, Phys. Rev. A 43, 6104 (1991).

[144] S. I. Themelis, J. Chem. Phys. 132, 154111 (2010).

[145] E. Lindroth and J. L. Sanz-Vicario, Radiat. Phys. Chem. 70, 387 (2004).

[146] P. Balling, H. H. Andersen, C. A. Brodie, U. V. Pedersen, V. V. Petrunin, M. K. Raarup, P. Steiner, and T. Andersen, Phys. Rev. A 61, 022702 (2000).

[147] H. R. Sadeghpour and C. H. Greene, Phys. Rev. Lett. 65, 313 (1990).

[148] P. G. Harris, H. C. Bryant, A. H. Mohagheghi, R. A. Reeder, H. Sharifian, C. Y. Tang, H. Tootoonchi, J. B. Donahue, C. R. Quick, D. C. Rislove, W. W. Smith, and J. E. Stewart, Phys. Rev. Lett. 65, 309 (1990).

[149] U. Ljungblad, D. Hanstorp, U. Berzinsh, and D. J. Pegg, Phys. Rev. Lett. 77, 3751 (1996).

[150] G. Haeffler, I. Yu. Kiyan, U. Berzinsh, D. Hanstorp, N. Brandefelt, E. Lindroth, and D. J. Pegg, Phys. Rev. A 63, 053409 (2001).

[151] G. Haeffler, I. Yu. Kiyan, D. Hanstorp, B. J. Davies, and D. J. Pegg, Phys. Rev. A 59, 3655 (1999).

[152] I.Yu.Kiyan,U.Berzinsh,J.Sandström,D.Hanstorp, and D. J. Pegg, Phys. Rev. Lett. 84, 5979 (2000).

[153] A.O.Lindahl, J.Rohlén, H.Hultgren, I.Yu..Kiyan, D. J. Pegg, C. W. Walter and D. Hanstorp, Phys. Rev. Lett. 108, 033004 (2012).

[154] K. T. Andersson, J. Sandström, I. Yu. Kiyan, D. Hanstorp, and D. J. Pegg, Phys. Rev. A 62, 022503 (2000).

[155] S. Kaufman, Opt. Commun. 17, 309 (1976).

[156] P. Andersson, A. O. Lindahl, C. Alfredsson, L. Rogström, C. Diehl, D. J. Pegg, and D. Hanstorp, J. Phys. B: At. Mol. Opt. Phys. 40, 4097 (2007).

[157] U. Fano, Phys. Rev. 124, 1866 (1961).

[158] B. W. Shore, Phys. Rev. 171, 43 (1968).

[159] D. G. McDonald and A. Crowe, J. Phys. B: At. Mol. Opt. Phys. 26, 2887 (1993).

[160] D. Antypas and D. S. Elliott, Phys. Rev. A 83, 062511 (2011).

[161] W. van Wijngaarden and J. Li, J. Quant. Spectrosc. Ra. 52, 555 (1994).

[162] M. Scheer, J. Th¿gersen, R. C. Bilodeau, C. A. Brodie, H. K. Haugen, H. H. Andersen, P. Kristensen, and T. Andersen, Phys. Rev. Lett. 80, 684 (1998).

[163] C. Fischer and D. Chen, J. Mol. Struct.: THEOCHEM 199, 61 (1989).

[164] C. H. Greene, Phys. Rev. A 42, 1405 (1990).

[165] J. Slater, F. H. Read, S. E. Novick, and W. C. Lineberger, Phys. Rev. A 17, 201 (1978).

[166] H. Stapelfeldt and H. K. Haugen, Phys. Rev. Lett. 69, 2638 (1992).

[167] A. O. Lindahl et al. Phys. Rev. A **85**, 033415 (2012).

[168] J. E. Sansonetti, J. Phys. Chem. Ref. Data 38, 761 (2009).

[169] H. Friedrich, Theoretical atomic physics (Springer, Berlin, 1991).

[170] B. Yang et al. *Phys. Rev. Lett.* **71**, 3770Ð3773 (1993).

[171] T. K. Kjeldsen and L.B. Madsen, *J. Phys. B* **37**, 2033 (2004).

[172] A. Jarón-Becker, A. Becker, and F. H. M. Faisal, *Phys. Rev. A* **69**, 023410 (2004).

[173] D. B. Milošević, *Phys. Rev. A* **74**, 063404 (2006).

[174] J. G. Dojahn, E. C. M. Chen, and W. E. Wentworth, *J. Phys. Chem.* **100**, 9649 (1996).

[175] L. D. Landau and E. M. Lifshitz, *Quantum Mechanics. Non-relativistic Theory* 3rd edition. Pergamon, Oxford (1977).